Faculty of Engineering

**Confocal Surface Plasmon Microscopic Sensing**

By

Bei Zhang，Msc

Thesis submitted to

The University of Nottingham for the degree of

Doctor of Philosophy

June 2013

# Abstract

Surface Plasmons provide a relatively high axial sensitivity and thus are generally used in a thin surface film sensing and imaging. Objective lens based surface plasmon microscopy enables measurement of local refractive index on a far finer scale than the conventional prism based systems. However, researchers find that a trade-off between the lateral resolution and the axial sensitivity exists in the conventional intensity based surface plasmon microscopy. In order to optimize the trade-off, interferometric surface plasmon microscopy was exploited. An interferometric or confocal system gives the so-called *V(z)* curve, the output response as a function of defocus, when the sample is scanned axially, which gives a measure of the surface plasmon propagation velocity. Considering the complexity of the two arm interferometric system, in this thesis, I show how a confocal system provides a more flexible and more stable alternative.

This confocal system, however, places greater demands on the dynamic range of the system. Firstly, the sharp edge of the pupil on the back focal plane of the objective can generate similar effect with the surface plasmon (SPs) ripples; Secondly, the SPs ripples that convey much of the information are much smaller compared to the in focus response which means the confocal system suffers from low signal to noise ratio (SNR). In order to overcome the limitations, I proposed pupil function engineering which was to use a spatial light modulator to modulate the illumination beam profile by using the designed pupil functions with smooth edges. The results show that the sharp edge effect of confocal setup can be greatly reduced and the SNR is improved. Based on this system, I demonstrated that images obtained from the setup are comparable with the two arm interferometric SPR microscope and other wide-

field non-SPR microscope.

Secondly, I demonstrate the technique of $V(\alpha)$. A phase Spatial Light Modulator (SLM) was applied to replace the previous amplitude SLM. I show how a phase spatial light modulator (i) performs the necessary pupil function apodization (ii) imposes an angular varying phase shift that effectively changes sample defocus without any mechanical movement and (iii) changes the relative phase of the surface plasmons and reference beam to provide signal enhancement not possible with previous configurations using ASLM.

Later, I extend the interferometer concept in the confocal system to produce an 'embedded' phase shifting interferometer in chapter 6, where I can control the phase between the reference and surface plasmon beams with a spatial light modulator. I demonstrate that this approach facilitates extraction of the amplitude and phase of the surface plasmons to measure of the phase velocity and the attenuation of the surface plasmons with greatly improved signal to noise compared to previous measurement approaches[1]. I also show that reliable results are obtained over smaller axial scan ranges giving potentially superior lateral resolution.

In the end of the thesis, future work will be discussed. Firstly, I will propose another technique called 'artificial' plasmon. Secondly, I will recommend constructing another system and develop the ideas discussed so the system can work in aqueous environment.

# Contents

# Acknowledgement

I have been very lucky to be supervised by Prof. Mike Somekh. I would like to express my sincere gratitude to him for his considerable knowledge, stimulating guidance, encouragement and patience in the research. The knowledge and creative ideas will definitely benefit my future. I wish to thank Dr. Chung See for his valuable knowledge in optics and kind help in my research. I also appreciate Dr. Suejit Pechprasarn for his kind support during our co-operation.

I wish to also thank Dr. Mark Pitter for his guidance and training to me during my first two years; thank Dr. Jing Zhang and Maria Bivolarska for teaching me the ways of optical system alignment and sharing valuable experiences; thank Dr. Kevin Webb for his kind help in teaching me experimental techniques; thank Kelly Vere for her kind support in IBIOS things; thank all the members of the IBIOS for their kind help and support, especially Gilbert, Stephen, Bo, Jing W. and Feng. I am really happy to say I am so happy and I do enjoy my PhD in the UK, including the research, study and living. I would like to give my appreciation to the China Scholarship Council, University of Nottingham, and Embassy of the People's Republic of China in the UK for the secured funding.

Finally, I would like to thank my parents, my elder sister, my brother-in-law, my younger brother and my lovely niece for their love, care and support.

# Declaration

No portion of the work referred to in this thesis has been submitted in support of an application for another degree or qualification of this or any other university or other institute of learning.

# Publications

*Journals*

1. B. Zhang, S. Pechprasarn, M. Somekh (2012). "Confocal surface plasmon microscopy with pupil function engineering." **Optics Express** **20**(7): 7388-7397. **(SCI/IF : 3.587)** *[Selected topic in the Virtual Journal for Biomedical Optics, 2012, Vol. 7, Iss. 5.]*

2. B. Zhang, S. Pechprasarn, M. Somekh (2012). "Surface plasmon microscopic sensing with beam profile modulation." **Optics Express** **20**(27): 28039-28048. **(SCI/IF : 3.587)** *[Selected topic in the Virtual Journal for Biomedical Optics, 2013, Vol. 8, Iss. 1.]*

3. B. Zhang, S. Pechprasarn, M. Somekh (2013) "Quantitative plasmonic measurements using embedded phase stepping confocal interferometry" **Optics Express** **21**(9): 11523–11535. **(SCI/IF : 3.587)** *[Selected topic in the Virtual Journal for Biomedical Optics, 2013, Vol. 8, Iss. 6.]*

4. S. Pechprasarn, B. Zhang, D. Albutt, J. Zhang, M.Somekh(2013).'Ultrastable embedded surface plasmon confocal interferometry' **Light: Science & Applications** (To be submitted)

*Conference*

1. B. Zhang, S. Pechprasarn, M. Somekh (2011). "Confocal surface plasmon resonance microscopy with pupil function engineering". **Functional Optical Imaging**, IEEE, Ningbo, China.

# 1    Introduction

This chapter is a basic introduction to the whole thesis and includes three sections. They are background to the project, general introduction, and the thesis layout.

## 1.1 Background issues of the project

Sensing and imaging thin transparent films quantitatively with high sensitivity and good lateral resolution has always been a challenge in biological optics. Many interference-related techniques which transform the phase information into intensity can be applied, like the Nobel Prize winning phase contrast technique developed by Zernike[2]. Other methods such as differential interference contrast (DIC) perform similar roles. These techniques have made great contributions in this field. Compared to these techniques, surface plasmon resonance (SPR) technique can provide higher sensitivity for layer thickness in the sub-nanometre range which makes the SPR technique an outstanding and relatively powerful tool in biological or chemical fields. Perhaps even more significant, from the point view of direction of observation, the SPR technique is much more convenient as the sample is located on the other side of the coverglass, as shown in Fig. 1-1(a) compared to conventional microscopic techniques shown in Fig. 1-1(b), especially when using a high NA objective lens whose working distance is usually around 0.1mm. However, just as one proverb says, "one can't have one's cake and eat it too". For cell-level samples, SPR is limited by its poor lateral resolution of around tens of microns. Furthermore, much literature has shown there is a conflict between the sensitivity and lateral resolution for SP imaging. Thus, to overcome or at least optimize the conflict has been a challenge in the SPR field. Some efforts have been tried, like using high NA oil-immersion objectives, or even solid-immersion objectives; other approaches use other metals such as aluminium which has a short propagation length. All of

them have optimized the lateral resolution to some extent. Our group has developed a method that overcomes some of these problems. A heterodyne interferometric surface plasmon microscopy (SPRM) was developed by introducing the method of *V(z)*, which has obtained lateral resolution(10%-90% edge response[3]) of submicron region comparable to other good quality optical microscopy, but without significant reduction in sensitivity. This interferometric SPRM combines the technique of SPR and a two arm interferometer. It is well known that a two arm interferometer suffers from some experimental limitations, like complexity of optical system, high sensitivity to the environmental vibration, etc. Then I ask if there is any other kind of setup to help us to overcome the drawbacks of the two arm configuration, while obtaining comparable results. I present the idea of replacing the heterodyne interferometer with a single arm common path confocal surface plasmon resonance microscopy. The problem with the new confocal arrangement is that i) the sharp edge effect of the system can generate some ripples, which does not contribute to the SP signal ii)the SP ripples that convey much of the information are relatively smaller compared to the in focus response. That means that the system places greater demands on the dynamic range of the system. In order to optimize the two problems, I proposed pupil function engineering which was to use a spatial light modulator to modulate the illumination beam profile by using the designed pupil functions with smooth edges. More details on how to develop the experimental system will be disclosed in chapter 3, and details in the confocal SPRM with pupil function engineering will be in chapter 4.
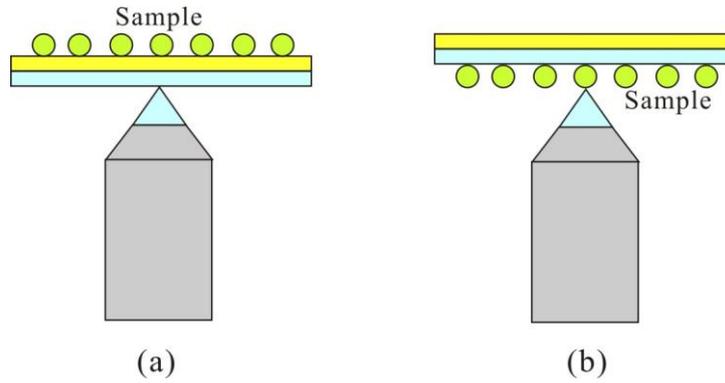
Fig. 1-1 Comparison of sample location from the point view of direction of observation. (a) shows the SPR technique; (b) shows the other techniques.

Secondly, in the confocal surface plasmon resonance microscopy, I use a piezoelectric stage to scan over the z direction and generate the output response as a function of defocus, $V(z)$ effect. During the experiment, I found that there are some improvements which can be made. Firstly, in the mechanical scanning: 1) sample relocation is a big challenge for us; 2) microphonics is another problem. Can I avoid mechanical scanning? By analyzing the phase term variations when moving the defocus distance mechanically, I propose the technique of $V(\alpha)$. 'α' here refers to the phase we impose on the back focal plane (BFP). I show how a phase spatial light modulator (1) performs the necessary pupil function apodization (2) imposes an angular varying phase shift that effectively changes sample defocus without any mechanical movement and (3) changes the relative phase of the surface plasmons and reference beam to provide signal enhancement not possible with previous configurations. More details will be shown in chapter 5.

Thirdly, since the confocal system acts as a two beam interferometer the SLM can be used to introduce a phase shift between reference and plasmon beams, so that phase stepping inteferometry can be applied to extract detailed information on the SP propagation. I show that the interferometer can extract amplitude and phase of surface plasmons directly. This provides the first objective based far field direct measurement of these properties. This

approach produces a far more accurate measurement of the angle at which plasmons are excited, $\theta_p$, which, in turn, gives the plasmon k-vector. The method also gives the attenuation of the surface waves. I demonstrate quantitative measurement of surface wave propagation properties on a range of surfaces.

## 1.2 General introduction

A scanning heterodyne interferometric microscope has been developed and realized by previous researchers in our group in 2000 [4, 5] and then later employed by other researchers [6-8]. More recently this idea has even been extended to a wide-field configuration [9, 10]. The problem associated with the interferometric configuration is that it places severe demands on system stability and in the case of the heterodyne system acousto-optic modulators and associated electronics are required. This thesis concerns the confocal scanning surface plasmon resonance microscope (SPRM). To the author's knowledge, it is the first time the confocal technique is applied to the interferometric SPR microscopy and experimentally realized. The underlying idea is that a confocal system has the same transfer function as the interferometric system, which was discussed by Somekh in 1992[11]. The experimental setup involves a single arm confocal microscope, as shown in Fig. 1-2. It resolves the conflict between high resolution and high sensitivity in non-interferometric SPRM and supplements the limitations of two arm scanning heterodyne interferometric microscope. Basically, the project still utilizes the so-called *V(z)* technique as the scanning heterodyne interferometric microscope. The essential idea is that when the sample moves towards to the objective lens above the focal plane of the objective, there are two major contributions to the output signal, one arising from the SP (P2 in Fig. 1-2 ) and the other from light directly reflected from the sample (P1 in Fig. 1-2). As the sample is defocused the

relative phase between these contributions changes leading to an oscillating signal whose period depends on the angle of incidence at which SPs are excited.
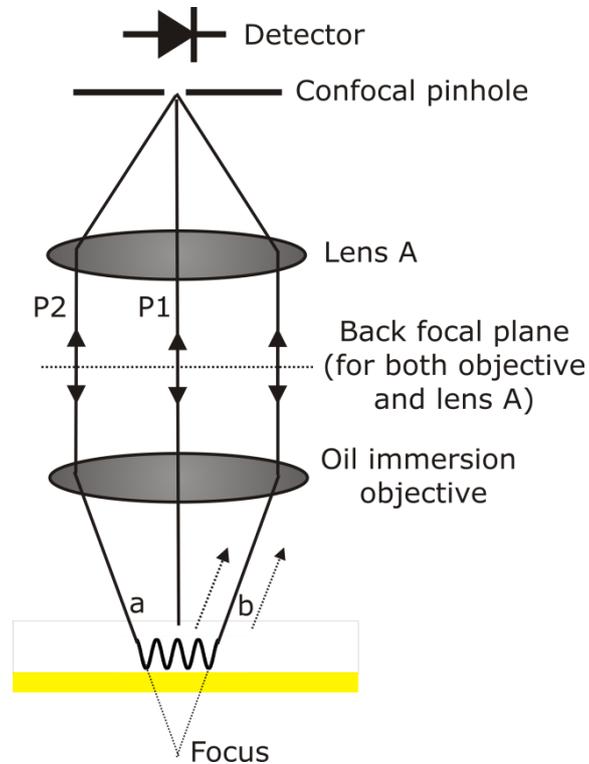


Fig. 1-2 Diagram of the confocal surface plasmon microscopy figure

This project concentrates on the confocal configuration. It does reduce the complexity of former two arm interferometric system and provide a more versatility. Several issues in the realization section need to be considered:

1) Why using surface plasmon resonance microscopy (SPRM)?

2) How to combine the confocal idea to a surface plasmon resonance (SPR) microscope system?

3) How to make the system setup more flexible?

4) How to suppress the sharp edge effect of clear aperture of the objective lens and overcome the low SNR and low dynamic range of the system problems?

5) Is it possible to remove the mechanical scanning?

6) Any more features, such as quantitative measurement?

For 1), SPR is a kind of surface electromagnetic wave and it is fairly sensitive to the variations of thickness or refractive index on the surface. SPRM is a novel kind of microscopy which applies the SPR to the field of microscopy and it can provide considerably high sensitivity on the axial direction [3, 12-17]. The project is based on this.

For consideration 2), many efforts were made and a whole experiment platform on using confocal technique on SPRM was developed and built. Chapter 3 will introduced the whole platform, including the optical system, controlling system, data processing system, etc.

For 3), in order to make the system as flexible as possible, a confocal system is used according to the experiment requirements. A selection of camera pixels is used to replace the pinhole in front of camera in conventional confocal microscope. Removing the interferometer configuration and physical pinholes makes the system more versatile and more flexible.

For 4), the ripples owing to the confocal sharp effect are small compared to in focus response. That means that the system places greater demands on the dynamic range of the system. I therefore use an amplitude sensitive spatial light modulator to engineer the microscope pupil function to suppress the sharp edge effect, which does not contribute to the plasmon signal. Experimental results demonstrate that both the theory and pupil function engineering works. Later in chapter 4, by optimizing the pupil functions used in the system, contrast of the system can be improved. I introduced an amplitude sensitive Spatial Light Modulator (SLM) to the system to modulate the pupils. A corresponding controlling system was developed. This part of information can be found in chapter 4.

Although the amplitude spatial light modulator (ASLM) works quite well in the project, it cannot be used to modulate the phase profile and thus limit the application of the confocal

SPRM. Therefore, after the experiment of chapter 4, another experimental system was built up by using a phase sensitive Spatial light modulator to replace the amplitude sensitive SLM. Related controlling hardware and software are developed. More details will be introduced in chapter 3. Based on this phase SLM based experiment setup, I calculate the phase variations of the mechanical scanning and propose the $V(\alpha)$ technique. The point of '6' above concerns this technique. Details can be found in chapter 5. Furthermore, this new setup makes the quantitative measurements possible. Details are in chapter 6.

## 1.3 Layout of the thesis

The layout of the thesis is as follows.

Chapter 1 presented the background issues, introduction of the project and thesis layout;

Chapter 2 is a review of the SPs, SPR sensing and SPR microscopy.

Chapter 3 introduces the instrumentation development, including the general design, specific optical section design, automation hardware and software development, data processing program, and test results of the setup.

Chapter 4 describes confocal surface plasmon microscopy with pupil function engineering. Preliminary images are presented.

Chapter 5 describes the technique of $V(\alpha)$.

Chapter 6 is about the measurement of SPs properties, like the phase velocity and SPs propagation length. Phase-stepping algorithm was exploited to extract the SPs.

Chapter 7 gives the discussion and suggestions for future work.

# 2  Review

As this project is mainly concerned with confocal microscopy, which combines the confocal technique with the field of surface plasmon microscopy, it is necessary to review the surface plasmon and confocal microscopy as well as surface plasmon resonance microscopy (SPRM). In this chapter, I start the review from the physics of surface plasmons (SPs); then based on the SPs, some properties of surface plasmon resonance (SPR) are introduced and some simulation results on the SPR are provided; furthermore, different kinds of surface plasmon microscopes are described. In the last section, I will review confocal technique and briefly introduce the confocal SPRM in this review.

## 2.1 Physics of SPs

### 2.1.1 What is a plasmon?

In early literature of 1902 and 1912, a physical phenomenon of dark bands or an anomaly was observed in metal gratings [18, 19] which half a century later was found to be SPR. These were reported by R.W. Wood who claimed that this anomaly only exists when the illuminated electric field is parallel to the grating vector. At its first discovery, this kind of anomaly could not be explained by classical theories and Wood did not provide any interpretations for this anomaly. In 1907, Rayleigh provided a theoretical explanation of the anomaly for the first time in history by using the 'dynamical theory of grating', which was based on the scattered electromagnetic field theory [20, 21]. Rayleigh validated his theory by using the characteristics of the grating Wood provided, such as period, profile of material, metal. Rayleigh found that there was a mismatch between the prediction by his theory and Wood's experiment results. The mismatch remained until Fano [22] proposed his theory of 'a forced resonance' by distinguishing the sharp anomaly assumed by Rayleigh and the diffuse

anomaly observed by Wood in 1941. In 1965, Hessel and Oliner [23] provided a new theoretical explanation by using the wave guide theory and drew the same conclusion as Fano. Until then, all the anomalies were observed on gratings. In the 1950s and 1960s, the anomalies were observed on thin films by Ritchie, Powell and Swan [24, 25]. Pines and Bohmic [26-29] suggested some explanation in terms of plasmons and later, many rigorous vector theories were proposed to explain the phenomenon, like the integral theory and differential theory of gratings. Since its discovery, the phenomenon of surface plasmons has been proved of considerable interest to physicists and considerable application to chemists and biologists [30]. In this project, I apply the concept that surface plasmon is an electromagnetic wave and will use some theories based on Maxwell's Electromagnetic equations to analyze its properties.

## 2.1.2 Properties of SPs

Physically, a plasmon refers to the quantum phenomenon of collective oscillations of free electrons by using the electric field or photon coupling. When a periodic external electric field is imposed, such as light, the electron cloud will oscillate and thus a propagating wave of 'plasmon' is generated. Some of the energy of these vibrating electrons is lost as ohmic heating; other losses can include radiative losses in the form of light. If the plasmon is excited and propagates along the interface between two materials, such as a dielectric and metal interface as show in Fig. 2-1, it is called a surface plasmon.
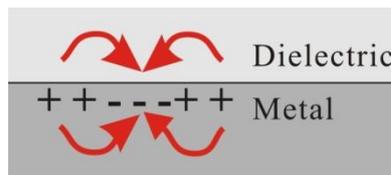


Fig. 2-1 Collective oscillation along a metal - dielectric interface

Here, we look for a surface wave bound to the interface between a semi-infinite dielectric and a semi-infinite metal whose necessary properties will be discussed below. Maxwell's equations are solved with boundary conditions (dielectric 1 and metal 2) as shown in Fig. 2-2 (a). As only p polarized waves can be used to excite surface plasmons, here, the derivations are only correct for the p polarization. $\epsilon_1$ and $\epsilon_2$ are the electric permittivity of dielectric and metal and $k_{z1}$ and $k_{z2}$ are the normal components of the k-vectors in the dielectric and metal. The corresponding coordinate system definition is shown in Fig. 2-2 (b). In this part, references [31-34] are referenced.



(a) k vector decomposition          (b) Definition of coordinate system
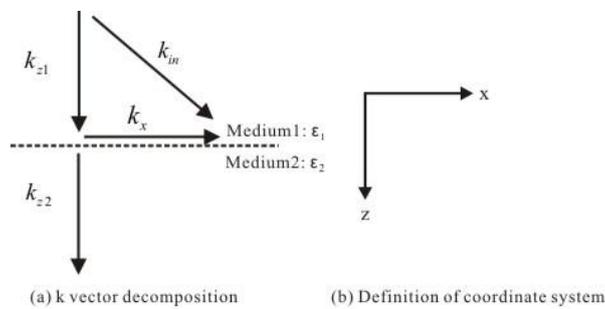
Fig. 2-2 The definition of coordinate system and the k vector decomposition in both dielectric and metal

In both medium 1 and medium 2, Maxwell's Equations can be expressed as:

$$\begin{cases} \nabla \cdot \varepsilon_i E = 0 \\ \nabla \cdot H = 0 \\ \nabla \times E = -\mu_0 \dfrac{\partial H}{\partial t} \\ \nabla \times H = \varepsilon_i \dfrac{\partial E}{\partial t} \end{cases}$$

Eq. 2-1

Considering the boundary conditions of 1) continuity of the tangential $E_x$; 2) continuity of the tangential $H_y$; 3) continuity of the normal $D_z$, they can be expressed as:

$$\begin{cases} E_{x1} = E_{x2} \\ H_{y1} = H_{y2} \\ \varepsilon_1 E_{z1} = \varepsilon_2 E_{z2} \end{cases}$$

Eq. 2-2

Use the curl equation for H in both the dielectric and the metal:

$$\nabla \times H_i = \varepsilon_i \frac{\partial E_i}{\partial t}$$ 

Eq. 2-3

Where for harmonic signals in space and time,

$$H_i = (0, H_{yi}, 0) \exp i(k_{xi}x + k_{zi}z - \omega t)$$
$$E_i = (E_{xi}, 0, E_{zi}) \exp i(k_{xi}x + k_{zi}z - \omega t)$$

Eq. 2-4

Combine Eq. 2-3 and Eq. 2-4,

$$\left( \frac{\partial H_{zi}}{\partial y} - \frac{\partial H_{yi}}{\partial z}, \frac{\partial H_{xi}}{\partial z} - \frac{\partial H_{zi}}{\partial x}, \frac{\partial H_{yi}}{\partial x} - \frac{\partial H_{xi}}{\partial y} \right) = (-ik_{zi}H_{yi}, 0, ik_{xi}H_{yi}) = (-i\omega\varepsilon_i E_{xi}, 0, -i\omega\varepsilon_i E_{zi})$$

Eq. 2-5

Therefore,

$$k_{zi}H_{yi} = \omega\varepsilon_i E_{xi}$$

Eq. 2-6

Use Eq. 2-6 to the dielectric and metal respectively:

$$k_{z1}H_{y1} = \omega\varepsilon_1 E_{x1}$$
$$k_{z2}H_{y2} = \omega\varepsilon_2 E_{x2}$$

Eq. 2-7

E across boundary is continuous, so

$$E_{x1} = E_{x2}$$

Eq. 2-8

Combine Eq. 2-7 and Eq. 2-8, so

$$\frac{k_{z1}}{\varepsilon_1} H_{y1} = \frac{k_{z2}}{\varepsilon_2} H_{y2}$$

Eq. 2-9

Considering the continuous H across boundary

$$H_{y1} = H_{y2}$$

Eq. 2-10

boundary condition 1 can be obtained:

$$\frac{k_{z1}}{\varepsilon_1} = \frac{k_{z2}}{\varepsilon_2}$$

Eq. 2-11

Then considering the k-vector decomposition, boundary condition 2 can be obtained:

$$k_{zi}^2 + k_x^2 = k_{in}^2 \xrightarrow{\ k_{in} = \frac{2\pi}{\lambda n_i}\ } = (\frac{2\pi n_i}{\lambda})^2 \xrightarrow[\omega = 2\pi f]{c = f\lambda} = (\frac{\omega n_i}{c})^2 \xrightarrow{\ \varepsilon_i = n_i^2\ } = \varepsilon_i(\frac{\omega}{c})^2 \qquad \text{Eq. 2-12}$$

Applying Eq.2-12 to the dielectric and metal respectively and solving the three equations (Eq.2-12 in two mediums and Eq. 2-11), the dispersion relation of the surface plasmons in x direction is expressed as:

$$k_x = k_x^{'} + ik_x^{''} = \frac{\omega}{c}\sqrt{\frac{\varepsilon_1\varepsilon_2}{\varepsilon_1 + \varepsilon_2}} \qquad \text{Eq. 2-13}$$

In the z direction,

$$k_{zi}^2 = \varepsilon_i(\frac{\omega}{c})^2 - k_x^2 \qquad \text{Eq. 2-14}$$

So the dispersion relation of the surface plasmon in z direction can be expressed as:

$$k_{zi} = k_{zi}^{'} + ik_{zi}^{''} = \pm\frac{\omega}{c}\sqrt{\frac{\varepsilon_i^2}{\varepsilon_1 + \varepsilon_2}} \qquad \text{Eq. 2-15}$$

As surface plasmon is an evanescent wave, $k_x^{'}$ is real and $k_{zi}$ is imaginary. In Eq. 2-15, considering the imaginary $k_{zi}$, $\text{Re}(\varepsilon_2) + \varepsilon_1 < 0$ or $\text{Re}(\varepsilon_2) < -\varepsilon_1$. That means medium 2 must be metal and its electric permittivity has a large real part and the real part is negative. This is the first condition of surface plasmon excitation. In practice, metals like gold, silver, copper, etc are used to excite surface plasmons. In this thesis, I use gold layers.

Let us use the first condition of $\text{Re}(\varepsilon_2) + \varepsilon_1 < 0$ in Eq. 2-13, in order to make sure that $k_x^{'}$ is real, $\varepsilon_1\varepsilon_2$ must be negative. In the first condition, I mentioned that medium 2 was a metal and its electric permittivity has a negative real part, so medium 1 must be real and positive or its imaginary part should be small enough to be neglected. This is the second condition for surface plasmon excitation.

There is still another condition to match the k vector. Let us rewrite Eq. 2-15 and combine the condition of imaginary $k_{zi}$,

$$k_{zi} = \pm\sqrt{\varepsilon_i(\frac{\omega}{c})^2 - k_x^2} = \pm i\sqrt{k_x^2 - \varepsilon_i(\frac{\omega}{c})^2} \qquad \text{Eq. 2-16}$$

Therefore,

$$|k_x| > \sqrt{\varepsilon_i}(\frac{\omega}{c}) \qquad \text{Eq. 2-17}$$

The right side of Eq.2-17 refers to the k vector of input from free space and the left side of Eq.2-17 is the k vector component of the input which can be used to excite surface plasmon, therefore, Eq. 2-17 tells the condition that the k vector of the input from free space is not big enough for the surface plasmon excitation. If the k vector of the input can be increased, the surface plasmon will be excited. A frequently used method is to illuminate the beam from a high refractive index medium. In this project, I use cover glass as the medium which has a refractive index of 1.52. For a metal, its dielectric constant is subject to the formulae below:

$$\varepsilon_2(\omega) = 1 - \frac{\omega_p^2}{\omega^2} \qquad \text{Eq. 2-18}$$

Insert Eq.2-14 to Eq.2-13, the dispersion relation can be expressed as:

$$k_x = k_{sp} = \frac{\omega}{c}\sqrt{\frac{\varepsilon_1\varepsilon_2}{\varepsilon_1 + \varepsilon_2}} = \frac{\omega}{c}\sqrt{\frac{(\omega^2 - \omega_p^2)\varepsilon_1}{(1+\varepsilon_1)\omega^2 - \omega_p^2}} \qquad \text{Eq. 2-19}$$

In order to show why higher refractive index medium can be used to excite surface plasmon, I plot the relation between frequency and k vector as shown in Fig. 2-3. The red curve is the dispersion relation of direct illumination from air, it does not intersect with the dispersion curve of surface plasmon (black curve); while if the beam illuminates from a higher refractive index medium like glass (blue line), the k vector is increased and it will intersect with the dispersion curve of surface plasmon (black curve) which means at the intersection point of k

vector, the surface plasmon can be excited, for incidence angle of 90º. When the plasmon (black) curve is to the left of the blue dielectric curve, excitation is achieved for incident angles below 90º.
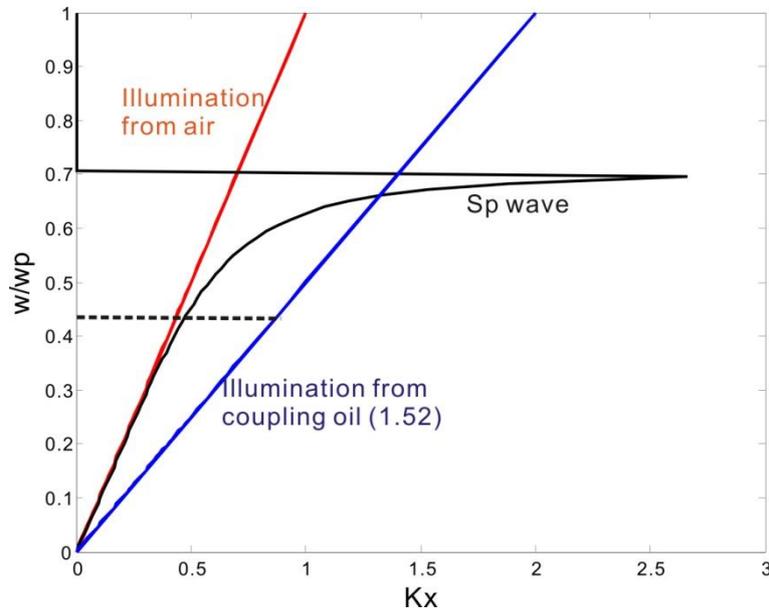


Fig. 2-3 Dispersion relations of electromagnetic waves; the red line, blue line and black curve describe the light dispersion in air, glass and the SPR non-linear dispersion relation when using metal/air.

$k_x$ consists of a real part and an imaginary part: $k_x = k_x^{'} + ik_x^{"}$. So the wave equation along the x direction can be expressed as:

$$E_x(x) = |E_0|\exp(ik_x x) = |E_0|\exp(i(k_x^{'} + ik_x^{"})x) = |E_0|\exp(-k_x^{"}x)\exp(ik_x^{'}x) \qquad \text{Eq. 2-20}$$

Then I can analyze the surface plasmon from the view points of amplitude $|E_0|\exp(-k_x^{"}x)$ and phase $\exp(ik_x^{'}x)$ separately. From the view point of amplitude, it can be seen that the surface plasmon is a decaying wave which is subject to the function of $|E_0|\exp(k_x^{"}x)$. Physically, that means with the surface plasmon propagating along the surface (x direction), the energy is absorbed and converted to ohmic heat or reradiated into the excitation medium. Therefore, a plasmon decays as it propagates. The propagation length can be evaluated from the following equation:

14

$$L_x = \frac{1}{k_x^{"}}$$ 

By measuring the real part of k-vector $k_x^{'}$, and using the following equation:

$$v_p = \frac{2\pi f}{k^{'}} = \frac{\omega}{k^{'}}$$ 

the phase velocity of surface plasmon can be measured. Where, $v_p$ is the phase velocity and f is the wave frequency.

In summary, k-vector defines the properties of the surface wave: the real part defines the phase velocity and the imaginary part defines the attenuation length of the surface plasmon. Measurement of the two terms will be described in chapter 6.

## 2.1.3 Excitation of SPs by light

As mentioned before, SPR can be excited by both light and electrons. The experiment exploits light excitation. Generally, there are two light coupling methods, diffraction grating coupling [35] and attenuated total reflection (ATR) coupling [36].

*Grating coupling*

The grating excitation is shown in Fig. 2-4.
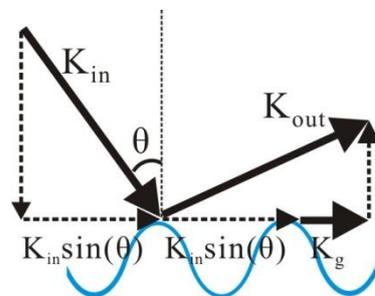


Fig. 2-4 k vector match of SPR excitation when using a grating

The momentum condition can be expressed as:

15

$$k_{sp} = k_{in} + nk_g$$

<div align="right">Eq.2-10</div>

Where, $k_{sp}$ is the k-vector of SPs, $k_{in}$ is the k-vector of incident beam, $k_g$ is the grating k

vector, n refers to the diffractive order.

*Attenuated total reflection*

Attenuated total reflection (ATR) uses the total internal reflection theory. Fig. 2-5 (a) shows

the schematic diagram for Snell's law. At the interface between two materials, according to

Snell's law, if the incident angle is $\theta_i$ , the reflected angle will be still $\theta_i$ and the transmission

angle can be calculated by the equation: $n_0 \sin(\theta_i) = n_1 \sin(\theta_t)$ . If $n_0 > n_1$, at a particular angle,

$\theta_t$ can exceed $90°$ as shown in Fig. 2-5 (b). This case is called the total internal reflection and

the particular angle is called the 'critical' angle, which can be calculated by: $\sin^{-1}(\frac{n_1}{n_0})$ .

When the beam incidents around the critical angle, an 'evanescent' wave generates at the

boundary of the interface, which is the SPs. If $n_0 = 1$ that means the light incidents from air,

there is no total internal reflection. However, if locating a higher refractive index material

( $n_0 > 1$ ) at the light incident space, the total internal reflection will be possible. And

according to the definition of k vector, the k vector will be increased to be $k = n_0 k_{free}$ . This is

the principle of the ATR surface plasmon excitation configuration. The project exploits ATR

configuration. According to the specific requirements, different kinds of ATR configurations

were devised.

(a) Schematic diagram of Snell's law        (b) Total internal reflection
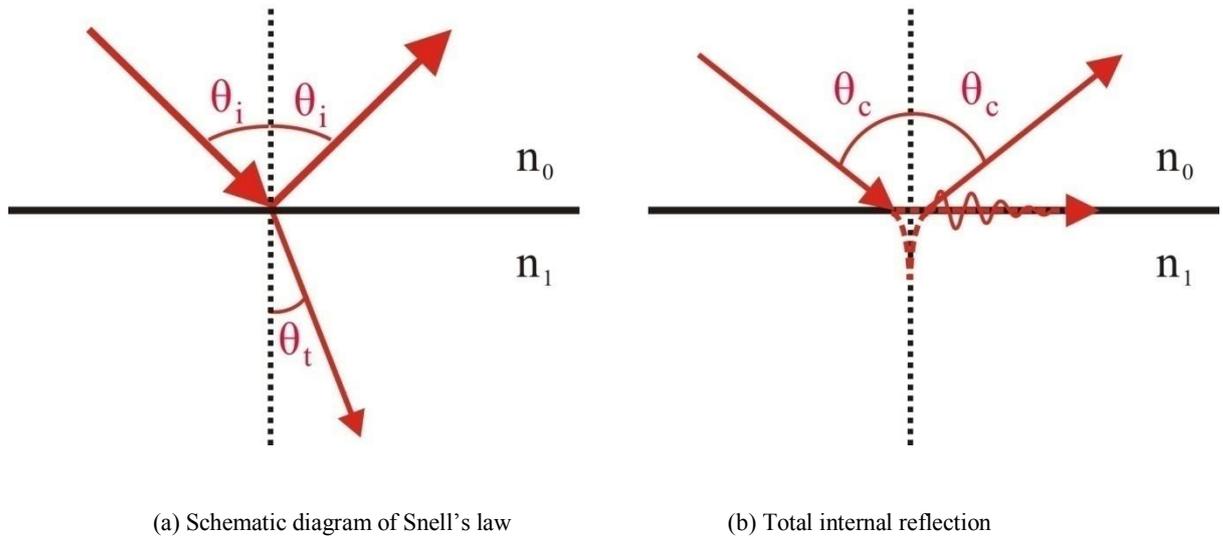
Fig. 2-5 Snell's law and total internal reflection

Usually, there are two kinds of configuration in the category of prism coupled ATR, one is Kretschmann alignment[37] (Fig. 2-6 (a)), the other one is Otto configuration[38, 39] (Fig. 2-6 (b)).



(a) Kretchmann structure        (b) Otto structure
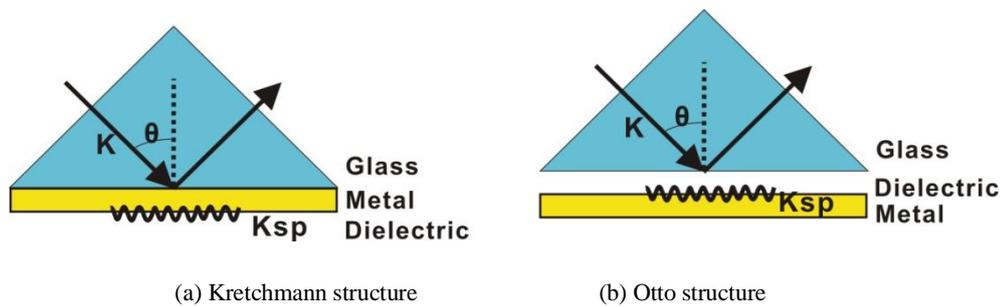
Fig. 2-6 prism based SPR excitation structure

Both of the prism structures can be used to excite SPR. Firstly, the illumination is incident from a high refractive index, e.g. BK7 glass, thus the k-vector is increased to match that of the surface plasmon; the condition can be expressed as: $nk\sin(\theta) = k_{sp}$; Secondly, a metal layer like gold, silver, copper, etc. is coated. The only difference between the two configurations is the location of the sample. For the Otto structure, the dielectric is located in the gap between the coupling glass and metal layer as shown in Fig. 2-6(b), while for the Kretschmann the sample is located in free space thus one has space to locate the sample,

which is more convenient to use and combine with other techniques[40] . Most SPR sensors exploit the Kretschmann based structure.

As another big application of SPR is in bio-imaging, obviously, prism based SPR excitation is incompatible with objective lens based microscopy. Can I use a similar coverglass based sample structure in the SPR excitation setup and remove the prism? By analyzing the prism based SPR excitation system like the Kretchmann setup, it can be found that the function of the prism is to offer a high refractive index and therefore to increase the k-vector of the illumination to match with that of the surface plasmon. In 1972, Abeles[41] analyzed the behaviour of a surface film on SPs mathematically. Later in 1977, Azzam and Bashara [42] gave considerable insight into the behaviour of SPs on the variation of the reflection coefficient with incident angle from a thin metal. From then, the sample structure was expanded to be the so-called sandwich structure and the prism is removed as shown in Fig. 2-7. The momentum condition of $k\sin(\theta) = k_{sp}$ is still fulfilled. More details on objective based SPR excitation can be found in the SPRM section later in section 2.3 of this chapter.
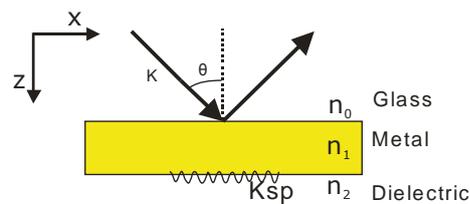


Fig. 2-7 three layer sandwiched sample structure

## 2.1.4 Properties of surface plamon resonance

In section 2.1.3, I discussed the excitations of SPs. Here, I will provide more information on the SPR properties and some simulations are done to show the influence of illumination polarization and influence of metal. Different methods have been used to analyze surface plasmon, like the theories of waveguide, integral method, differential method, Fresnel

equations etc [32, 43]. In this project, I adopt the Fresnel equations method, which is solutions to Maxwell equations subject to the appropriate boundary conditions for p- and s-polarization, to simulate the uniform samples, while the theory of rigorous wave coupled analysis (RCWA) can be introduced for the grating samples. As this thesis mainly focuses on the experiment part, I do not discuss RCWA and  more details on the RCWA theory and simulations can be found in Pechprasarn's thesis[3].

*Fresnel equations*



(a) Two layers                          (b) Three layers
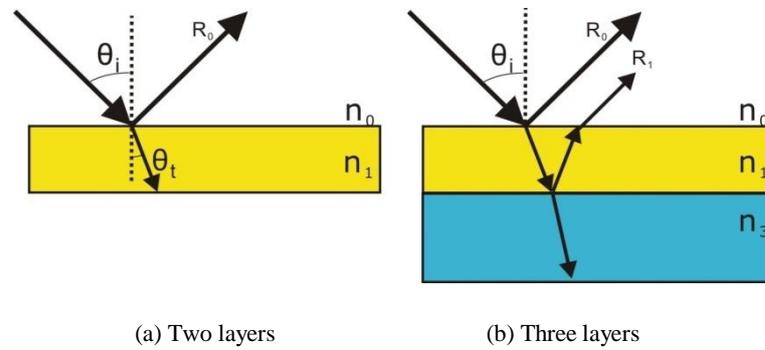
Fig. 2-8 Sample structure for Fresnel equations

The basic simplest Fresnel equations example is the two layer sample structure (Fig. 2-8 (a)).

$$t_p = \frac{\cos(\theta_i)\sin(\theta_t)}{\sin(\theta_i + \theta_t)\cos(\theta_i - \theta_t)} \qquad \text{Eq. 2-23}$$

$$t_s = \frac{2\cos(\theta_i)\sin(\theta_t)}{\sin(\theta_i + \theta_t)} \qquad \text{Eq. 2-24}$$

$$r_p = \frac{\tan(\theta_i - \theta_t)}{\tan(\theta_i + \theta_t)} \qquad \text{Eq. 2-25}$$

$$r_s = \frac{\sin(\theta_i - \theta_t)}{\sin(\theta_i + \theta_t)} \qquad \text{Eq. 2-26}$$

If more layers are used, like three or four layers, the reflections from all the interfaces should be considered. For instance, in Fig. 2-8 (b), both of $R_0$ and $R_1$ should be added together. If there is no specific indication, the simulations in this thesis are based on the multi-layerer Fresnel equations. Details on the multilayer Fresnel equations can be found in [44, 45]. I investigated the three layers and four layers behaviours in this thesis and the code for the Fresnel equations were written by Somekh. All the simulations in this thesis used this code as one of the basic functions. I used this function of the Fresnel equations to calculate the refractive coefficient called $r_p$. The modulus of $r_p$ gives the amplitude behaviour of surface plasmon and the tangent of $r_p$ demonstrates the phase behaviour of surface plasmon.

*Influence of illumination polarization in SPR excitation*

There are two kinds of beam polarization states, s- and p- wave, also called TE (Transverse Electric) and TM (Transverse Magnetic). In the first SPs introduction section, I reviewed the discovery history of SPs and both s and p anomalies existed for grating coupling, although the p anomaly only existed for gratings with deep grooves. Here a question needs to be asked: for the ATR coupling, can both s and p polarized illumination be used to excite surface plasmon? A simulation on a simple three layer sample structure, which is a coverglass substrate coated with 46nm gold is applied to show the amplitude and phase variations of the reflection coefficient, as shown in Fig. 2-9. The subfigure of (a) demonstrates the amplitude curve and (b) shows the phase curve. If the polarization of p-wave is used as the blue curves in (a) and (b), there are an amplitude dip and dramatic phase variation in the amplitude and phase curves respectively, which show the presence of SPR excitation. The reason for the presence of the dip is that the energy is coupled to SPR around the plasmonic angle and then to ohmic heat when propagating along the surface. The red curves in the two subfigures refer

to the amplitude and phase changes when using s incident. I draw the conclusion that only the p wave can be used to excite SPR.



(a) Amplitude response          (b) Phase response
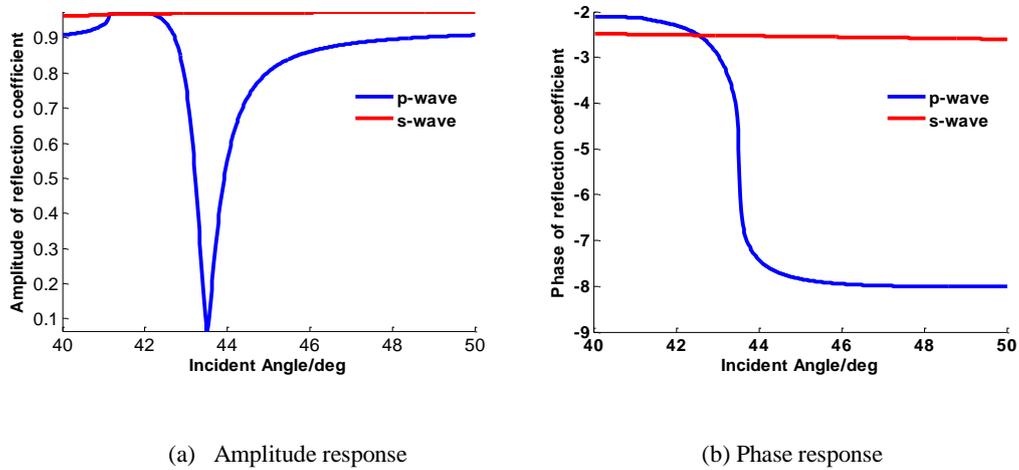
Fig. 2-9 Comparison of SPR excitation by using p and s polarized illumination

## *Influence of metal to SPR*

1)  Electric field enhancement by coating metal layers

At the very beginning of the SPR discovery, the importance of metal was not realized. In 1936, John Strong[46] showed Wood's anomaly by using different metallic grating with same period and demonstrated  that it was the metal that influenced the Wood's anomaly and even the locations of the anomalies. Surface plasmon wave is physically an effect of field enhancement. That means a dramatic electric field generated on the interface of gold/dielectric and thus tiny variations on the interface will cause a big effect on the SPs, which is one reason that SPR can provide a much higher sensitivity than other techniques. Here, a simulation as shown in Fig. 2-10 was used to demonstrate the influence of metal and the field enhancement quantitatively. The red curve demonstrates the electric field of SPs when using a three layer sample structure (1.52 coverglass, 50nm gold and air); while the blue curve shows the electric field if there is no gold between the coverglass and the air. The maxima around the plasmonic angle show a dramatic difference. That is the reason why a

metallic layer is required in the SPR excitation and the reason why SPR behaves excellently for sensing and imaging.
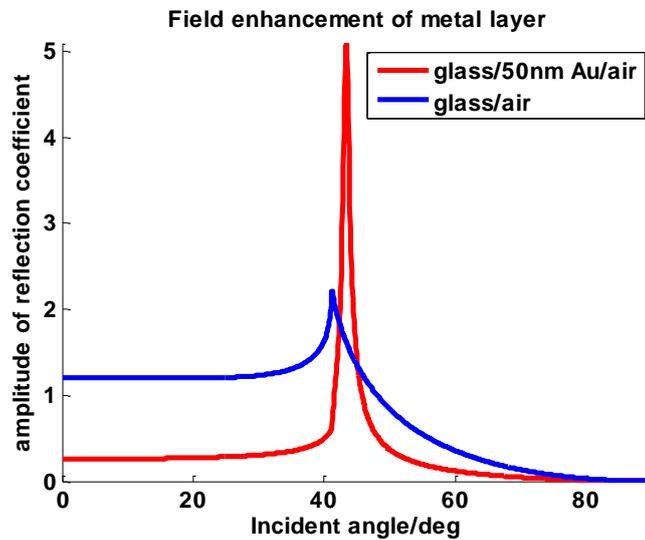


Fig. 2-10 Comparison of the excited electric field enhancement when using a sample structure with gold layer (red curve) and without gold layer (blue curve)

2) Selection of metals for plasmon sensors

It was  discussed above the conditions of SPR excitation and mentioned that many metals can be used to support SPR. Here the metals are selected to be used for SPR excitation based on the following criteria: 1) To be able to excite SPR in the visible wavelength range so we can use lasers which are relatively cheap and used commonly in optical lab to excite SPR; 2) To be stable in both air and especially in liquid, like water, as the main application of SPR is in biology. For the first criteria, most metals can be excluded. Usually, only aluminium (Al) [47], gold (Au), copper (Cu), silver (Ag), etc[48] are used. Application of Al in SPR is rarely reported owing to its higher attenuation and much shorter propagation length owing to the big imaginary part of permittivity. For the second criteria, it is well known that usually, noble metals are more stable than oxidizing metals.  In practice, silver and gold are the most popular metals which are used to excite SPR [49, 50]. Cu is used less frequently. Silver was used in the first SPR system because it has low loss. However, considering the main

application of this project in biological area, I will not choose Ag. The reason is that silver is less stable, forming $Ag_2S$, which may do harm to the biological samples, and also affects the consistency of any measurements taken. In practice, gold is widely used in SPs excitation. I adopt gold in this project.

3) Influence of gold thickness

After choosing gold as the metal to excite SPR, I still need to consider the influence of gold thickness. A simulation comparison by varying the gold thickness from 30nm to 100nm is done here. The results show that i) The thickness of gold should not be too thin or too thick, or else the SPR would disappear (see the 10nm and100nm curves in Fig. 2-11 (a) and (b)); ii) Different thicknesses refer to different sensitivities. At around 46nm, the SPR dip on the intensity curve is deeper and the phase has a steeper slope which means it is more sensitive than the other thickness to the refractive index variation; iii) although different thicknesses provide different sensitivities, the resonance angle is almost the same, all around 43.5 deg.



(a)                                (b)
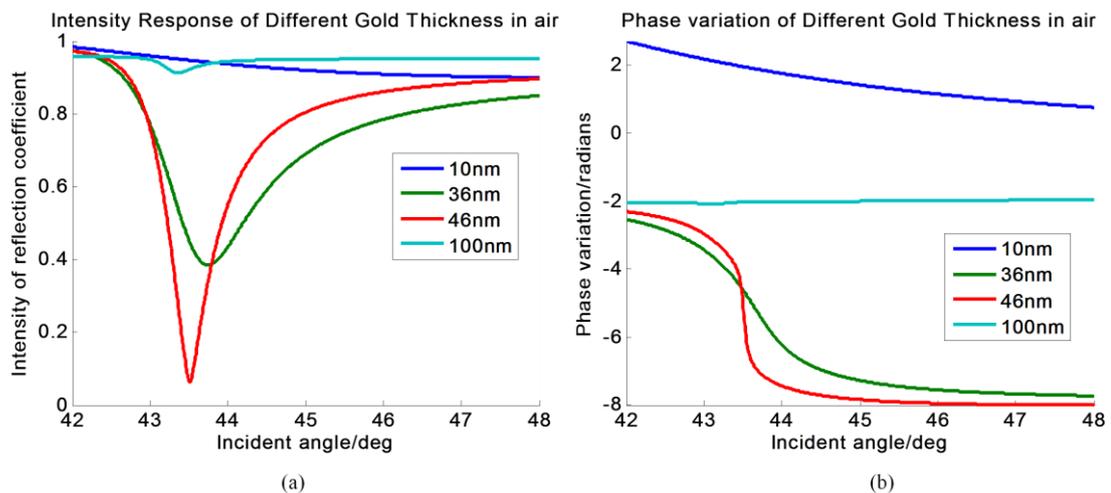
Fig. 2-11 Comparison of SPR excitation by using different gold thickness samples (glass/gold/air)

I can conclude that the metal layer is able to enhance the electric field dramatically; gold is suitable for biological related applications and all the experiments in the thesis use gold;

Thickness of gold layers can influence the sensitivity and approximate 46nm of gold can provide good sensitivity. I adopted approximately 50nm gold in this project. It is the dramatically high sensitivity that makes the SPR a powerful tool for sensing, especially bio-sensing. More details are given in the next section.

## 2.2 SPR sensing

### 2.2.1 Review of SPR sensor

Thanks to the pioneers' work in SPR foundations and following researchers' effort in the realization of instrumentation, SPR based sensors have not only been possible but also been boosted in the last few decades because of the demands of customers requirements in semiconductor, biological, chemical and pharmaceutical areas [51]. There have been many famous companies which are developing SPR related instruments especially SPR sensors, like GE Biacore, Attana AB, AutoLab, Biosensing Instrument, ICx Nomadics, Hofmann Sensorsysteme , and Biosuplar, etc [51]. Among them, Biacore is the most famous and leading one, which sets a gold standard for SPR devices. Both the laboratory and commercial SPR sensing instruments are designed to sense and measure quantitatively the interactions of membranes or biopolymers, like protein-protein, protein-DNA, antigen-antibody binding, etc[52-54]. Both the laboratory and commercial SPR sensors share the advantages of high sensitivity, label-free and real time detection. Label-free means that no bio-markers or analyte are required in SPR sensing, compared to other kinds of techniques, like fluorescent sensor which needs fluorophores to emit fluorescent light. Any variations on the surface of metal can be detected directly without labelling the sample for SPR sensors. As the real time detection, as the interactions can occur very quickly and no delay time is needed, the detection of SPR sensors can be operated in real-time. Another feature of SPR sensors is that it can provide relatively high sensitivity. Even commercial instruments can present the

sensitivity as high as around $10^{-7}$ refractive index units (RIU) using single point detection [55].

There are also limitations of SPR, such that there is no inherent analyte selection as shown in Fig. 2-12 (a). Although the density of molecules can affect the refractive index of the dielectric and the tiny variations can be detected by the SPR sensor, it is difficult to identify the material. However, with the efforts of biologists and chemists, more and more antibodies have been studied and put into practice, and therefore this problem has been being solved. Fig. 2-12 (b) shows how the selection works. The procedure is called binding. The analyte (red 'Y' in (b)) are immobilised on the surface of sensor substrate and its binding partner (red 'spot' in (b)) is injected in through the flow cell. With the procedure of the binding, the refractive index will change and the variation is detected by SPR sensor in real-time. This is the principle of analyte selection. By using several channels, the selection of several analyte is possible as shown in Fig. 2-12 (c). Of course, more effort is still been needed, like how to select specific analyte, how to make the sensor sensitivity higher, how to increase the dynamic sensing range.
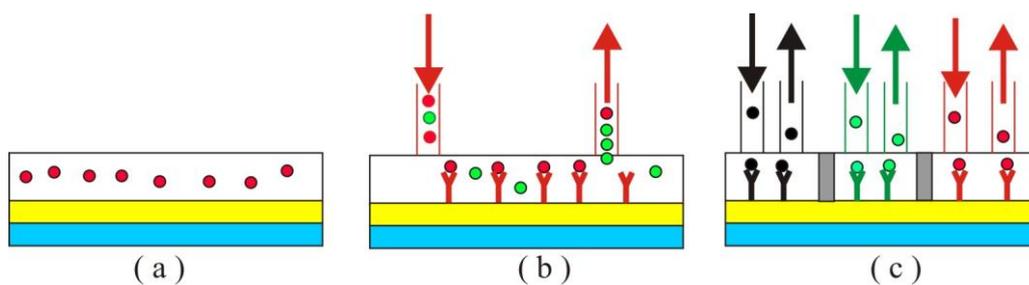
Fig. 2-12 SPR binding procedure

## 2.2.2 Principles of SPR sensor

A sensor is a device which can convert a quantity which is difficult to measure directly into measurable signals. SPR sensors can convert the variations on the surface of metal to be some

detectable variables, like an optical intensity change, phase variations, resonance angle movement, or even excitation wavelength difference, etc. According to which coupling variables are used like resonance angle, resonance wavelength or even polarization state, different kinds of SPR sensors are designed. As in this project, I fixed the illumination source to be a He-Ne laser, only the resonance angle coupling is discussed.
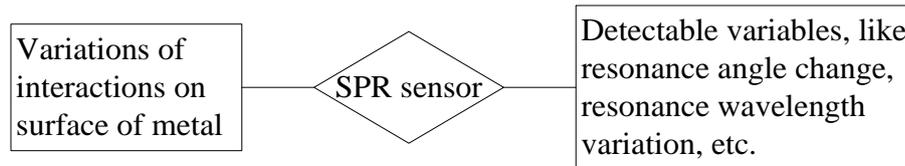


Fig. 2-13 Schematic diagram of SPR sensor

### *Influence of dielectric refractive index*

SPR is relatively sensitive to the variations of the dielectric properties, for example, that of the refractive index. As the resonance angle also varies with other variables, like the wavelength, the kind of metal, metal thickness, the substrate coverglass, etc, here, I fix all of them, and just change the refractive index. Fig. 2-14 shows the change of resonance angle $\theta_p$ when 5nm ITO (indium tin oxide) is coated on the surface of gold ((a) is the amplitude figure and (b) is the phase figure). It can be see that 5nm layer gives a very large change in SPR signal.  Fig. 2-14(c) shows the relation between the resonance angle and the dielectric refractive index. It is approximately a linear curve and it can be used to measure the sample quantitatively.
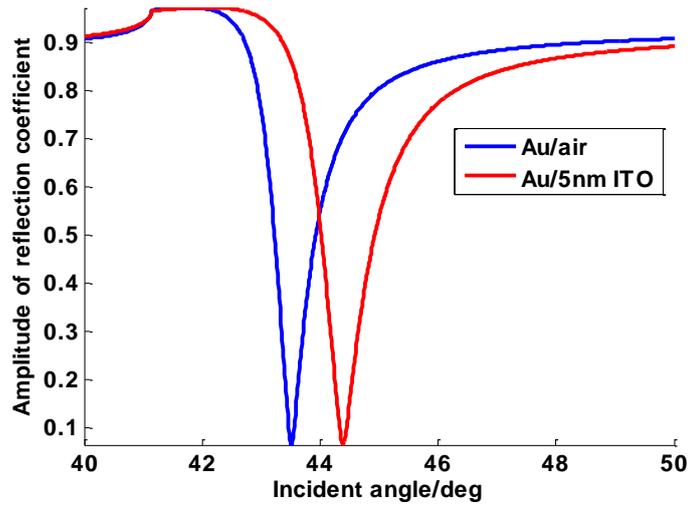
(a)
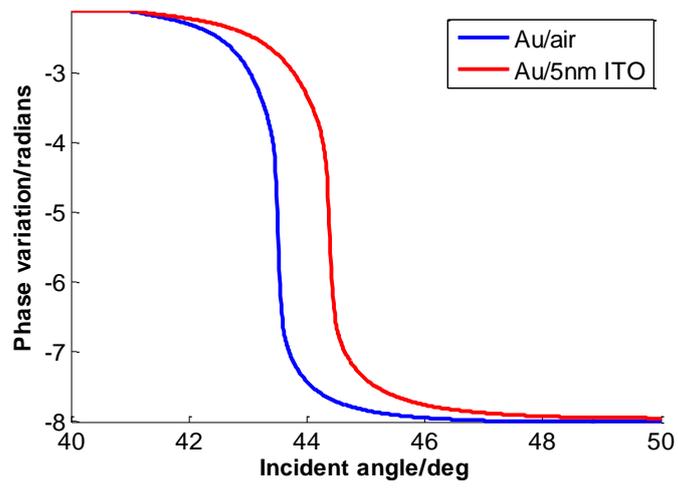


(b)
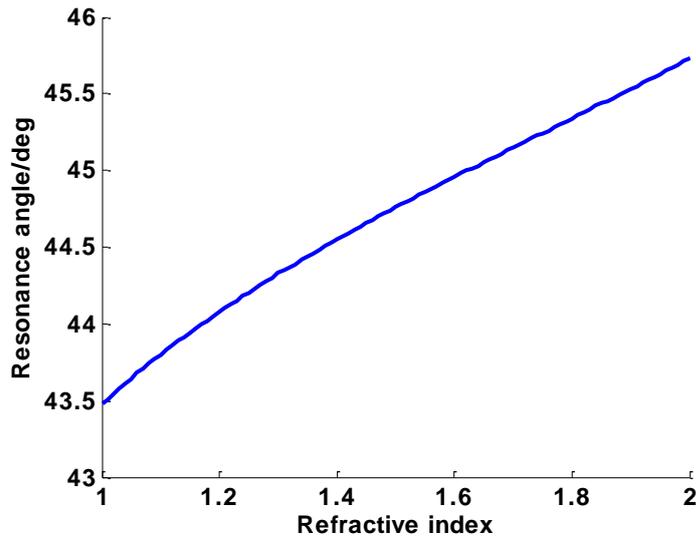
(c)

Fig. 2-14 Influence of the reflection coefficient against the dielectric refractive index variation. (a) is the amplitude response; (b) is the phase response; (c) shows the relation between the resonance angle and the dielectric refractive index.

## *Influence of dielectric thickness variation*

In this part, I fix the refractive index and vary the thickness of the coating. Fig. 2-15 (a) shows the amplitude and the phase variation when the thickness of ITO varies from 5nm to 10nm. As the resonance condition changes, a higher incident angle is needed to excite SPR. (c) shows the relation between the resonance angle and the dielectric thickness. It is approximately a linear curve and I can use it to measure the coating properties quantitatively.
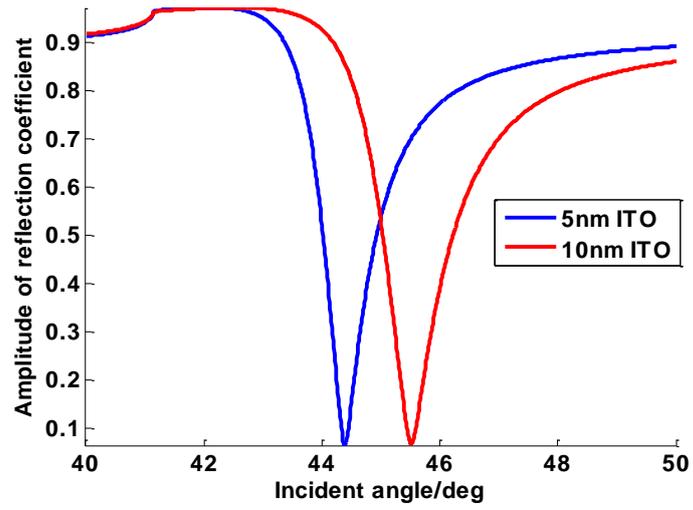
(a)
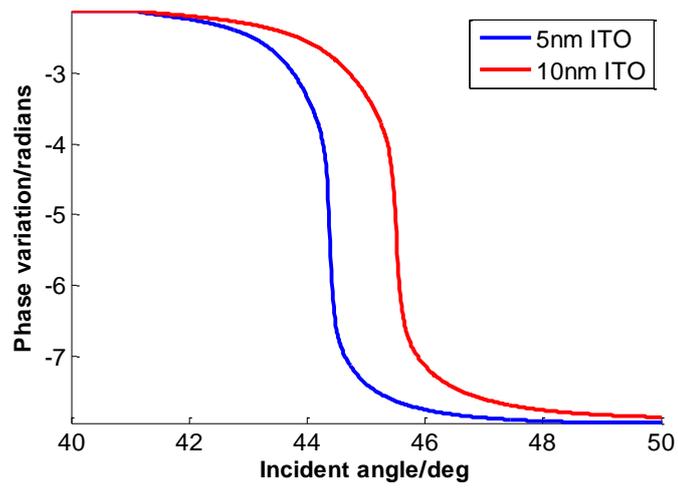


(b)
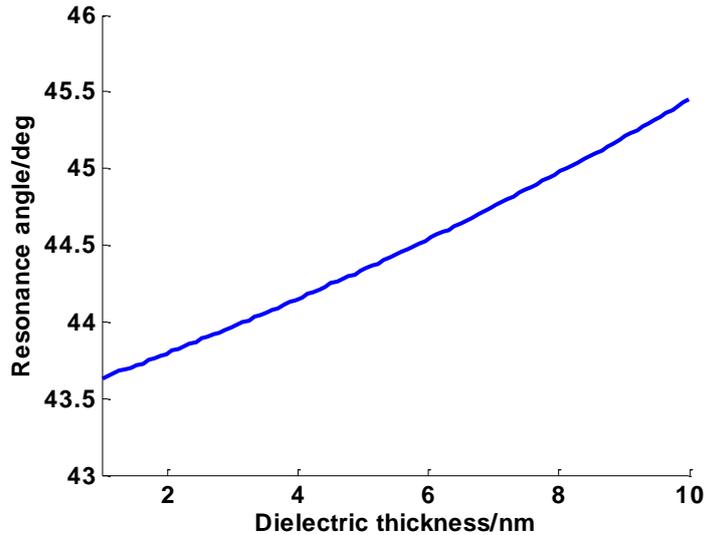
(c)

Fig. 2-15 Influence of dielectric thickness variation against the dielectric film thickness. (a) is the amplitude response; (b) is the phase response; (c) shows the relation between the resonance angle and the dielectric film thickness.

## 2.2.3 Phase detection *v.s.* intensity detection

Both amplitude (intensity) and phase can be detected in SPR sensors. According to which variables are detected, SPR sensor can be classified whether they detect intensity or phase. Many researchers have claimed that phase detection can provide a lower limit of detection, higher throughput [51] and at least two orders of magnitude higher sensitivity than conventional intensity measurement [56, 57]. Kabashin claimed that the following reasons promise the higher sensitivity for phase based SPR sensor:

Firstly, Kabashin claims that phase shift only occurs at the strict resonance angle while amplitude changes show a small range around the strict resonance angle as shown in Fig. 2-16, where the phase variation shape has a steeper slope than the intensity response around the resonance angle. It means that with the same input variation (like refractive index variation), the phase information has a higher sensitivity than the intensity response. A

30

simulation is shown here to compare the difference between amplitude detection and phase detection quantitatively. As biological environment is a big application field of SPR, here, take the cell environment as an example, letting the refractive index changes from 1.33 to 1.34, seeing Fig. 2-17 which might indicate that the phase response provides higher sensitivity.
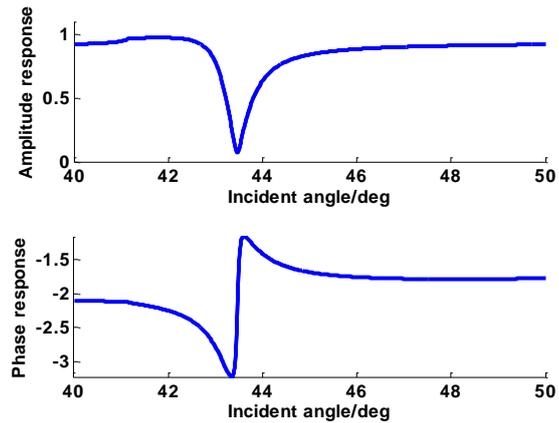


Fig. 2-16 comparison between the amplitude response and the phase response

He also claimed that under a proper design of a detection scheme, phase noise can be orders of magnitude lower compared to amplitude noise, which results in a much better signal-to-noise ratio. He also argued that phase offers much better possibilities for signal averaging and filtering, as well as for image treatment.
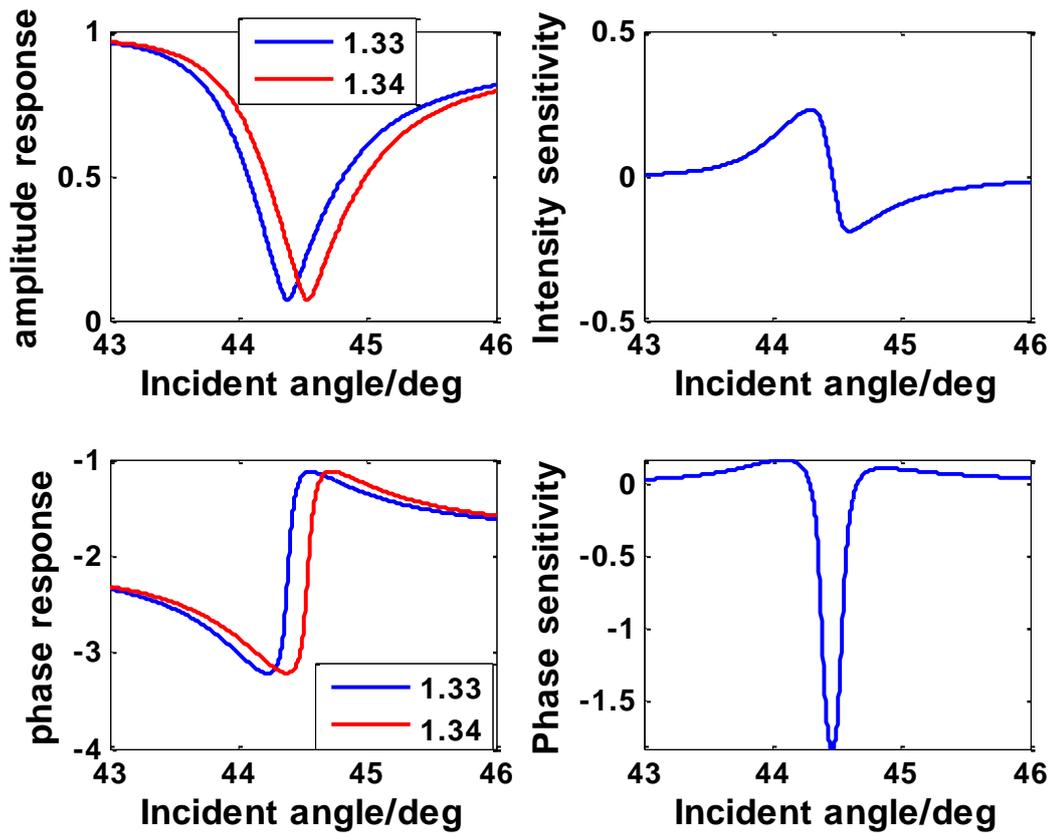
Fig. 2-17 Sensitivity comparison between intensity and phase when $n_{dielectric}$ varies from 1.33 to 1.34

One difficulty in phase detection is that it cannot be detected directly as intensity and it needs to be interfered with a reference. Usually, an interferometer is required. This project exploits the phase detection.

## 2.2.4 Summary of SPR and SPR sensing

In this section, I discussed the properties of SPR and showed the influence of illumination polarization and that of metals. I draw the conclusion that only a p-wave can be used to excite SPR and fix the metal layer to be gold and the thickness to 50nm. In the influence of metal section, I described the electric field enhancement effect which provides the high sensitivity of SPR. Then I discussed the influence of dielectric, including the refractive index and thickness. After that, I analyzed the relation between the plasmonic resonance angle and the dielectric thickness. Owing to this approximate linear relation and the high sensitivity, SPR

has mainly been applied as a sensor, especially after the introduction of Kretschmann ATR configuration. Owing to its high sensitivity in the variation of dielectric refractive index and thickness, the SPR sensor can be used to detect the gas [58, 59] or other chemical materials variations in the field of chemistry, binding of monolayer protein [60, 61] in biology, viruses [62] and cells [63] in bioscience, drugs molecular sensing [64, 65] in pharmacy, etc. Another big potential application of SPR is in the field of microscopy. This project is one of the efforts in developing surface plasmon resonance microscopy (SPRM).

## 2.3 Surface plasmon resonance microscopy (SPRM)

### 2.3.1 Introduction to surface plasmon microscopy

In the late 1980s, SPR was introduced to the imaging field. Since then, surface plasmon imaging has been a very popular topic. Surface plasmon resonance microscopy (SPRM) is optical microscopy which uses the evanescent confined surface plasmon wave as a tool to observe tiny surface changes, which is usually difficult to be observed by conventional microscopy of continuous propagating waves. The concept of SPR imaging was proposed and SPRM firstly invented by Yeatman and Ash in 1987 [13] with a lateral resolution of 25 microns. Compared to other kinds of microscopy techniques, SPRM provides several advantages, like no vacuum, no addition of probes, or mechanical contact and no fluorophore. It is just these advantages that make the SPRM attractive since the absence of fluorophores reduces photon damage and photo bleaching. Although SPRM is a relatively young technique compared to other kinds of microscopy, it has been proving itself as a promising and powerful front-edge technology. Similar to other microscopy, SPRM can detect intensity or phase changes, classified as intensity SPRM and phase SPRM respectively as shown in Fig. 2-18. As mentioned above, for a phase detection device, interferometer is required. Different kinds of interferometer can be used. In order to distinguish the conventional two arm setup

and the confocal one proposed in this project, here, I define them as interferometric SPRM and confocal SPRM.
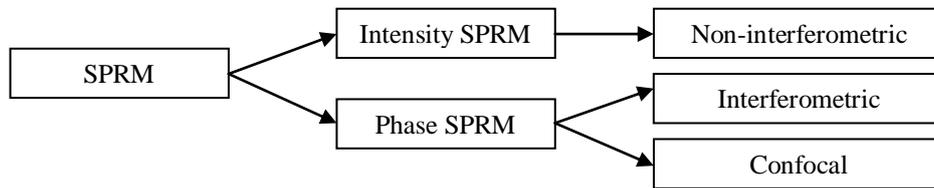


Fig. 2-18 Classification diagram of different type of SPRM in this thesis

Since the invention of SPRM, intensity based measurements have definitely been dominant, although phase based SPRM is also developing slowly. In this section, I will review the conventional intensity based SPRM and discuss its limitations, then introduce the interferometric one and finally the confocal one. As both the interferometric SPRM and the confocal SPRM apply the so-called *V(z)* technique, it is necessary to describe the *V(z)* technique.

## 2.3.2 Non-interferometric intensity based SPRM

In the 1987 and 1988[12, 13], two kinds of SPRM were invented by Yeatman and Rothenhausler separately. Both of them were used to detect the intensity and exploited the Kretchmann configuration (prism based) setup. Yeatman applied the specimen thickness modulation and built a bright field microscope. One example of SP microscopy is described in [12]. When a uniform beam illuminates the sample at a fixed angle where SPs are excited, the reflected beam was reduced (Fig. 2-19). It was the first time that the imaging contrast mechanism was described (Fig. 2-19). At the illumination angle of $\theta_0$, SPR was excited only at the uncoated part and the energy was converted to into Ohmic heat and there was almost no directly reflected light, while the excitation conditions were not fulfilled at the layer coated part and no SPR was excited that most part of the light was reflected. By detecting the

returned reflection light, image of the specimen was obtained with a contrast to show the uncoated part and the coated part. The change in local SP resonance conditions is the basic contrast mechanism of SPRM. In the previous case since the intensity was detected, I call this kind of microscopy as intensity based SPRM. Later, other intensity based SPR microscopes were reported [66, 67].
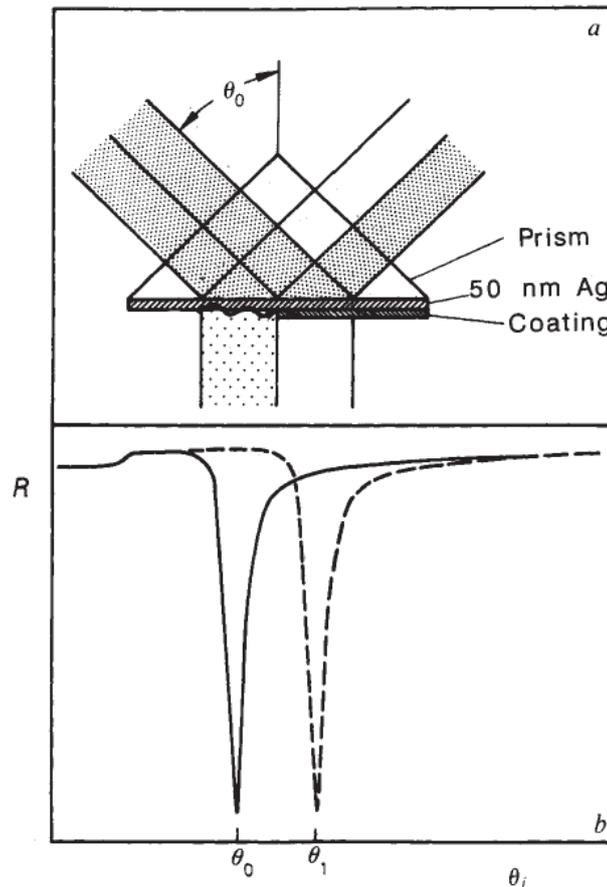


Fig. 2-19 Imaging contrast mechanism of the SPRM [12]

The first invented SPRM achieved relatively high sensitivity [12, 40, 68, 69] but poor lateral resolution of around 25 microns which is much lower than that of conventional optical microscopy and presents a big limitation for its further application. Therefore, methods to improve the lateral resolution for a SPRM have been a popular topic. Several attempts were made here: near field technique[70], using Al to replace gold to excite SPR[47], and using a tightly focused beam to collect more spectrums of SPR[36], etc.

1) Near field techniques

Some researchers proposed scanning near-field optical microscopy[70] or a far-field technique by using guided SPs coupling[71] to optimize the lateral resolution. The two techniques do improve the lateral resolution but share the problem of inconvenience in aqueous media or are incompatible with other conventional optical techniques, and are thus not suitable for biological application.

2) SPRM on aluminium

In 1999, Giebel et al proposed a method to improve the lateral resolution by using Al as the excitation metal layer owing to its shorter propagation length[47]. However, because of its large positive imaginary part of the dielectric permittivity, the attenuation is too severe for higher sensitivity which will be introduced later in 2.3.3 section). In this project, I still apply gold as the metal layer to excite SPR.

3) Oil-immersion high NA objective excitation

During the first ten years of SPRM, prism based SPR excitation dominated and resolution of SPRM was usually tens of microns. By analyzing the principles of SPRM, traditional prism based SPRM used plane incident in a particular direction onto the metal surface and just the specific angle of spectrum was collected as the reflected signal, and thus the actual NA is dramatically low. In 1998, Kano proposed to use a tightly focused beam[36] and applied a large numerical aperture (NA) oil immersion objective lens to excite SPR. This objective lens based of SPRM can collect more angular information than traditional prism based SPRM and can improve the lateral resolution of SPRM. Another big advantage of this objective lens SPR excitation is that the new setup is compatible with conventional non-SPR optical microscope. This makes SPRM more easily be accepted by biologist. Since the invention of objective lens based SPRM, it has been widely used in SPRM. This project exploited oil-immersion high NA objective lens to excite SPR (ZEISS 100X NA1.25 and 1.45).
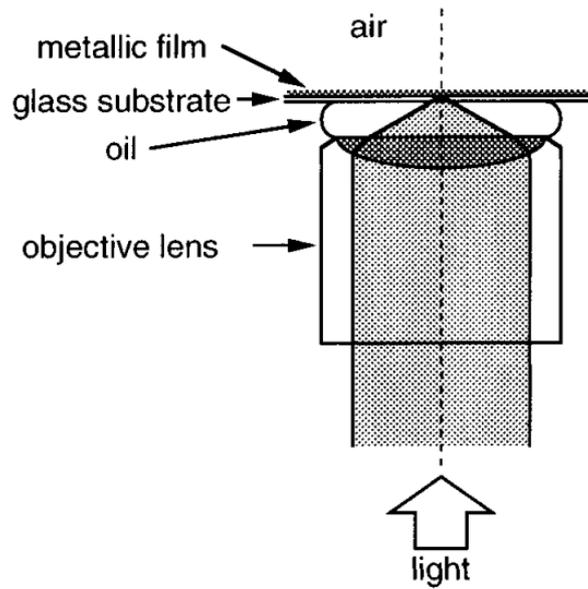
Fig. 2-20 SPR excitation by using an oil-immersion objective lens invented by Kano[36]

By comprehending all these techniques, some advanced non-interferometric SPRM were reported. According to the image formation methods, I classify them intro two kinds: scanning and wide-field. Obviously, scanning can be time-consuming. Usually, it is less popular than wide-field, unless it provides other advantages, like better resolution or higher sensitivity. Two kinds of scanning SPRM exist: sample scanning and back focal plane scanning.

### *Sample scanning SPRM*

As I do not exploit a prism in this project, I only discuss the objective based scanning system. One typical sample scanning intensity SPRM was proposed by Kano in 1998. Its system setup is in Fig. 2-21. A small sample scanning schematic diagram is also provided in the figure. This system is a transmission SPRM and sample was scanned by moving the motorized stage.

37
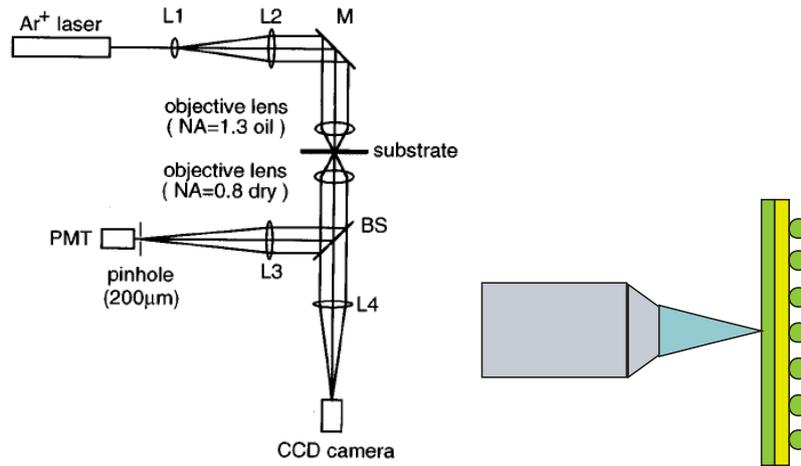
Fig. 2-21 Optical setup of Sample scanning SPRM by Kano [36]

The image from this experiment setup provided a much higher lateral resolution than the prism based SPRM by Yeatman in 1987. Because in this system, by using the high NA oil-immersion objective lens to focus the illumination beam, the SPR can be excited in a relatively localized region, Kano claimed that in this situation, the lateral resolution was limited by the sample structure, rather than the decay length of SPs. Sample scanning system has been successfully applied to measure film properties [72-74].

*Back focal plane scanning SPRM*

In 2000, Kano devised another scanning SPRM which is to scan the back focal plane[75]. He employed the SPs as a sensing probe [12, 66, 67]to measure the refractive variations along the metal interface. The system setup is in Fig. 2-22. The SPR excitation conditions vary with different sample points and the dips on the back focal plane vary. The dips positions were recorded by the CCD. By locating the dip ring position, the image was obtained.
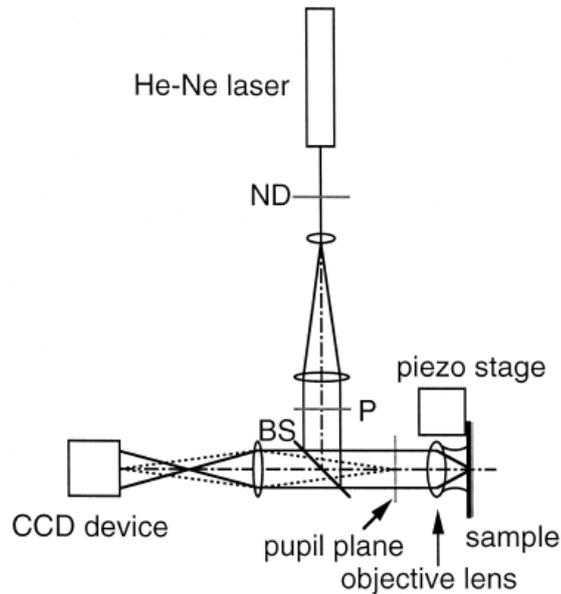
Fig. 2-22 system setup of back focal plane scanning SPRM by Kano [75]

Although the concept in this system is novel and the system setup is relatively simple to construct, the lateral resolution of this system, 1.5 microns, was a little poorer than the sample scanning one. The main reason is speckles were generated on the BFP image because of the coherent laser illumination source.

*Wide-field SPRM*

In 2004, a wide-field surface plasmon microscope was developed by Zhang [76]. Instead of using oil-immersion high NA objective, she exploited a solid immersion lens to enlarge the NA of a long working distance objective lens (Mitutoyo, NA=0.42) and used a diffuser to break up the speckles owing to high time spatial coherence of the He-Ne laser and to build up a Kohler illumination system for the wide-field SPRM system. The optical setup is in Fig. 2-23. Two CCD cameras were used to detect the wide-field image and the back focal plane image. Since the system is wide-field, the back focal plane image is the average response of the whole sample in the field of view. The wide-field images both in air and water were obtained.
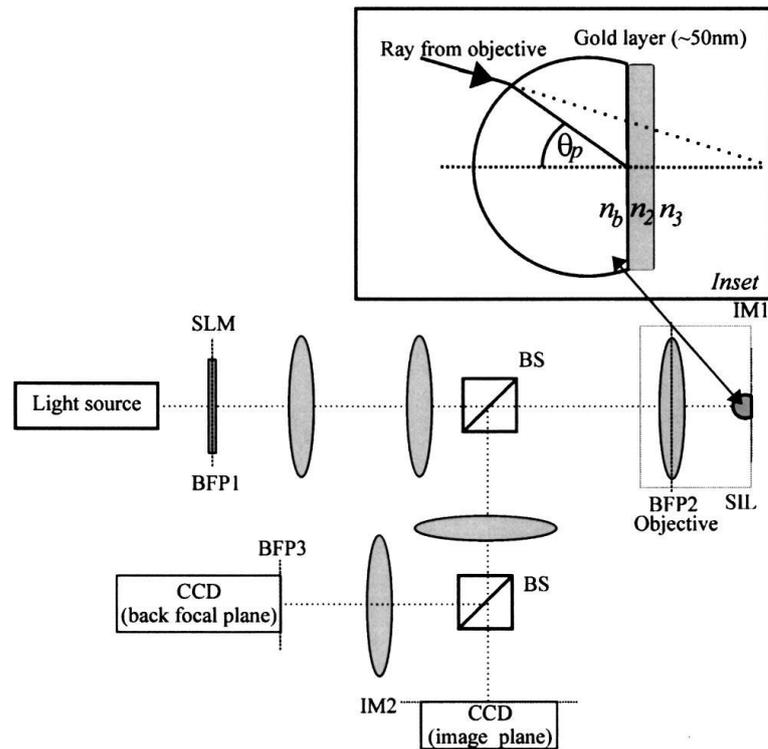
Fig. 2-23 Optical setup of the SIL wide-field objective [76]

In 2006, Zhang[34, 77] made the optical setup more convenient to use by splitting the sample part into a two-piece SIL by using a conventional BK7 coverglass as the substrate of the sample. Later, a high resolution angle scanning wide-field surface plasmon resonance microscope was built by Tan[45]. It can measure the variation of sample quantitatively. In Tan's system, the SIL part in Zhang's system was replaced by a high NA oil-immersion objective lens (ZEISS, 60X, 1.49NA) and a much easier wide-field system was built up by Tan[45]. Tan claimed a lateral resolution of 6.5 μm in air and 7.6 μm in water when the grating direction is parallel to the illumination polarization and 4.3μm in air and 4.8 μm in water when the grating direction is perpendicular to the illumination polarization.

## 2.3.3 Limitations of non-interferometric SPRM

At the very beginning of the SPRM invention in 1987[13], Yeatman mentioned that the lateral resolution might decrease with the higher 'vertical' resolution (sensitivity). Until 1994, Berger analyzed the relation between decay length, lateral resolution and sensitivity[40]. He

40

deduced that the lateral resolution of SPRM was limited by the decay length of the SP (propagating length). In order to demonstrate his claim, Berger analyzed the relation between wavelength and reflectance difference, and the relation between wavelength and decay length, which demonstrated clearly that decay length is related to the reflectance difference (Fig. 2-24). It was the first time to show that lateral resolution of SPRM was related and confined by the decay length of SP wave, rather than the diffractive limit of conventional optical microscopy.
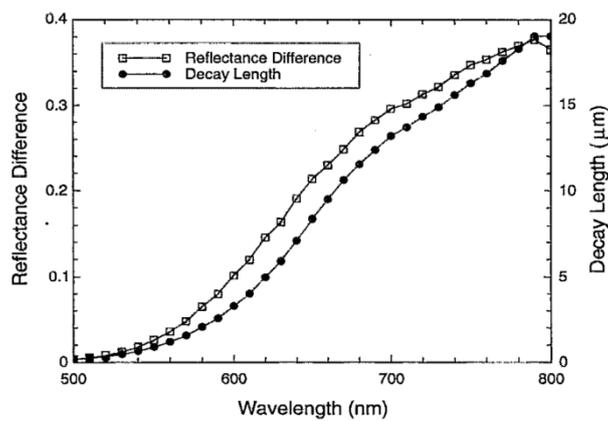


Fig. 2-24 Reflectance difference for bare gold and gold coated with 2.5nm $SiO_2$ (circles) and surface plasmon decay lengths (squares) [40]

In 2006, Zhang and Somekh analyzed the relation systematically and proposed a theoretical framework for it[78]. Here, I define the lateral resolution as the transition distance (Edge response) along x-axis between the on and off of the grating, and sensitivity as the response difference between the on and off of the grating. In Fig. 2-25 it is clearly shown that (b) has sharper edge response than (a), which means (b) has better lateral resolution. Then I check the sensitivities of the two cases. According to the definition, it is obvious that (a) has higher sensitivity than (b). The conclusion is that higher sensitivity refers to poorer lateral resolution. This is therefore a trade-off between the two properties. Thus, how to overcome or at least optimize the trade-off by obtaining high sensitivity and relatively comparable lateral resolution with conventional optical microscopy is a big topic in the field of SPRM.

41

(a)                                          (b)
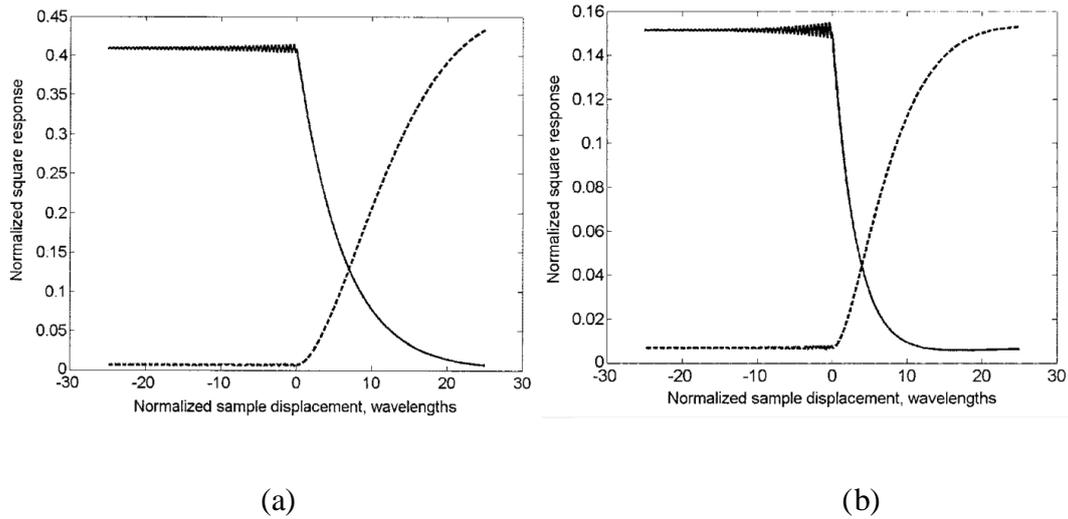
Fig. 2-25 Surface wave response across an interface on and off resonance (a) 'weak' coupling; (b) strong coupling

[78]

## 2.3.4 Interferometric SPRM

Although many researchers are struggling in overcoming the trade-off, in the field of intensity based SPRM, rare successful reports could be found. In 2000, Somekh built a two-arms heterodyne interferometric SPRM and achieved a submicron lateral resolution with satisfying sensitivity [4, 5]. The experimental setup is shown in Fig. 2-26. In this system, a ZEISS 100X 1.25 NA oil-immersion objective was used to excite SPR and a reflected mirror was used for the reference beam. Two Bragg cells were used to shift the frequencies of two interference signals. Images with different defocus were obtained.
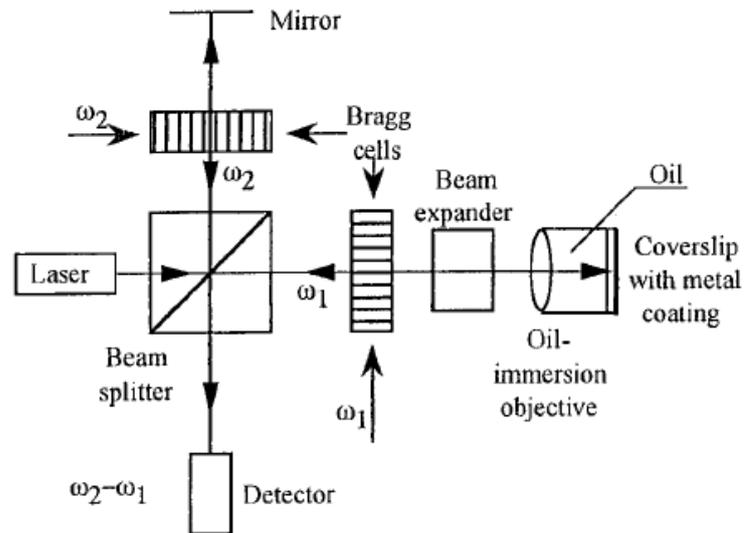
Fig. 2-26 schematic diagram of the scanning heterodyne interferometer [4, 5]

It was the first time to limit the lateral resolution of SPRM to the diffraction limitation. The so-called *V(z)* technique was exploited.

### *Introduction to V(z)*

*V(z)* which refers to the voltage generated with defocus z, was originally proposed in acoustic scanning microscopy[79, 80]. Later, the technique of *V(z)* was introduced to confocal microscopy to assess the lens aberration[81]. In 2000, Somekh introduced the *V(z)* technique into the field of SPRM[4, 5]. By detecting the interference between the reference and the SPR signal along the axial z direction, a *V(z)* curve could be generated. In order to calculate the *V(z)* response theoretically, I need to evaluate the electric field on the back focal plane. Fig. 2-27 shows the schematic diagram of the back focal plane.
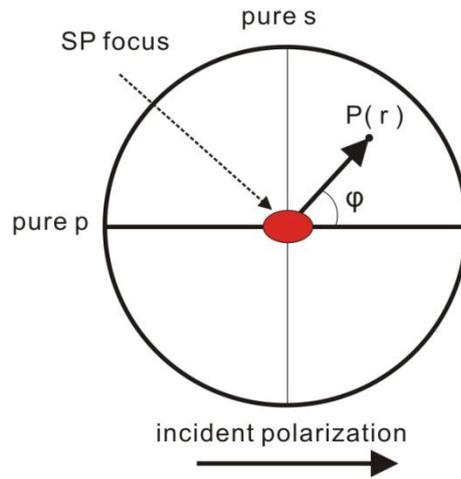
Fig. 2-27 schematic diagram of the back focal plane

Assuming a linear polarization plane wave indicent on the back focal plane, the electric field varies with the pupil function, which is a function of the radius r. The maximum angle of the incident can be calculated from the clear aperture of the objective,

$$\theta_{max} = a\sin(\frac{NA}{n_{oil}})$$
Eq. 2-27

If I take the aperture of the objective to be the unity, according to the Abbe sine condition, the relation between the radius and the incident angle can be expressed as:

$$\sin\theta = r \times \sin\theta_{max}$$
Eq. 2-28

From Fig. 2-27, every point on the back focal plane can be fixed by r and $\phi$. I assume the pupil function is P(r). By using the upper equation, the pupil function can be expressed as $P(\sin\theta)$. Now, the electric field on the back focal plane can be calculated:

$$E_{reflected} = P^2(\sin\theta)(R_p(\sin\theta)\cos^2\phi + R_s(\sin\theta)\sin^2\phi)\exp(j2nk\cos\theta z)$$
Eq. 2-29

Where, $R_p$ and $R_s$ refer to the reflected coefficients for the p and s polarization component; k refers to the k-vector (wave number) in the free space; n is the coupling oil refractive index

and also that of the coverglass substrate. z refers to the distance from the focal plane and the positive and negative means the movement direction away or towards the objective lens. Pupil function is squared as the system is a reflected one and the signal passing through the objective lens twice. Similar to other interferometric system, a reference is required. In the two arms heterodyne interferometer, a mirror is used to generate the reference $E_0$. Now the interference between the SP signal and the reference can be expressed as:

$$(\vec{E}_{reflected} + \vec{E}_0)^2 = \left|E_{reflected}\right|^2 + \left|E_0\right|^2 + 2E_{reflected}E_0 = DC + 2E_{reflected}E_0 \qquad \text{Eq. 2-30}$$

As the system is heterodyne, only the AC signal can be detected. For simplicity, I take the uniform reference $E_0$ as a unit, then I integrate the whole back focal plane and the output of $V(z)$ can be calculated as:

$$V(z) = \iint\limits_{Aperture} P^2(\sin\theta)(R_p(\sin\theta)\cos^2\phi + R_s(\sin\theta)\sin^2\phi)\exp(j2nk\cos\theta z)d(\sin\theta)d\phi \quad \text{Eq. 2-31}$$

In the whole project, only the amplitude of $V(z)$ is detected, and the phase is omitted.

### *Contrast mechanism of the interferometric SPRM*

Experimental $V(z)$ curves were shown to explain the contrast mechnism (Fig. 2-28). A grating composed from 20nm thickness of $SiO_2$ (n=1.5426) coated and bare gold was applied. When the plasmon condition changes (like dielectric is coated), the period of $V(z)$ will be different. Dielectric material coated part has longer period. Thus, by scanning 'on' and 'off' of the grating, different period of $V(z)$ will be generated. For example, at the position A, as different field is detected, the grating can be distinguished. This is the contrast mechanism in the $V(z)$ technique. Furthermore, by using different defocus, the contrast can be inverted when using -

1.5μm and -1.8um ('A' and 'B' in Fig. 2-28). The experimental images are shown in Fig. 2-29.
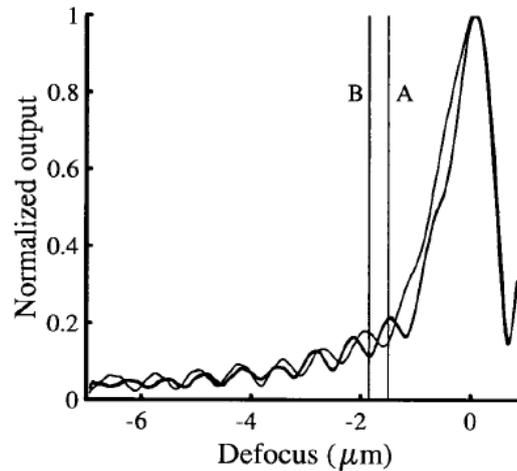


Fig. 2-28 *V(z)* curves by scanning the coated sample and uncoated sample, thin and thick line refers to the on and off part of the grating sample, thin line refers to the coated section and thick line is that of the uncoated section [4, 5]. Here the minus defocus means the distance between the sample and the objective lens is shorter than the focal length of the lens.

This system is a milestone in the history of SPRM, as it is the first interferometric SPRM was demonstrated and the so-called trade-off between the sensitivity and lateral resolution was optimized. The lateral resolution was improved to the submicron, wavelength range, rather the conventional several micrometres. It was the first time that the lateral resolution of a SPRM was comparable with the conventional optical microscopy. In 2007, Berguiga extended the lateral resolution of a little smaller than 1μm in air and 200nm in water[8]. In 2009, Stabler and Somekh expanded the scanning heterodyne interferemeter into a wide-field system [9]. In 2011, Berguiga applied the scanning heterodyne application to cell imaging.
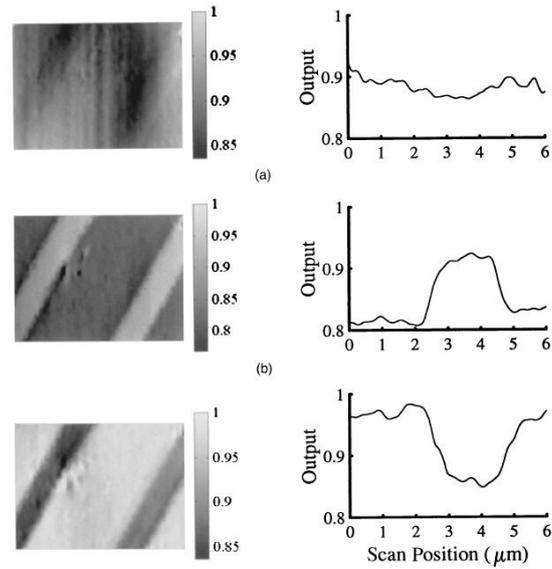
Fig. 2-29 Scanning images from the scanning heterodyne interferometric SPRM with different defocus. (a) z=0;(b) z=-1.5μm;(c) z=-1.8μm [4, 5]

It can be seen that the scanning heterodyne SPRM and wide-field SPRM 1) optimized the trade-off between the sensitivity and lateral resolution suffered by the conventional non-interferometric system, and 2) provides a satisfactory lateral resolution comparable with conventional optical microscopy without reducing the contrast. However, I can also find that both of them exploit a two-arm interferometric system setup. It is well known that the interferometer suffers from the complicated system setup and the problem of relatively high sensitivity to the environmental vibration. So I ask myself if there are other setup which can avoid the problems of interferometer but also provide a similar lateral resolution and acceptable sensitivity. In this project, I devise a confocal setup to replace the heterodyne interferometer. The new confocal SPRM can avoid the complexity of the two arm heterodyne interferometer but provides comparable lateral resolution as well as allowing greater flexibility.

## 2.3.5 Confocal SPRM

By analyzing the interferometer and confocal technique, I find they share the same transfer function. Furthermore, the confocal method can provide a similar $V(z)$ effect to the scanning heterodyne interferometer. Since I need to use the confocal technique in the project and build a confocal optical setup, a brief review on the confocal technique is provided.

### *Introduction to confocal microscopy*

The confocal technique was invented by Marvin Minsky [82] in 1955 and firstly was used to limit the resolution out of the focal plane. Although in this thesis, I are only looking at two dimensional objects, I are still using the confocal configuration for a similar purpose that is to examine light that appears to come from the same plane. This point will become clear in the following of the section. Confocal microscopy can get sharper images of a specimen than conventional microscopy by blocking the light which is not in the focal plane and is the reason of blurred edge of the image [82, 83]. Although the technique was invented in the 1950s, its popularity increased towards the end of 1980s. Since then, it has been widely used in life sciences and materials science. It is worth mentioning that there are more and more confocal microscope designs coming up and they all use the key elements of the original setup: the two apertures and the point-to-point acquiring. Basically, there are two kinds of setup. The first one is the sample scanning type, which was adopted by Marvin Minsky in the first confocal microscope[82]. A typical optical setup of this type is shown in Fig. 2-30 (From Nikon).
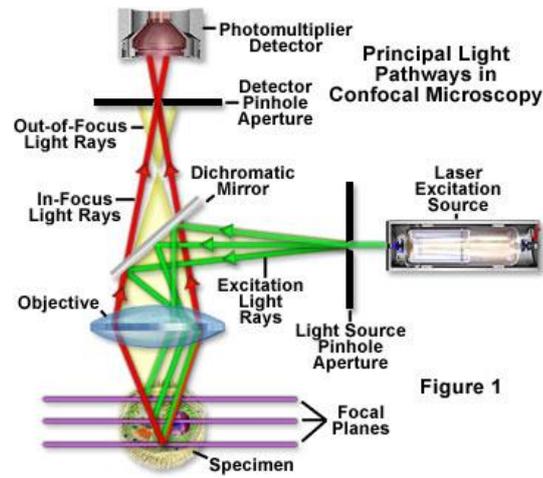
Fig. 2-30 the  mechanics of confocal microscopy from Nikon Microscopy

Another type is the optical beam scanning and a typical mechanics is as Fig. 2-31.
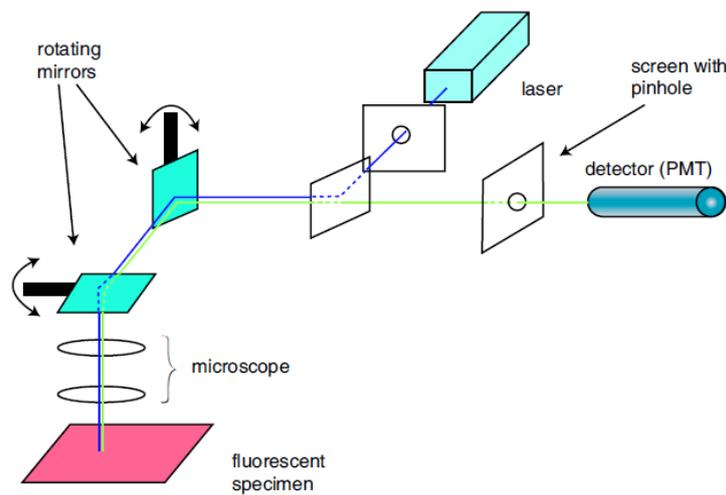


Fig. 2-31 Basic setup of a beam scanning microscope[84]

The first setup is easier to build. The latter one benefits from faster scanning, but it is more complicated and is less suitable for a demonstration experiment. As this project aims to demonstrate the idea of interferometric confocal SPRM, I build up a simple optical system based on the first setup, that is the sample scanning type.

## *How a confocal microscope works*

A simple configuration of the confocal laser scanning microscope is shown in Fig. 2-32. The actual alignment in the project is similar but not identical to the schematic diagram. The same objective lens is used as both the collector lens and objective lens which collect the signal information reflected from the sample.
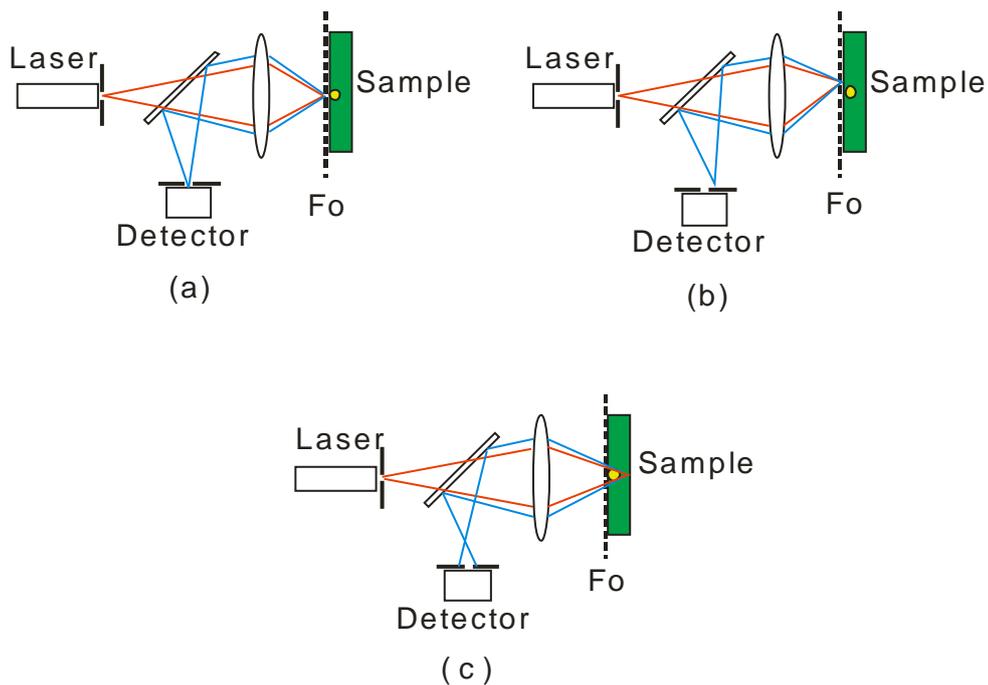


Fig. 2-32 Schematic of confocal laser scanning microscope, (a) focal plane; (b) off-axis; (c) defocus

In Fig. 2-32 (a), a point of sample on the focal plane is detected by the detector, while a point out of the sample is blocked by the detector even if it is located on the focal plane in Fig. 2-32 (b). In Fig. 2-32 (c), defocused light coming from the object axis is still blocked because the returning light is out of focus of pinhole. In this thesis I use the properties of confocal microscopy to select certain paths of the surface plasmon. It is easy to draw the conclusion that both the lateral resolution and axial resolution are increased. Although confocal technique is adopted in the project, it does not mean that I will use the exactly same configuration as general confocal microscopy. Actually, some simplification is provided.

More details on how to build up the confocal experimental system can be found in chapter 3 and details on how to apply $V(z)$ in the confocal surface plasmon microscope will be developed in chapter 4.

## 2.4 Summary

In this chapter, I firstly introduced the physics of SPs and properties of SPR, and then based on the fundamental knowledge, SPR sensing was described. Finally, a review of surface plasmon microscopy was presented. According to the limitations of the conventional intensity based SPRM, I introduced the two-arm interferometric SPRM. Aiming at simplifying the complexity of the system, I proposed the confocal SPRM technique. A brief introduction to the confocal technique was given and the working of a confocal microscope was described. More information will be in the following chapters.

# 3 Instrumentation

## 3.1 Introduction

This chapter will introduce the development of the confocal surface plasmon resonance microscope. Initially, I built a confocal SPR microscopic system with amplitude modulation for the illumination beam by using an amplitude spatial light modulator (A-SLM). The experiment in chapter 4: confocal SPRM and pupil function engineering experiment is based on this system. Later, in order to modulate the phase profile of the illumination beam, I replaced the amplitude SLM with a phase SLM. The experiment in chapter 5 ($V(\alpha)$) and chapter 6 (Phase-stepping) are based on the new system. There is no big difference in the optical system except for the SLM part. I will introduce the first system in detail and just briefly describe the modifications of the second system.

Before developing the system, I need to consider what kinds of functions I need to fulfil in the project. By analyzing the project, the functions list is shown: 1) A simplified confocal SPR system setup; 2) 3D sample scanning; 3)Beam profile modulation; 4) Relatively high magnification (>1000) in imaging system. According to these functions, I designed the instrumentation structure which is composed of four parts: optics, mechanical sample scanning, A-SLM control, and data acquisition & processing part, as shown in Fig. 3-1.
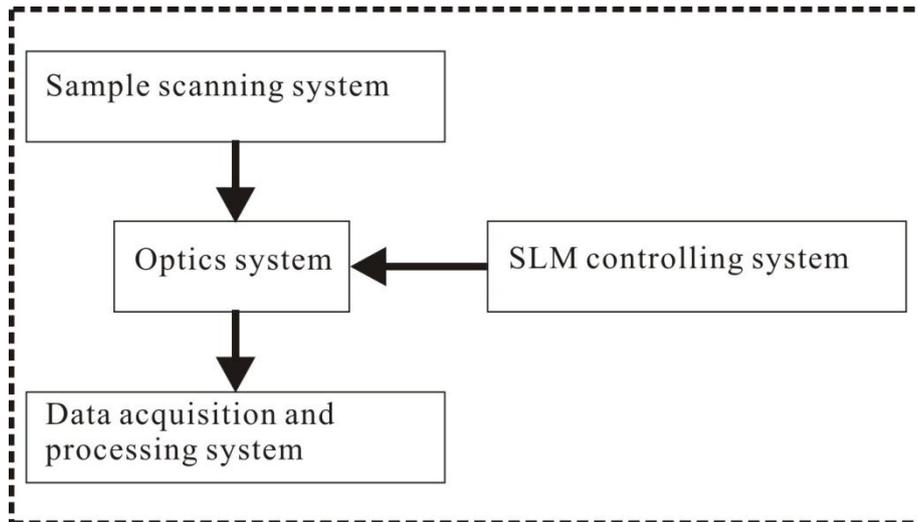
Fig. 3-1 schematic diagram of the system

A reflected amplitude sensitive spatial light modulator (A-SLM) is used to modulate beam profile of the illumination amplitude. A two-stage magnification is designed to magnify the focal point. All the controlling software, which mainly includes the sample scanning motion control, A-SLM control and camera control, is developed on the LABVIEW platform. Data acquisition and processing programs are based on MATLAB. Details will be described respectively in the subsequent sections.

## 3.2 Optical system

### 3.2.1 General design of the optics

Fig. 3-2 shows a schematic diagram of the optical system which consists of two parts: illumination part (in red rectangle) and imaging part (in blue rectangle). Since this is a reflection system, light passes through the objective twice and takes the roles of both condenser and collector. The SLM optics is enclosed in the green rectangle. A 632.8nm He-Ne laser (10mW) was used as the illumination source. Beam expanders were designed to increase the beam diameter of the beam incident onto the spatial light modulator (SLM) which was conjugate with the back focal plane (BFP) of the immersion objective. The SLM

could control the effective illumination pattern in the BFP. Illumination and imaging paths were separated by a pellicle beam splitter. A 1.25 NA oil immersion objective which had sufficient aperture to excite SPs in air was employed in the experiment in chapter 4. The light distribution reflected from the sample was imaged onto the CCD camera which served as a variable pinhole. The light from the sample was magnified by approximately 1000 times from the sample to the CCD plane so that a point spread function occupied >100 pixels, this allowed the pinhole radius to be readily controlled by selecting different regions of camera, moreover, spreading the returning beam reduced the problem of saturating individual pixels. More details will be shown below.
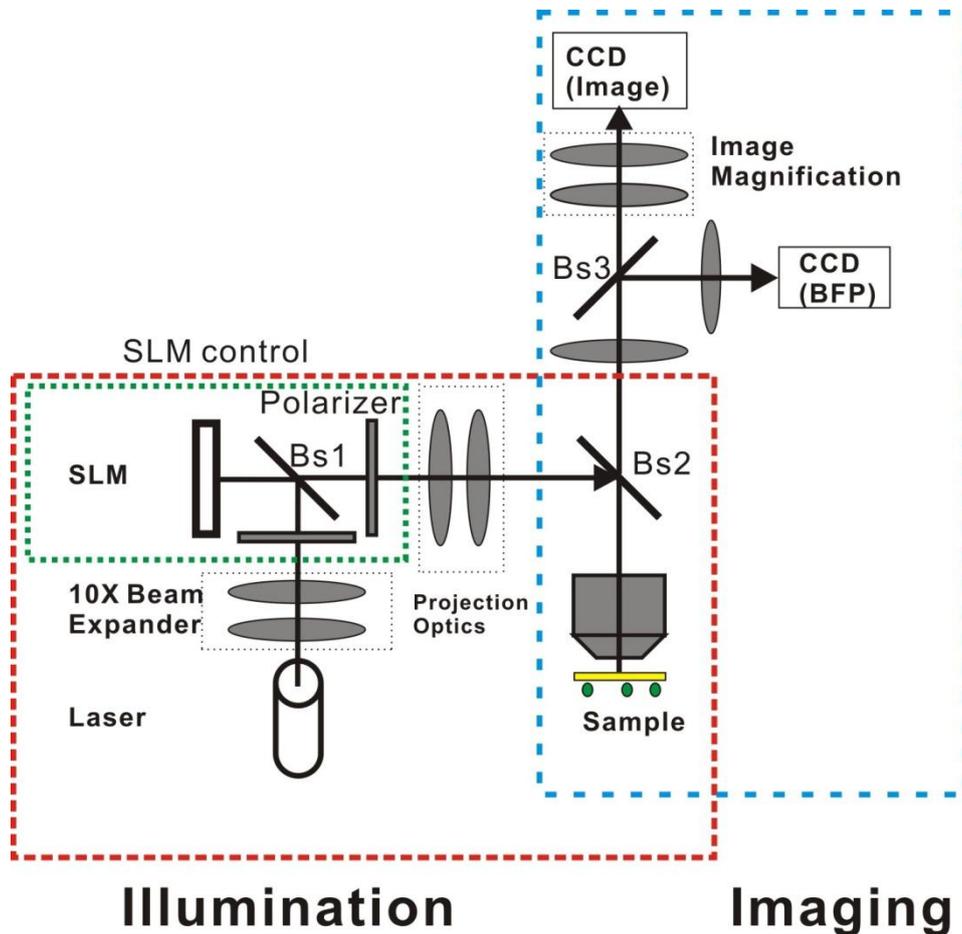
Fig. 3-2 Schematic diagram of the experiment setup

During the development of the system, I noticed several issues which need to be considered:

## 1) *SLM v.s. mirror*

In the earliest version of the system, there was no amplitude SLM and a pure mirror was used. A simple expander was built to expand the laser beam to fill in the aperture of the objective. (ZEISS N.A. 1.25). Different expander values were tried, 8, 10 to even 80, to reduce the influence of the illumination shape to the *V(z)* curves. Results have shown that the illumination pattern at the edge of the lens aperture can be a major problem in generating *V(z)* curves. By analyzing the reasons, I proposed the method of pupil function engineering and employed an amplitude SLM to modulate the beam profile and reduced this effect. More simulations and experiment results will be in Chapter 4.

## 2) *Pellicle BS v.s. cube BS*

At the very beginning, I used cube beam splitters rather than pellicle ones. Then I found that i) the reflection from 2nd surface of the cube BS was so strong that it was rather difficult to align the imaging section; ii) the defocused signal of high NA oil-immersion objective lens was relatively weak and was almost covered by the background noise owing to the 2nd surface reflection of BS. For these two reasons, pellicle beam splitters replaced the cube ones.

## 3) *Bragg Cell*

The function of the Bragg Cell in the system was not same as used in the heterodyne interferometer described in chapter 2. According to the requirements of the reflected SLM from ForthDD Ltd, the illumination should be modulated by the pulses from the driver board of the SLM. Generally, LEDs, which can be switched on and off at high frequencies, are used as the illumination of the SLM. However, in the system, a He-Ne laser was used and the fast switching was performed by modulating the 1st order of Bragg Cell ( located in front of the He-Ne laser) on and off. More details will be introduced in the following section of the SLM controlling section.

## 4) *High magnification*

A two-stage-magnification is developed. Because of the relatively high magnification requirement, a 10X/0.20NA infinite objective lens is used for the second stage magnifier. A total magnification ratio of 1470 was obtained.

## 3.2.2 Illumination part
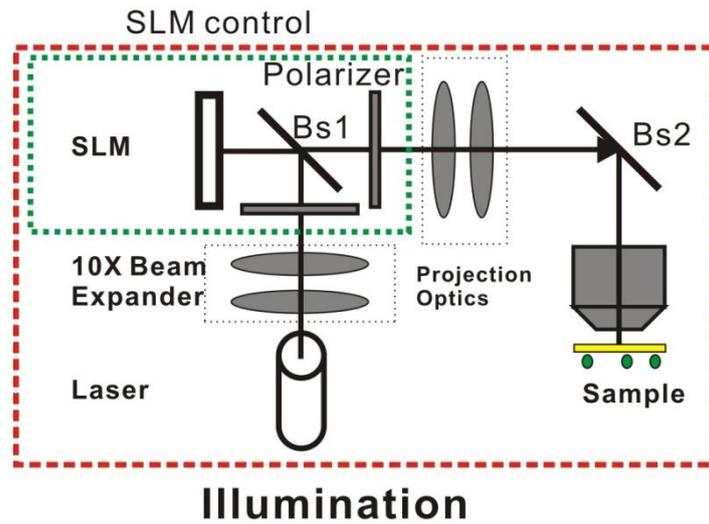


Fig. 3-3 Schematic diagram of the illumination part

The schematic diagram of the illumination part is shown in Fig. 3-3, which is part of Fig. 3-2. Six parts are included: the illumination source laser, beam expander, SLM projection, two polarized beam splitter (BS1 and BS2), and objective lens.

### *Laser coherent illumination source*

In selecting the illumination source, I need to consider whether the plasmonic resonance angle at the wavelength is in the range of NA of the objective lens? I have 1.25NA and 1.45NA objective lenses in the lab, which provide biggest angle of (55.3 deg and 72.5 deg) respectively. For all the experiments in this thesis, I excite SPR in air. Fig. 3-4 shows the relation between the resonance angle $\theta_p$ and wavelength. If I use He-Ne laser (wavelength is 632.8nm), the resonance angle in air is 43.47 deg as the mark shown on the blue curve of Fig. 3-4. Even if coated dielectric, like 20nm BSA (Bovine serum albumin, n=1.43), the

resonance angle is about 46 deg as the mark shown on the red curve of Fig. 3-4. Considering I modulate the pupil, this is sufficient. Another big advantage of using a He-Ne laser is that it is inexpensive and can be easily found in any optics group. Considering all the conditions, a He-Ne laser with a total output of 10 mW is applied. It is coherent and is suitable for interference. Since I are using a scanning system, it is necessary to avoid saturation of the focal spot projected onto the CCD so a high neutral density filter is required.
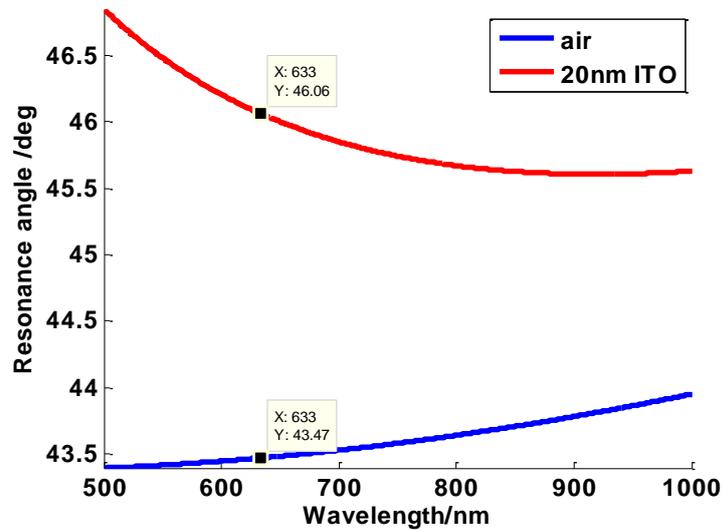


Fig. 3-4 Plasmonic resonance angle v.s. wavelength of illumination source

### *Objective lens*

An oil immersion objective lens is used to excite SPR in the system: ZEISS 100x/1.25, ∞/0; The tube length of the objective is 165mm, and thus the focal length is $f = 165/100 = 1.65$mm. The diameter of the BFP (clear aperture of the objective lens) is $D = 2f \times NA = 4.125mm$. In this system, a focused laser beam by a high NA objective and a sandwich structure sample (Fig. 3-5) are used to excite SPR.
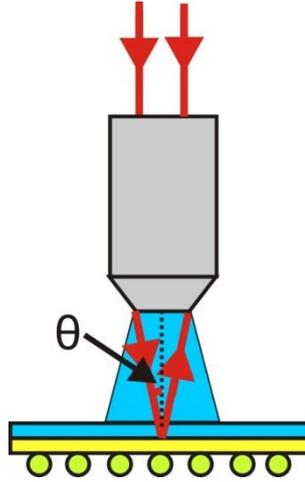
Fig. 3-5 Excitation of SPR by using a high NA oil-immersion objective

θ is the incident angle at which SPR can be excited. Its value can be calculated from the momentum matching condition, as follows:

$$k'_{photon} = k_{sp} = k_{photon} \times \sin(\theta) = \frac{2\pi n}{\lambda} \times \sin(\theta) = \frac{2\pi NA}{\lambda} \qquad \text{Eq. 3-1}$$

Where, $k'_{photon}$ is the parallel component of the photon wave vector, while $k_{sp}$ is the surface plasmon wave vector[12]. $k_{sp}$ depends on the optical thickness of the metal coating[85]. The propagation constant of the SPR on the metal surface facing the air medium is approximately given by [32, 36].

*Beam expander*

In order to fill in the clear aperture of the objective lens (4.125mm), considering the diameter of the He-Ne laser (0.68mm), a beam expander should be added. I used two doublet lenses to expand the beam (Fig. 3-6). It is obvious that an at least 6X (4.125/0.68) expander is required. Then considering the Gauss function shape of the laser profile, a 10X can produce a flatter beam profile in the clear aperture. In this system, I adopted 10X therefore the beam diameter after the expander will be 6.8 as shown in Fig. 3-6.
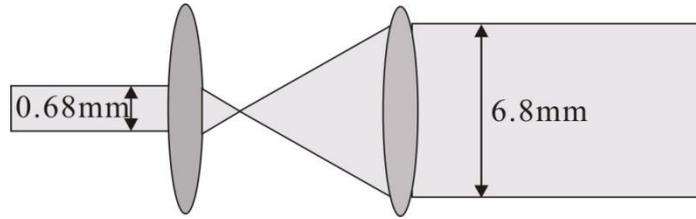
Fig. 3-6 Schematic diagram of the 10X beam expander

*SLM projection optics*

I designed 1X projection optics. The reason of the projection optics is that the SLM can be located at the conjugate plane of the BFP of the objective. Therefore, the modulation patterns on the SLM can be projected on the back focal plane of the objective lens using a 4-f system (Fig. 3-7). Considering the diffraction of the pixels on the SLM, a pinhole (red structure in Fig. 3-7) is used as the spatial filter to remove the diffractive orders and to ensure only the zero-order beam passes.
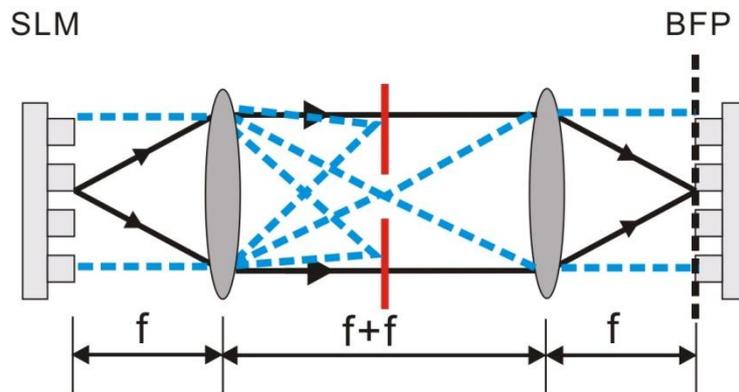


Fig. 3-7 4-f projection structure of the SLM

## 3.2.3 Imaging part

In this section, I demonstrate the imaging section of the optics (Fig. 3-8). It includes three parts: objective lens (same one with the illumination part), focal point magnification part, two cameras (one for the focal point imaging, the other is for the back focal plane imaging). Each part will be introduced respectively.
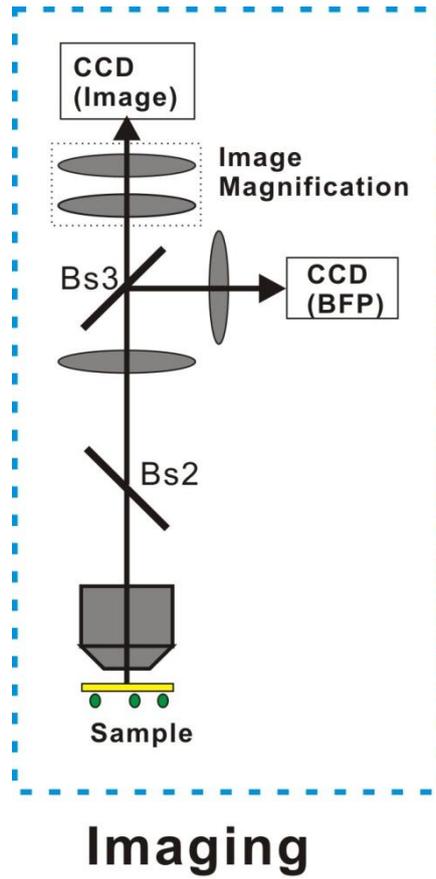
Fig. 3-8 Schematic diagram of the imaging section

*Focal point imaging system*

As this system is a reflected one, the oil immersion objective lens (ZEISS 100x/1.25, ∞/0) is passed through twice, once for the illumination (Section 3.2.2), and once for the imaging (this section). The tube length of ZEISS objective lens is 165mm, and thus the focal length is:

$$f = \frac{165}{100} = 1.65 mm \qquad \text{Eq. 3-2}$$

The Airy disc diameter of the point spread function by using the 1.25NA objective lens can be calculated as:

$$d = \frac{\lambda}{NA} = 0.506 \mu m \qquad \text{Eq. 3-3}$$

As I use the CCD as a virtual pinhole, a much more large magnification is required than the Shannon sampling theorem dictates: the sampling frequency should be higher than twice of the retrieved signal. Considering the magnified Airy disc takes around 100-150 pixels on the CCD which has $640 \times 480$ pixels with a pixel size of 7.4 microns, the diameter of the magnified Airy disc will be $7.4 \times 100$-$7.4 \times 150$, which is 740-1110 microns, therefore, the magnification ratio will be $(740 \sim 1110) / d = 1463 \sim 2194$. A further 10X magnification was provided using an objective and second tube lens. This is more compact than using two doublets. Another advantage of making the system compact is that it improves the sensitivity to vibration noise. A 10X/0.2 NA infinite conjugate objective by ZEISS and a 200 mm lens are added to the system as the $2^{nd}$ stage magnification. M2=200/16.5=12. Therefore, a total magnification of 1467 is obtained and the actual Airy disc will take 100 pixels. The focal point image on the CCD will be $0.618 \times 1467 = 906.6 \mu m \approx 1mm$. The whole diagram is shown in Fig. 3-9.
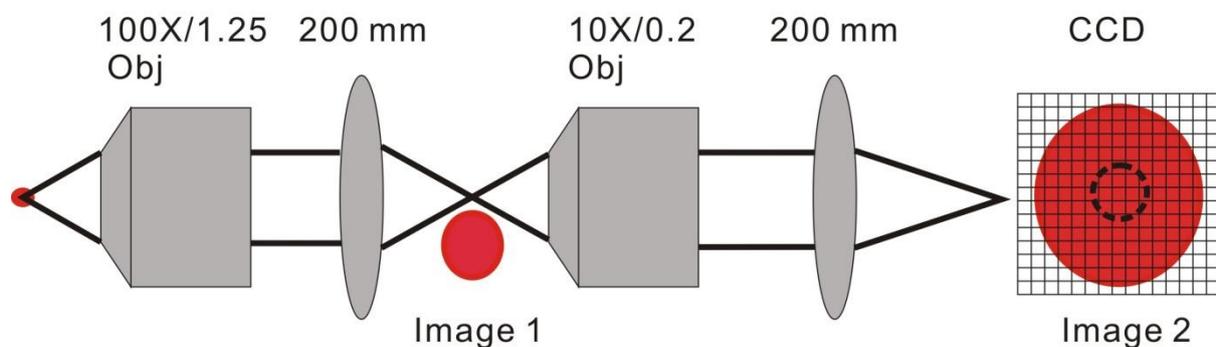


Fig. 3-9 Schematic diagram of the focal point magnification system

## CCD: virtual pinhole

Two Sony XCD-V60 CCD cameras are applied for the detection of the focal point images and back focal plane images. The focal point is imaged by a monochrome CCD camera with cell size of $7.4 \times 7.4$ um and image size of $640 \times 480$. Its digital interface is IEEE 1394b-2002 and an image acquisition program was developed by LABVIEW. Details of the program are

in appendix. Virtual pinhole is applied by splitting the CCD pixels as the schematic diagram shown in Fig. 3-9. By using the magnification parameters above, the focal point image on the CCD is about 1 mm, which takes about $100 \times 100$ pixels. If I define the pinhole size to be 0.1 of the Airy disc, then the pixels in the pinhole will be about $10 \times 10$ pixels. Then I add the response of these pixels, the summation will be the intensity of the confocal system. By square rooting the intensity, I can calculate the field response. It can be expressed as:

$$\left| \vec{V} \right| = \sqrt{I} = \sqrt{\sum_{pinhole} i_{pi}} \qquad \text{Eq. 3-4}$$

## 3.3 Sample scanning system

According to the confocal microscope configuration mentioned in chapter 2, generally, there are two kinds of setups, one is sample scanning and another one is optical scanning. Optical scanning is quicker and thus generally used in confocal microscopy. While for the sample scanning system, although it is a little time-consuming, it is much easier to build and is usually used in testing new ideas. In this experiment, a sample scanning system was built. A sample scanning system, which was the heart of the system, was designed. According to the experiment conditions and the existing experimental equipment, a 3D mechanical stage was used for coarse adjustment of the sample. 2D (PI P541.2CD) and 1D piezoelectric transducer stages (PI P621.1CD) are used for fine adjustment separately. A holder and several adapters, which were homemade in the workshop of Faculty of Engineering, were designed. The schematic diagram of the system is shown in Fig. 3-10.
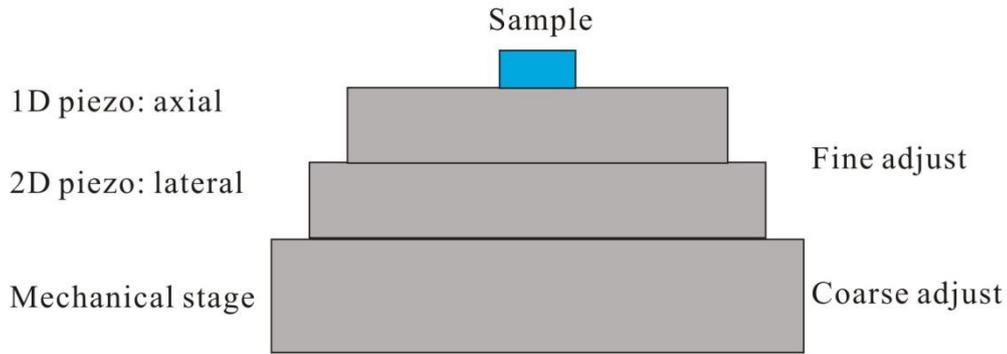
Fig. 3-10 Schematic diagram of the sample scanning system

The sample was mounted on the sample scanning system. The mechanical stage can be used to identify the observed specimen with its long moving distance but low moving resolution. While two PZT stages (1D for the axial direction and 2D for the lateral directions.) are used for the precise positioning and scanning, with its short moving distance (<100um) and accurate resolution (0.001um). Controlling software based on the LABVIEW platform is developed. Details of the software flowchart can be found in next section and the front panel and back block diagram designs will be in the appendixes.

## 3.4 Amplitude SLM system and control

### 3.4.1  Reason for modulating back focal plane

In the two-arm heterodyne system, no modulation was applied in the back focal plane image although the noise ripples owing to the sharp edge of pupil function were present. Actually, at the very beginning of the confocal experiment, there was no pupil function modulation and I just put the full profile of laser illumination to the aperture of the objective lens. According to my expectation, for a sandwiched sample (1.52 cover glass, 50nm gold, air), the ripple period of SPR interference should be about 0.74μm.  However, the experimental *V(z)* showed a considerable amount of spurious signals. It is obvious that some other ripples frequencies were added to the expected SPR ripples. To confirm my assumption, I used a conventional

63

mirror (non-plasmonic sample) as the sample and scanned its *V(z)* curves. I assumed that if there are no noisy ripples, there should be no ripples on the *V(z)* curves. The experimental curves show that even if I just scan the mirror, another kind of ripples appears. If I used the NA 1.25 objective lens, the noisy ripple period is about 0.54 microns. By analyzing the theory, I found that the noisy ripples come from the effect of sharp edge pupil function. If I did not take any measures here and scanned *V(z)* of plasmonic case (1.52 cover glass, 50nm gold, air) directly, the *V(z)* curves actually is the addition of the SPR ripples and the sharp edge confocal effect ripples. In order to solve this problem, I proposed the pupil function engineering here and exploited amplitude SLM to modulate the pupil function. More details, including the simulation results and experimental results, will be demonstrated in chapter 4. Here, I will just introduce the system built-up.

### 3.4.2 Mask generation

Generally speaking, three methods are usually used to realize the pattern shapes in the BFP. Let take the 'ring' shape as an example. The principles of the three methods are shown in Fig. 3-11.
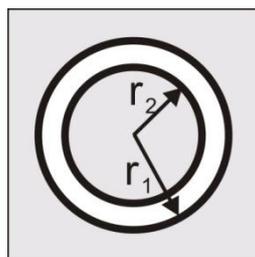


(a)
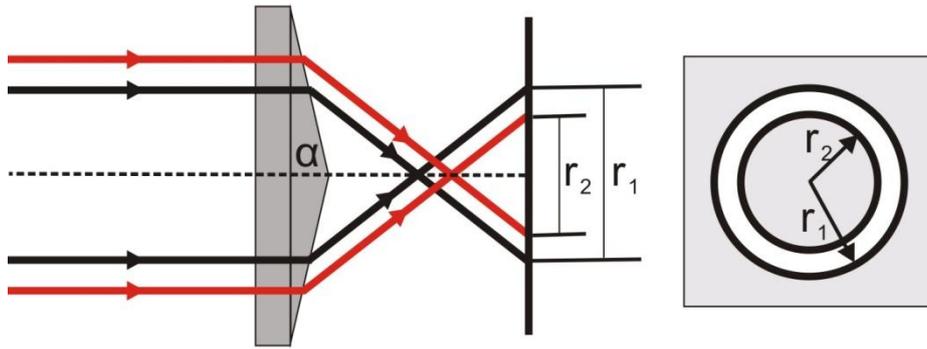
(b)
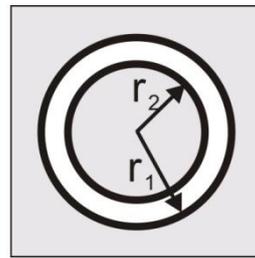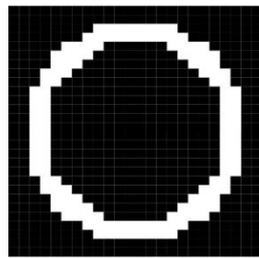


(c)

Fig. 3-11 Pattern generation methods, (a) is the physical mask; (b) is mask generation by Axicon prism lens; (c) is by using a reflected SLM

In order to compare the three methods clearly, Table 3-1 lists all of their advantages and disadvantages. By comparing the advantages and disadvantages and considering this system, I adopted the SLM for the following reasons. Firstly, in the scanning system, illumination power is not a vital factor, so the drawback of the former two methods can be eliminated. For the Axicon lens method, optical quality is poor as the phase profile gets randomized due to surface imperfections, which destroys effects relying on spatial optical coherence. That is the main reason that this method is not adopted in the system. As the physical mask, firstly, it is difficult to manufacture; secondly, when it is produced, the size and shape of the pattern cannot be varied; the last but the most important reason is that it cannot generate greyscale. Since the system is confocal, any axial intensity response or aberration can influence the results. If no greyscale is used and the edges of the pattern are sharp, errors of high frequency

ripples, which will affect the SPR *V(z)* response, may be introduced. Considering all these factors, SLM is adopted to generate the patterns of the BFP.

Table 3-1 comparisons of physical mask, Axicon prism lens and SLM

|  | Physical mask | Axicon prism lens | SLM |
|---|---|---|---|
| Cost | low | medium | high |
| Energy loss | high | low | high |
| Convenient to change pattern | Cannot change | Can change a bit | Easy to change |
| Phase disorder | no | yes | no |
| Automatic control | no | no | yes |
| Greyscale pattern | no | no | yes |

### 3.4.3  Spatial light modulation

A spatial light modulator is a device which can be used to modulate the beam profile. According to the amplitude or phase it can modulate, there are two kinds of SLM: amplitude SLM and phase SLM. Both of SLM is controlled by electrons pixel by pixel. In this part, I just describe the amplitude SLM. Controlling of the phase SLM will be described later in chapter 5. I ordered amplitude SLM from ForthDD Ltd. The SXGA miniature colour Liquid Crystal Display (LCD) displays full colour computer or video graphics images with a spatial resolution of 1280 × 1024 pixels on 20.68mm × 18.87mm reflection mode silicon die (active area 17.43mm × 13.95mm) micro-display. After calculation, the pixel size is around 13.62um

*SLM modulation principle*

According to the principles of the reflected SLM, an alignment as Fig. 3-12 was designed. Illumination beam vertical polarized wave was reflected to the surface of the A-SLM by a polarizing beam splitter and then the input vertical polarized wave (red line in figure) is modulated by the SLM. Every pixel has two states: on and off. The states are automatically controlled. If the state is 'on', the input vertical polarized wave is modulated to be horizontal polarized wave.  As the modulation efficiency is not 100%, there is still an amount of directly reflected vertical polarized wave from the surface of the SLM, so both vertical and horizontal

polarized wave exist (blue line). As the beamsplitter is polarized, ideally the directly reflected vertical polarized wave is blocked and only p wave can pass through the BS (green line). If the state is 'off', then the vertical polarized is not modulated and will be reflected directly. Considering the polarized BS, ideally the vertical polarized is blocked. In practice, I still need a polarization analyzer to reduce the leaking vertical polarization furthermore.
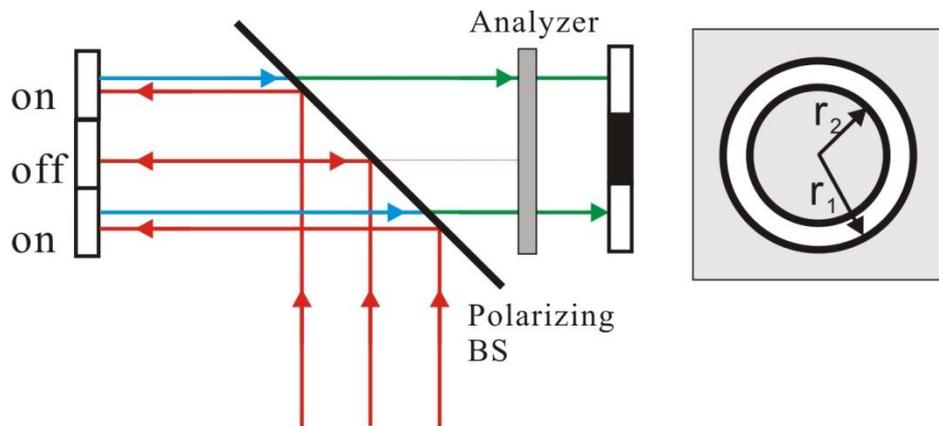


Fig. 3-12 Optical alignment schematic diagram of the amplitude SLM

## *Principle of Greyscale pattern generation*

Since the confocal technique is still based on the interferometer, I need to consider how to interfere between pixels. I proposed a method of picking up pixels randomly to generate greyscale patterns, as shown in Fig. 3-13. If there are 16 pixels, I turn on two of them and can get the grey level of 0.2. If I turn on 8 pixels, I can get 0.5.
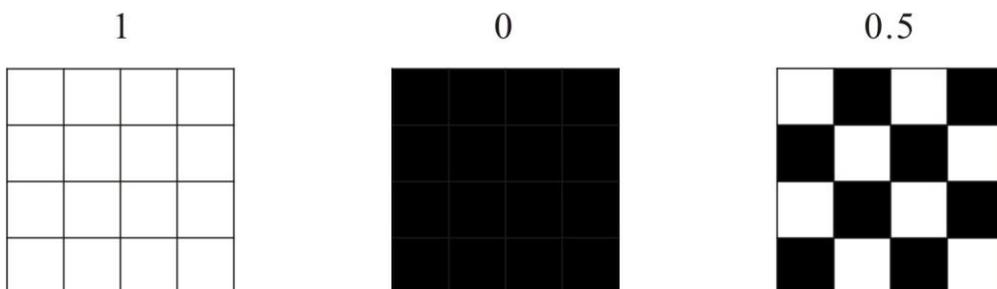


Fig. 3-13 greyscale patterns generation in this project

# 3.5 Automatic and motion control system

## 3.5.1 General structure

The automatic and motion control system is developed on the platform of LABVIEW. It includes three parts, sample precise positioning and scanning, SLM operation and camera acquisition part. I used the Top-Down software development approach, which makes the software development much more flexible. First of all, I will show the general structure. Then details of each section will be demonstrated. As different experiments in this thesis used different control software, here, I will just illustrate an example flow chart of the whole project. Specific procedures will be expressed in each chapter.
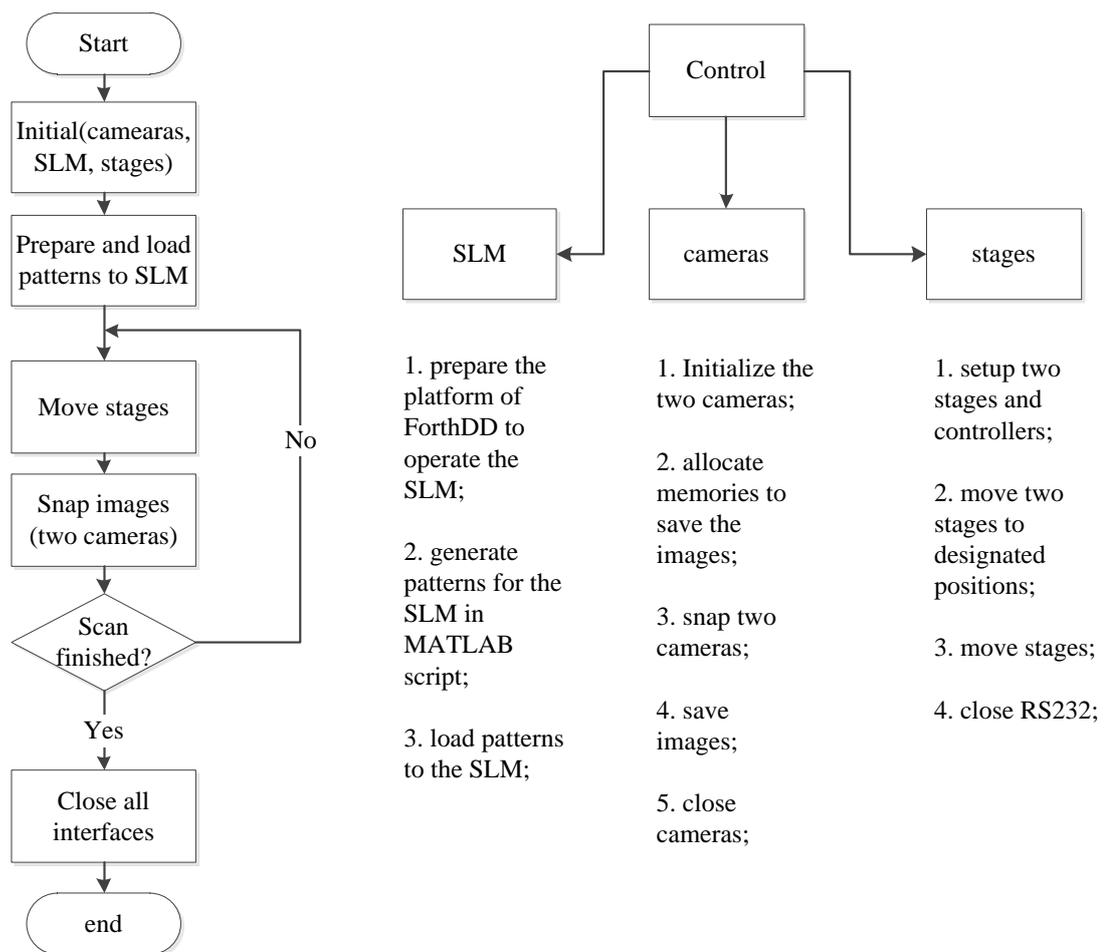
Fig. 3-14 Flowchart of the controlling software

## 3.5.2 PI stages control

### *Positioning precision*

I adopted two stages, P621.1CD for the z-scanning and P541.2CD for the x-y scanning. They are all capacitive piezo precision stages from Physik Instrumente Ltd. Table 3-2 shows the specifications of the two stages. The scan ranges of the stages are all 100 microns, which are definitely sufficient for the project. The closed-loop resolution was 0.3 nm in z direction and 0.8 nm in x-y directions.

Table 3-2 specifications

| Model | P621.1CD | P541.2CD |
|---|---|---|
| Axis | z | x-y |
| Scan range (μm) | 100 | $100 \times 100$ |
| Closed-loop resolution(nm) | 0.3 | 0.8 |

### *Hardware connection*

Two digital controllers were applied to position and move the stages, PI E-517 for the 1D stage and E710 for the 2D stage. The interface between the stage and digital controller is the Sub-D special connector. The interfaces between digital controller and PC are RS232 common interfaces, as shown in Fig. 3-15.
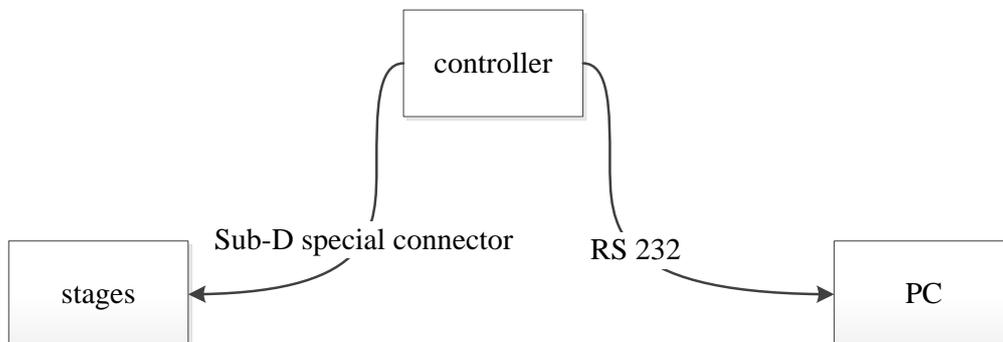


Fig. 3-15 hardware connections of the stages

*Configurations and commands*

After the connection, I should consider the configurations of the hardware. Table 3-3 shows the RS232 communication requirements between the controller and PC.

Table 3-3 RS 232 configurations

| Model | E517 (z) | E710 (x-y) |
|-----------|------------|------------|
| data rate | 115.2kbps | 9600 |
| data word | 8 bits | 8 bits |
| stop bits | 1 | 1 |
| parity | none | none |

Five example sets of commands were usually used in closed position control (Table 3-4). Other commands are similar in application.

Table 3-4 commands

| commands | explanation |
|----------|-------------|
| *IDN? | type of controller, no matter if I have ^M^J or not. |
| SVO A1 | enable servo-control on channel A |
| MOV A14 | move PZT to 14 microns |
| MVR A-1 | move PZT to 13 microns(-1 relative to last target position) |
| POS?A | query of the current position of Axis A PZT |

## 3.5.3 Camera control

Two CCD cameras were used to capture images of the sample and back focal plane. They were connected to the lab PC via the fireware 1394b interface. Settings of the cameras, like shutter speed, gain, etc can be controlled by the controlling software. The hardware connection is shown in Fig. 3-16.
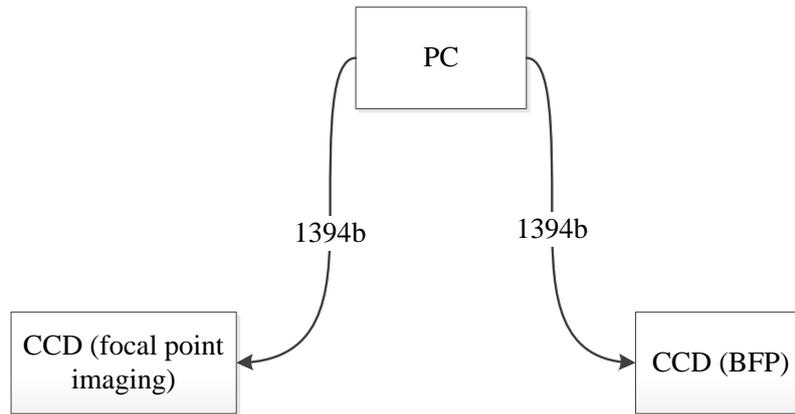
Fig. 3-16 CCD cameras connection

## 3.5.4 SLM control

According to the requirements of the reflected SLM from ForthDD Ltd, two kinds of software are applied. One is for sending image patterns to the SLM screen, the other one is used to control the operation of the SLM. Commercial software called FIVE DD, developed by ForthDD Ltd, is installed to operate the SLM. I developed a MATLAB program to generate patterns to the SLM. The overall design of the SLM application method is shown in Fig. 3-17.



Fig. 3-17  configurations software and pattern software

I adopted the MATLAB scripts on the LABVIEW platform to generate the SLM patterns. As the patterns vary with the pupil function I define, more details will in each chapter. Here, I only show the connection of the SLM to the PC.
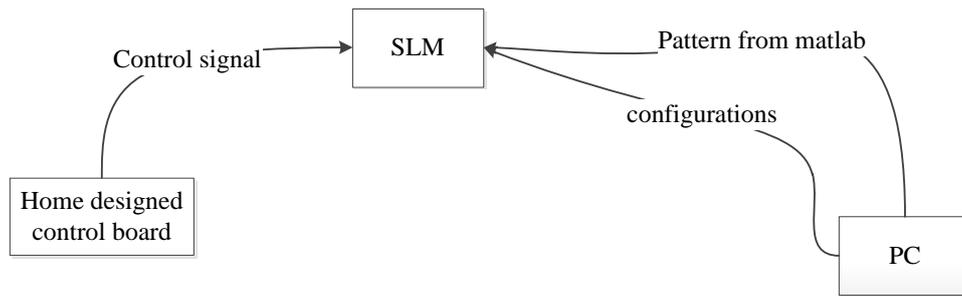
Fig. 3-18 hardware connection of the SLM

## 3.6 Imaging processing system

According to the experiment requirement, the imaging processing system can be integrated to the LABVIEW controlling software by using the MATLAB scripts in the LABVIEW, or can be used separately in MATLAB platform. No matter which situation is applied, the flowchart is as shown in Fig. 3-19.

```
                    ┌─────────┐
                    │  Start  │
                    └─────────┘
                         │
                         │◄──────────── No
                         ▼            │
                  ┌──────────────┐    │
                  │ Load images  │    │
                  └──────────────┘    │
                         │            │
                         ▼            │
                   ╱ Load ╲───────────┘
                  ╱finished?╲
                   ╲       ╱
                      │
                     Yes
                      ▼
              ┌──────────────┐
              │Find the gravity│
              │ center of the │
              │  focal point  │
              └──────────────┘
                      │
                      ▼
              ┌──────────────┐
              │Define pinhole │
              │    size      │
              └──────────────┘
                      │
                      ▼◄─────────────┐
              ┌──────────────┐       │
              │Integrate the │       │
              │response inside│      │
              │ the virtual  │       │
              │   pinhole    │       │
              └──────────────┘       │
                      │              │
                      ▼              │
              ┌──────────────┐   No  │
              │Calculate the │       │
              │  confocal    │       │
              │  response    │       │
              └──────────────┘       │
                      │              │
                      ▼              │
              ┌──────────────┐       │
              │Move to next  │       │
              │   point      │       │
              └──────────────┘       │
                      │              │
                      ▼              │
               ╱Finished all╲────────┘
              ╱ points in x-╲
               ╲ direction? ╱
                      │
                     Yes
                      ▼
              ┌──────────────┐
              │Define a defocus│
              └──────────────┘
                      │
                      ▼
              ┌──────────────┐
              │  Show the    │
              │grating image │
              └──────────────┘
                      │
                      ▼
                 ┌─────────┐
                 │   End   │
                 └─────────┘
```
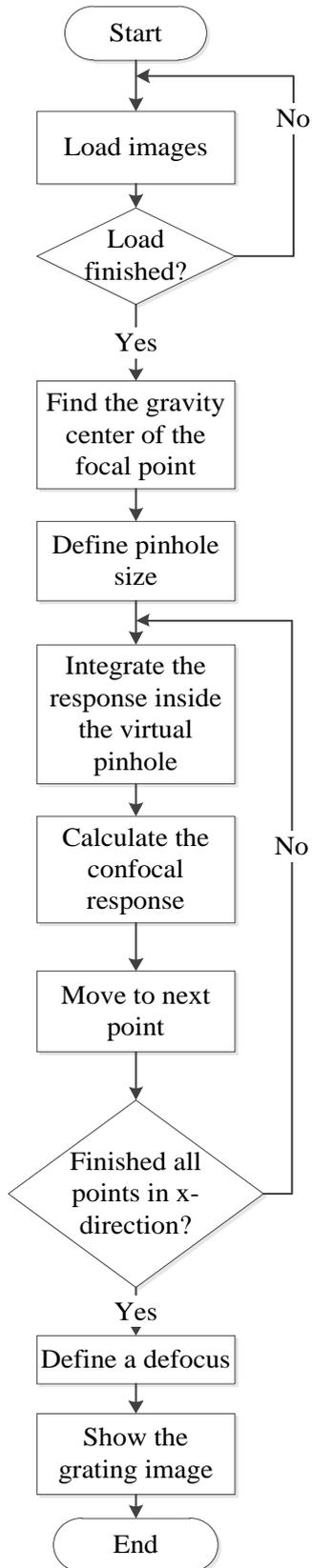
(1) To read all the images into the computer MATLAB environment;
(2) To find the centre of the focal points;
(3) To calculate the pinhole size according to different ratio;
(4) To fix the pixels which is located in the virtual pinhole ;
(5) To integrate the confocal intensity response;
(6) To calculate the confocal field response;
(7) To normalize the confocal field response;
(8) To draw  curves;
(9) To obtain the images of the sample;

Fig. 3-19 Flowchart of the data processing program

## 3.7 Modifying the system by using a phase SLM

In the above sections of this chapter, I introduced the development of a systematic instrumentation, including the optical part and control part, etc. Based on this instrument, I operated the experiment introduced in chapter 4: confocal surface plasmon resonance microscopy with pupil function engineering. Both the experimental $V(z)$ curves and grating line scan imaging based on that instrument worked well. However, after that experiment, I found some limitations of that system, for instance the experiment works better with a higher NA objective, limitations of amplitude modulation, etc. In order to optimize this project, another system was built up. The basic framework is similar and only two parts are modified, like using the NA1.45 objective to replace the 1.25NA objective and exploiting a phase SLM to replace the amplitude SLM.

### 3.7.1 NA=1.45 objective

During the experiment, I found that if the thickness of $SiO_2$ grating was bigger than 20nm, I were rather struggling modulating the back focal plane by using the proposed pupil function with the 1.25 NA objective lens, even if I have optimized the pupil function by blocking part of the background illumination. The distribution of the pupil functions and location of plasmonic angle is shown to illustrate the reason in Fig. 3-20. The SPR dip is shown in red curve when using the 50nm gold sample in air directly. The normalised intensity of the beam profile around the plamonic angle is about 0.88. However, if the dielectric is coated, for example, 30nm BSA (Bovine serum albumin, n=1.43), the plasmonic angle will be much higher and the beam intensity around this angle will be around 0.5 in theory. In the experiment, the ripples due to the SPs will be much worse for two reasons: firstly, the actual aperture of the system is lower than the nominal value 1.25; secondly the actual pupil function of the commercial objective varies with incident angle.
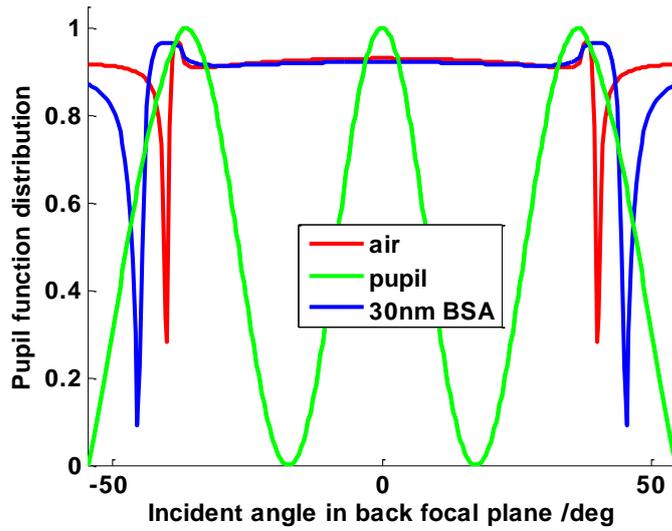
If NA=1.25
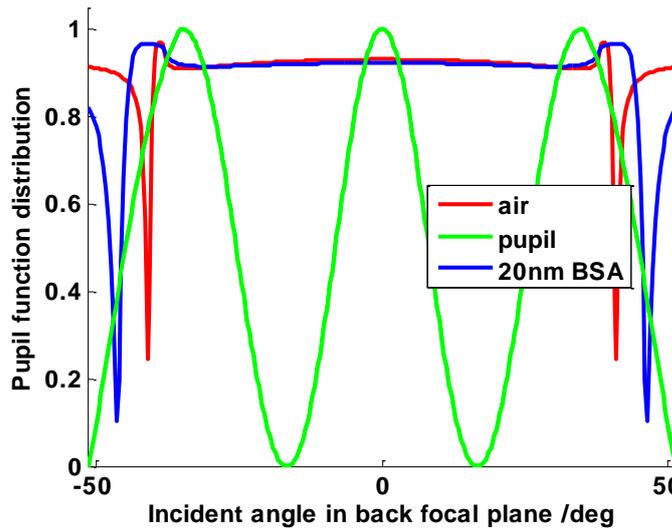


If NA is less than 1.25 and is about 1.20

Fig. 3-20 SPR dip movement of different samples when using 1.25 NA objective

In the experiment, I found that the actual NA of the nominal NA1.25 oil immersion objective lens is around 1.20. The beam intensity around this angle is around 0.3 in theory as shown in Fig. 3-20 (b), which makes the contrast much lower than I expected, not to mention that the original un-modulated beam profile is subject to the Gaussian function and the real pupil

function of the commercial objective lens is not uniform. For these reasons, I removed the 1.25NA objective lens and adopted another 1.45NA objective lens.

## 3.7.2 Phase SLM setup

The new system is similar to the old one, except for the SLM part. All the modifications are around the phase SLM, including the illumination part, hardware control connection part, and control software development part.

### *Optics of the modified system*

The schematic diagram of the optics is still as shown as in Fig.3-3. Only two parts are modified, beam expander and illumination source control. Firstly, as a higher NA objective lens is exploited. This means a bigger clear aperture can be obtained. In order to fill in the aperture of the 1.45NA objective lens, another stage of 2X beam expander is added in front of the old 10X beam expander, as shown in the red dashed line box in Fig. 3-21.
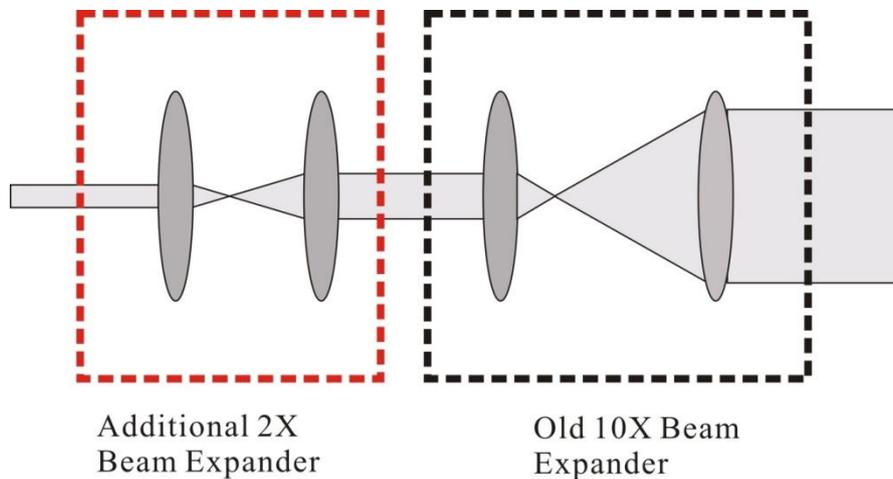


Fig. 3-21 Modified beam expander

Secondly, as the phase SLM does not require switching as described in section 3.4.3, the controlling part of the illumination source is much easier than the old one. Both the Bragg

Cell and high frequency generator can be removed from the controlling section. Hardware of the SLM control will be introduced in detail in 5.2.3.

Thirdly, optics alignment of the phase SLM is different. In the alignment of the amplitude SLM one, a polarized beam splitter was used and a polarizer was located in front of the amplitude SLM to make sure that all the input beam to the amplitude SLM to be's'; while in the new alignment, a normal non-polarized beam splitter was applied and a half wave plate was put in front the phase SLM as shown in Fig. 3-22. A half wave plate is located in front of the SLM to adjust the polarization of the illumination, which defines the modulation mode of the phase SLM. By rotating the half wave plate, I can use the pure phase mode of the SLM. Details on how to define and adjust different modes of the phase SLM will be provided in next section. If the pixel is 'on', the phase of the beam will be modulated and if it is 'off', no modulation is applied. Since a non-polarizing BS is used, both the modulated and un-modulated beam can pass through the BS. Considering the whole SLM, by setting some of the pixels 'on' and some pixels 'off', which means: some pixels are modulated and some pixels are un-modulated, I can generate the phase pattern. The method of generating patterns will be introduced later in section 3.7.3 of this chapter. Specific patterns I applied in the experiments will be introduced in each chapter of the experiments themselves.
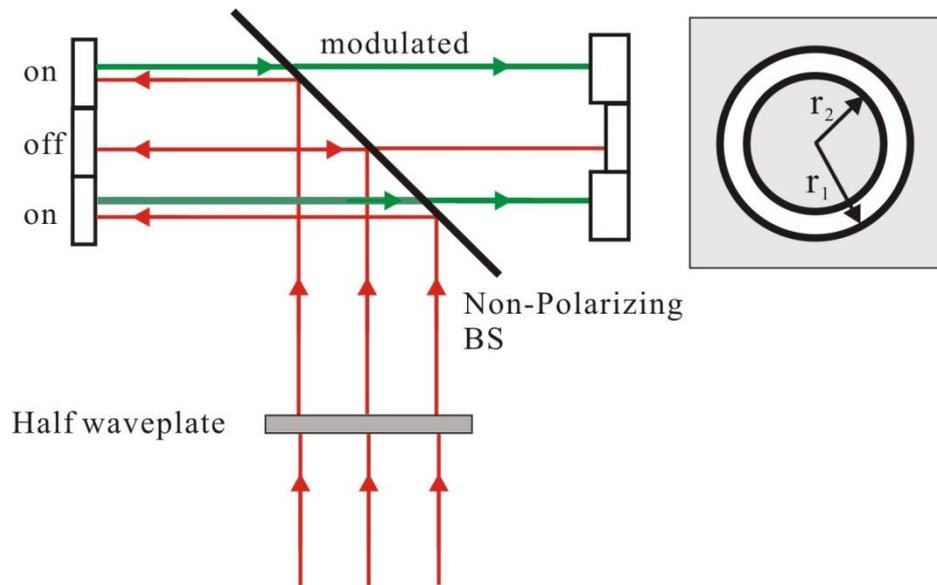
Fig. 3-22 optics alignment of the phase SLM

## *Hardware connection*
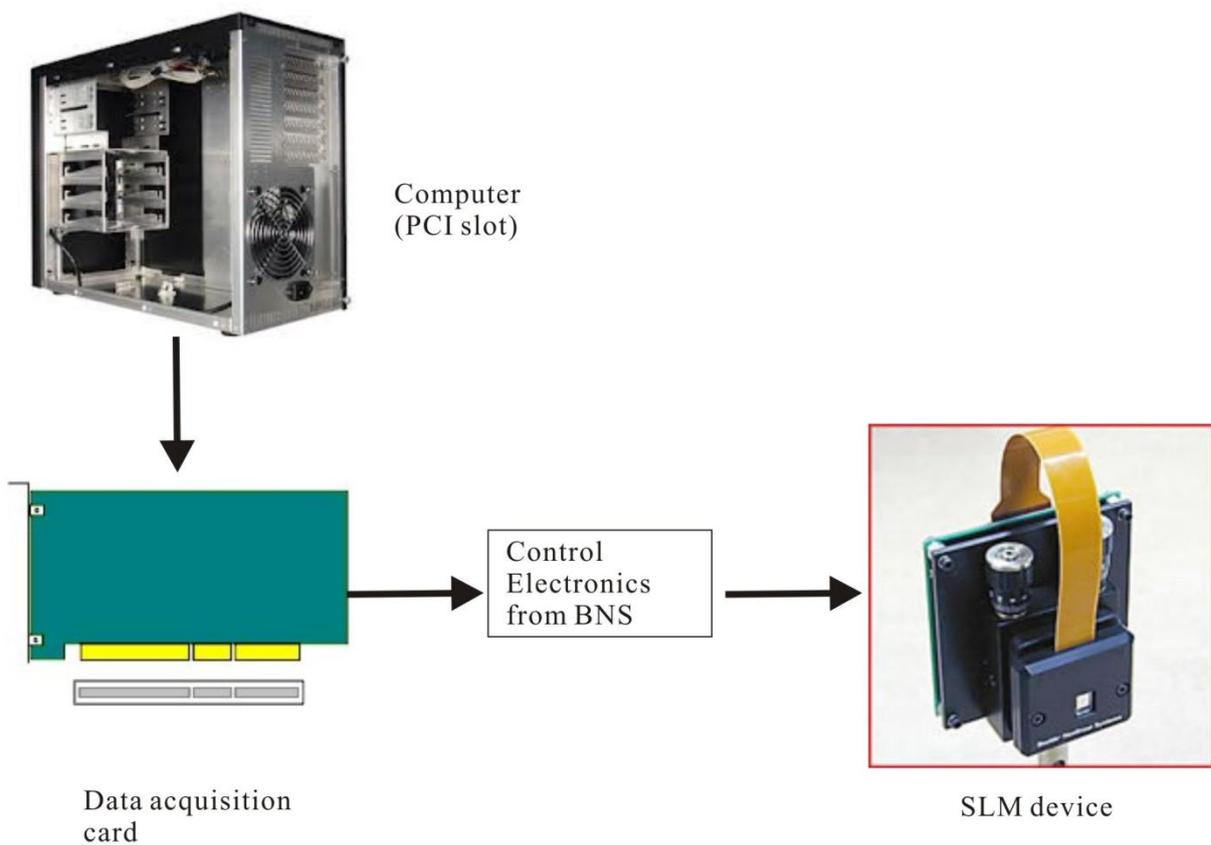


Fig. 3-23 hardware connection

*Control software development*

The general flowchart is shown in Fig. 3-24. It includes 4 steps:

1) Read interface.ini to initialize the SLM, including :

   ➢ Liquid crystal type

   ➢ Toggle rate

   ➢ Frame rate

   ➢ Laser setting

   ➢ Path to a sequence file (user defined SIF file (.sif)):

   One thing needs to be paid attention here. For the user developed labview software, the images files can be located any disc in the computer; however, if using the commercial software (BLINK) from the BNS Company, all the controlling bmp image files should be copied to the Image subfolders under the software installation folders.

   ➢ Path to a SLM phase compensation file

   ➢ Path to the system phase compensation file (ignored if no)

2) For the first loop to operate the SLM, the normal routine is :

   ➢ Call construction, which will open the communication to the hardware

   ➢ Set Download mode

   ➢ Preload a sequence of images to the memory

   ➢ Set run parameters, like Frame rate and Laser setting, etc

   ➢ Read LUT (look-up table) file

   It needs to illuminate that the LUT of slm7186.lut should be used for the linear case, other than the linear.lut.

   ➢ Load compensation files

   ➢ Update the SIF file

➢ Select image (which image needs to be read currently)

3) In the following procedure

➢ Turn on the power

➢ Select Image

➢ Turn off the power

4) After all the procedure, call the deconstruction to close the communication to the hardware

```
┌─────────────┐
│    Start     │
└─────────────┘
       │
       ▼
┌─────────────┐
│  Initialize  │
│     SLM      │
└─────────────┘
       │
       ▼
    ◇ Is it the first      ┌──────────────────┐
      time to operate ─Y→  │  Run the normal   │
      the SLM ◇            │ routine procedure │
       │                   └──────────────────┘
       N                            │
       ▼                            │
┌─────────────┐◄────────────────────┘
│  Run the     │
│  simplified  │
│  procedure   │
└─────────────┘
       │
       ▼
┌─────────────┐
│    Call      │
│ deconstructio│
│   n dll      │
└─────────────┘
       │
       ▼
┌─────────────┐
│    End       │
└─────────────┘
```
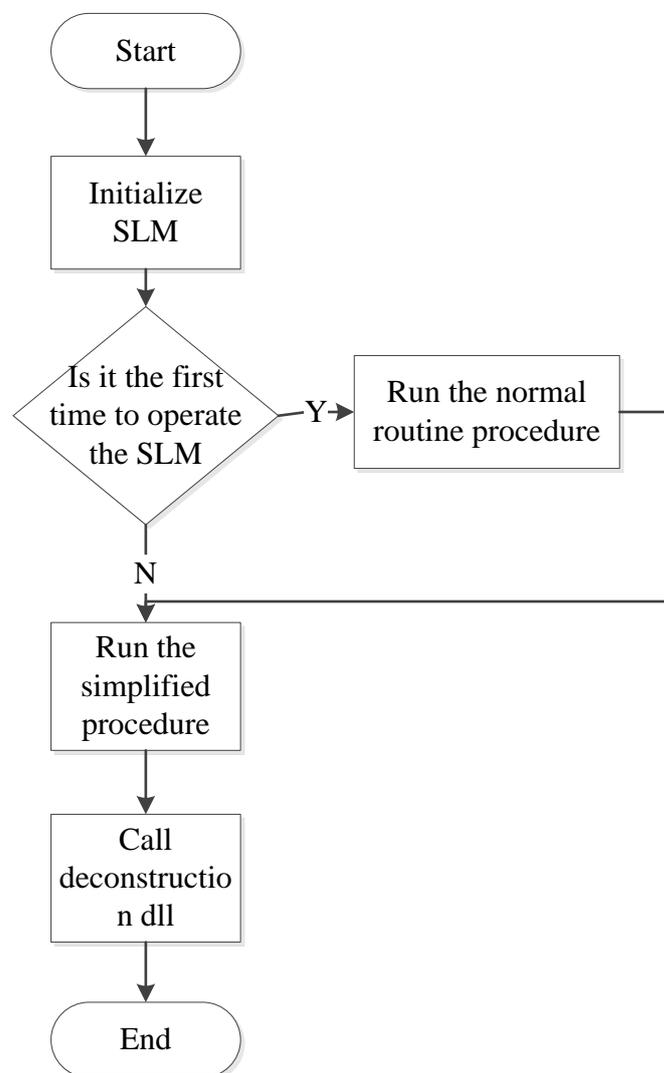
Fig. 3-24 flow chart of the software control

### 3.7.3 Phase SLM modulation

In this system, I have to use only one phase SLM to modulate both the amplitude and phase simultaneously and independently. Reasons will be explained in chapter 5 and 6. In this section, firstly, I will show the method to modulate the amplitude by using an only-phase SLM; then I will show how to modulate the pure phase by using the only-phase SLM; Finally, I will show if the modulation of the two terms is independent.

### 3.7.4 Amplitude modulation by using a phase SLM

Here, I will show how to modulate an amplitude pattern by using a phase SLM. I devise a method of using four pixels on the PSLM as a cell to eliminate the amplitude (Fig. 3-25).

| 0 | pi | 0 | pi |
|---|----|---|----|
| pi | 0 | pi | 0 |
| 0 | pi | 0 | pi |
| pi | 0 | pi | 0 |

Fig. 3-25 Four pixels to eliminate the amplitude

As I use the phase mode of the phase SLM, theoretically, the pixels of different phase should have same amplitude. For each pixel, the amplitude can be expressed as:

$$A = A_m \cos(\omega t + \phi_0) \qquad \text{Eq.3-5}$$

For the 1D case,
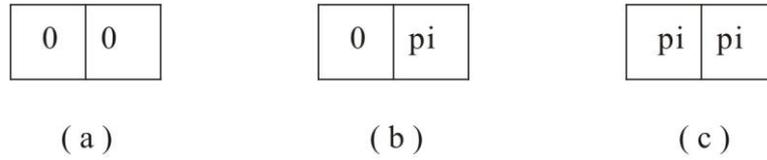


Fig. 3-26 1D pixel pairs of phase elimination

Let us take a pixel pair with different phase (Fig. 3-26 b) to calculate the effective amplitude.

$$A_1 = A_m \cos(\omega t + 0)$$
$$A_2 = A_m \cos(\omega t + \pi)$$

Eq.3-6

By adding $A_1$ and $A_2$,

$$A_{tot} = A_1 + A_2 = A_m \cos(\omega t + 0) + A_m \cos(\omega t + \pi) = A_m \cos(\omega t + \tfrac{\pi}{2})\cos(\tfrac{\pi}{2}) = 0 \quad \text{Eq.3-7}$$

For the (Fig. 3-26 a) and (Fig. 3-26 c) case, obviously, the amplitude will be doubled.

In the experiment, a 2D pattern is needed for the amplitude modulation. Therefore, I need to use four pixels as a cell to eliminate the amplitude and simulate the real amplitude pupil function patterns (Fig. 3-27).
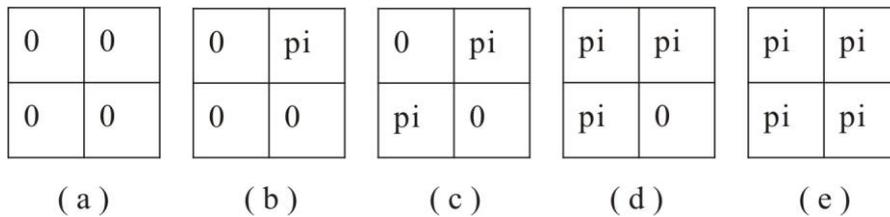


Fig. 3-27 2D pixels cells of phase elimination

## 3.7.5 Phase pattern modulation

In order to modulate the phase pattern, I need to obtain the relation between greyscale level and phase variation. I built a simple system and obtained the relation by fitting the curve as shown in Fig. 3-28. Blue curve is the plotted experiment data and red line is the fitted data.
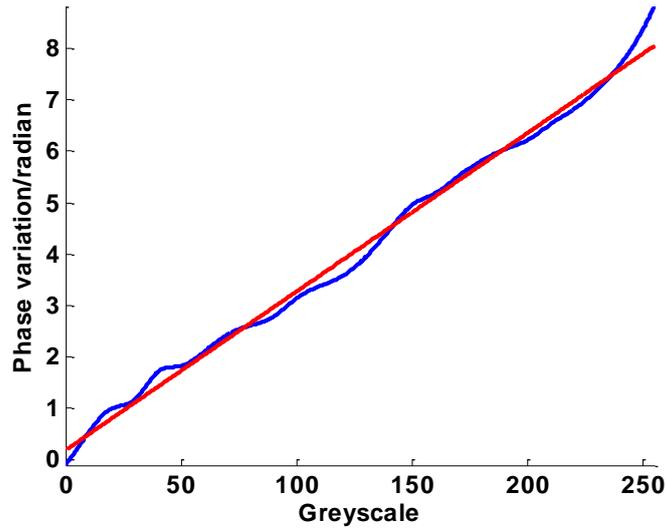
Fig. 3-28 Relation between the greyscale level and the phase variations

After fitting the curve, I can find the function between the greyscale level and the phase variations:

$$P = \frac{1}{32.31} * G + 0.425 \qquad \text{Eq. 3-8}$$

Where, G is the greyscale level, and P is the phase variation.

In the experiment, actually, I need to calculate what kind of patterns I want to use according to the phase variations I want, so the reverse function is:

$$G = 32.31 * P - 1.374 \qquad \text{Eq. 3-9}$$

As greyscale level cannot be negative, I rewrite the function to be

$$G = 32.31 * (P - 0.425) \qquad \text{Eq. 3-10}$$

The principle I used to modulate the phase in the experiment is just based on this function. A table (Table 3-5) is calculated to show how I modulate the phase by varying the greyscale level of the input BMP file. In the phase stepping experiments in chapter 6, the 0, 90°, 180°, 270° phase shifts were obtained from the blue calibration curve rather than the linear fit.

83

Table 3-5 phase modulation lookup table

| | | $\dfrac{\pi}{2}$ | $\pi$ | $\dfrac{3\pi}{2}$ | $2\pi$ |
|---|---|---|---|---|---|
| Theoretical phase | 0 | | | | |
| Calibrated phase | 0+0.425 | $\dfrac{\pi}{2}$+0.425 | $\pi$+0.425 | $\dfrac{3\pi}{2}$ + 0.425 | $2\pi$ + 0.425 |
| Greyscale (0-255) | 0 | 50.7 | 101.5 | 152 | 203 |
| Greyscale (0-1) for BMP file | 0 | 0.1990 | 0.3981 | 0.5971 | 0.7961 |

For example, if I want to generate a pattern with phase rings from 0 to $2\pi$ as shown in Fig. 3-29 (a), by using the function I obtained or look-up the above table, I can generate the greyscale BMP file as shown in Fig. 3-29 (b). Then I load the bmp to the SLM to modulate the phase profile. It is necessary to point out that this bmp is just an example pattern. For the respective experiment, I will design and generate the patterns according to the specific experimental requirements.
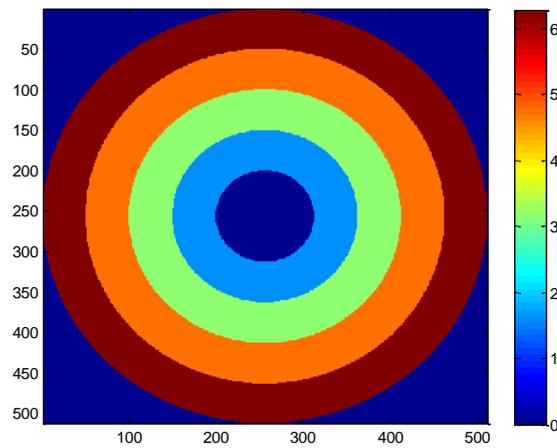


(a)
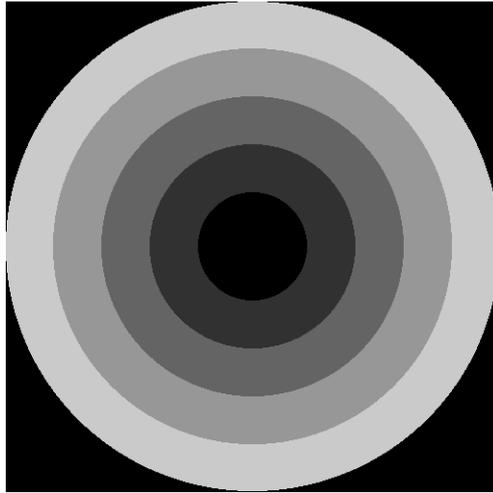
(b)

Fig. 3-29 An example of generating pattern and modulate the phase profile; (a) an example of phase ring pattern;

(b) the generated greyscale BMP image calculated from the phase ring pattern in (a).

## 3.8 Summary

In this chapter, I have described the development of the experimental system, including the optics system, controlling system, data processing system, etc. owing to the limitations of the old system, another new system was designed. As the whole framework exist the same, only two modifications were introduced briefly: i) higher NA objective lens; ii) phase SLM. Details on how to modulate the phase SLM and the test of the phase SLM before applying it will be demonstrated in chapter 5.

# 4 Confocal surface plasmon resonance microscopy with pupil function engineering

Surface plasmon microscopy can measure local changes of refractive index on the micro scale. Interferometric plasmon imaging delivers quantitative high spatial resolution images sensitive to refractive index. In addition, the so called *V(z),* allows image contrast to be controlled by varying the sample defocus without substantially degrading spatial resolution. Here, I show how a confocal system provides a simpler and more stable alternative. A spatial light modulator is applied to engineer the microscope pupil function to suppress light that does not contribute to the signal and smooth the sharp edge of the aperture to remove the noisy frequency. In this chapter, I will firstly provide a simple introduction, theory of *V(z)*, pupil function engineering, simulation results and lastly experimental results.

## 4.1 Introduction

It has been shown previously in section 2.3.4 that a scanning heterodyne interferometric microscope with an oil immersion objective can be used for high resolution surface plasmon (SP) imaging [4, 5, 7, 8]. The essential idea is that when the sample is moved above the focal plane of the objective there are two major contributions to the output signal one arising from the SP and the other arising from light directly reflected from the sample. As the sample is defocused the relative phase between these contributions changes leading to an oscillating signal whose period depends on the angle of incidence at which SPs are excited. More recently this idea has been extended to a wide-field configuration [9].

The problem associated with the interferometric configuration is that it places severe demands on system stability and in the case of the heterodyne system acousto-optic

modulators and associated electronics are required. The scanning heterodyne interferometer [4, 5, 8] involves a separate reference and sample arm which places severe demands on system stability. The confocal SP system offers a more compact and stable alternative which is compatible with commercial instruments.

In the previous scanning interferometer the interference signal is recovered from the product of the returning field in the back focal plane (BFP) and the reference beam so that this signal is proportional to the integral of the reflected field (assuming a uniform reference beam). An ideal confocal system is also dependent on the integral of the field returning from the sample. This can be easily understood by realizing that the lens A of Fig. 1-2 performs a Fourier transform between the BFP and the pinhole plane. The signal on the axis of the pinhole plane is therefore proportional to the DC or average value of the field in the BFP which is, in turn, proportional to the integral of the field in the BFP. Since the detected field is proportional to intensity the output depends on the square of the integral of the field which gives reduced contrast as discussed below.

## 4.2 Theory of confocal scanning SPRM

### 4.2.1 Theory of $V(z)$

The output signal from a confocal microscope with a small pinhole can be written, with a simple modification of the formulation given for the heterodyne interferometer[4] as:

$$I_{co}(z) = |V(z)|^2 = \left| \int_0^{2\pi} \int_0^{s_{max}} P_{in}(s) P_{out}(s) \left[ \alpha(\phi) r_p(s) + \beta(\phi) r_s(s) \right] \exp(2jnkz\cos\theta) ds d\phi \right|^2 \qquad \text{Eq. 4-1}$$

Where $I_{co}(z)$ is the output signal as a function of defocus, $z$. $V(z)$ is the field as measured in an interferometer. $P_{in}$ and $P_{out}$ are the input and output pupil functions as a function of $s$, the sine of the incident angle, $\theta$. $r_p(s)$ and $r_s(s)$ are the complex amplitude reflection coefficients for $p$-

and *s*- polarizations respectively. $\alpha(\phi)$ and $\beta(\phi)$ represent the variation in the proportion of *p*- and *s*- polarized light respectively as a function of azimuthal angle, $\phi$; for linear input polarization (and copolar detection) $\alpha(\phi)=cos^2(\phi)$ and $\beta(\phi)=sin^2(\phi)$, for radial $\alpha(\phi)=1$ and $\beta(\phi)=0$. *n* is the refractive index of the immersion oil, and *k* is $2\pi/\lambda$, where $\lambda$ is the free space wavelength of the light. In this chapter, all the theoretical *V(z)* curves are calculated using Eq. 4-1. For the gold sample, $r_p$ and $r_s$ are calculated using the model of three layers Fresnel equations and the code written by Somekh mentioned in section 2.1.4. For a non-plasmonic sample like an ideal mirror, I use $r_p=1$ and $r_s=1$.

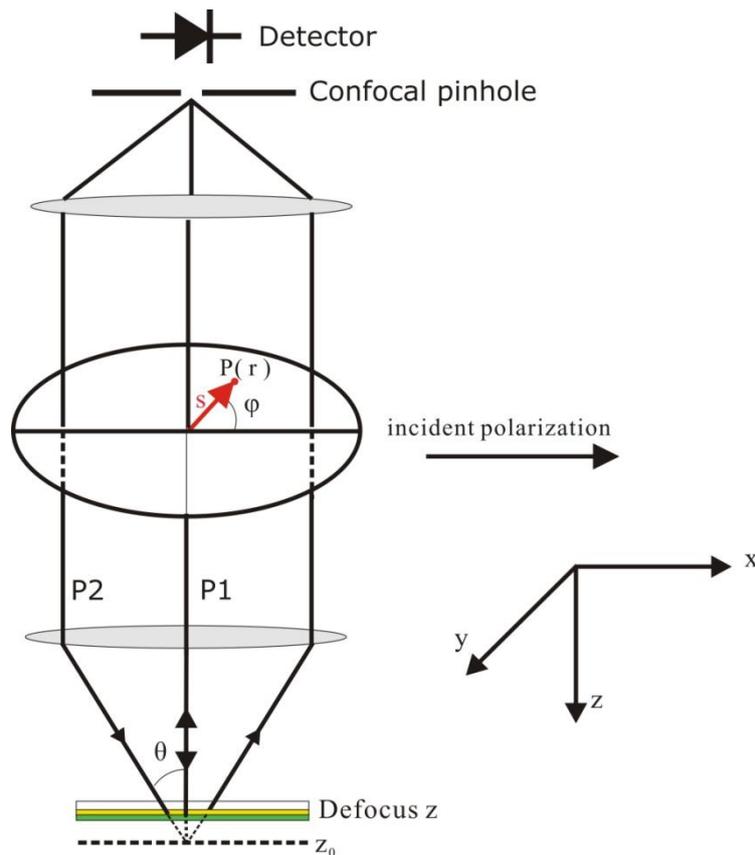The systematic diagram is shown in Fig. 4-1.



Fig. 4-1 systematic diagram of defocus and back focal plane

The true confocal response can be regarded as coherent since it is formed as the integral of a field; however, for finite size pinholes the response becomes partially coherent and cannot be written as a single integral over field or intensity. Apart from the squaring effect there is one other difference between the interferometric and confocal response. In the interferometer, the reference beam acts as a polarizer so only copolar components are detected, if there is no polarizer before the pinhole then cross polar components can also be detected. The total intensity detected is therefore the sum of copolar and cross polar, $I_{cr}(z)$ contributions

$$I_{tot}(z) = I_{co}(z) + I_{cr}(z)$$     Eq. 4-2

Where the $I_{cr}(z)$ is given by equation 1 with $\alpha(\phi) = \beta(\phi) = \frac{1}{2}\sin 2\phi$ for linear polarization.

For a point pinhole the cross polar terms disappear[86], and increase as the pinhole is opened. In previous literature [4, 5], the researchers have demonstrated that the $V(z)$ effect exists in a two arm interferometric system. Here, I show that the same $V(z)$ effect also exists in the confocal system.

## 4.2.2 Period of ripples on $V(z)$

Examining Fig. 4-1 I see that the presence of the confocal pinhole ensures that only light appearing to come from the focus returns to the pinhole. The presence of the confocal pinhole thus defines the allowable propagation paths (P2 of Fig. 4-1) of the detected SPs thus ensuring that the resolution is determined by the footprint of the optical beam rather than their propagation length [5]. When the sample is moved away from the focus towards the objective there are two major contributions to the signal detected at the confocal pinhole. The first is light close to normal incidence that will return to the pinhole and the second is the SP path discussed above. As the sample is defocused by a distance $\Delta z$, under conditions discussed below, the phase between the normal incident beam and the SP beam changes:

$$\Delta\phi_{ref} = \frac{4\pi n}{\lambda}\Delta z \qquad\qquad \text{Eq. 4-3}$$

$$\Delta\phi_{plas} = \frac{4\pi n}{\lambda}\cos\theta_p\ \Delta z \qquad\qquad \text{Eq. 4-4}$$

Where the subscripts 'ref' and 'plas' denote the phase shifts associated with the normal incidence and the plasmon beams, n is the refractive index of the couplant, essentially, the coupling oil, $\theta_p$ denotes the incident angle of the SP, and $\lambda$ is the wavelength of the illuminating radiation in vacuum. The relative phase between the reference and the SP contributions at the pinhole thus varies with defocus $\Delta z$ as:

$$\Delta\phi = \frac{4\pi n}{\lambda}\left(1-\cos\theta_p\right)\Delta z \qquad\qquad \text{Eq. 4-5}$$

So that the relative phase changes by $2\pi$ with a period given by:

$$\Delta z_p = \frac{\lambda}{2n\left(1-\cos\theta_p\right)} \qquad\qquad \text{Eq. 4-6}$$

This $2\pi$ phase shift corresponds to one cycle of oscillation observed on the so-called *V(z)* curve, so the period of the oscillation can be used to determine $\theta_p$ from which the real part of the wave number of the SP ($= 2\pi n\sin\theta_p/\lambda$) or phase velocity $c/(n\sin\theta_p)$ can be determined.

## 4.2.2 'Virtual' pinholes of confocal microscope

In a confocal microscope, the performance depends on both the illumination and the detection. The light from the sample is imaged onto a 'pinhole' in the image plane, however, the illumination is in the form of a focused spot coming from a collimated beam as the image from a point sample. Although traditionally a physical pinhole is used in confocal microscopy, it is often more convenient to use an electronically configurable pinhole. That means the physical aperture in the imaging space is unnecessary. Instead, selection of the CCD pixels determines the pinhole size as shown in Fig. 4-2.
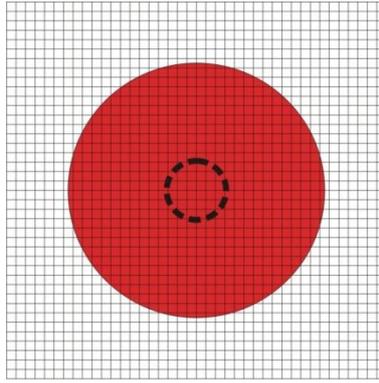
Fig. 4-2 Schematic diagram of scanning point image on CCD

The squares refer to the pixels of CCD, the orange refers to the centre of focal point of the scanning point, and the red refers to the Airy disc in the system. From this point of view, it can be seen that in the system, the actual aperture is not a physical one. Actually, what I use is a virtual aperture, whose size can be defined in the imaging processing programs. This solution makes the system much easier and more versatile than a traditional confocal one. For instance, it is more convenient to adjust the aperture size according to different applications. Apparently, the solution by using virtual concept instead of physical object is consistent to the trends of modern science. More details about how to process the images will be provided in the image processing section.

### 4.2.3 Influence of pinhole size on $V(z)$

It is well known that the pinhole is the 'soul' of the confocal technique. As the system adopts the confocal technique, it is necessary to discuss the influence of pinhole size to $V(z)$. What will happen if I use different pinhole sizes, as shown in Fig. 4-3.
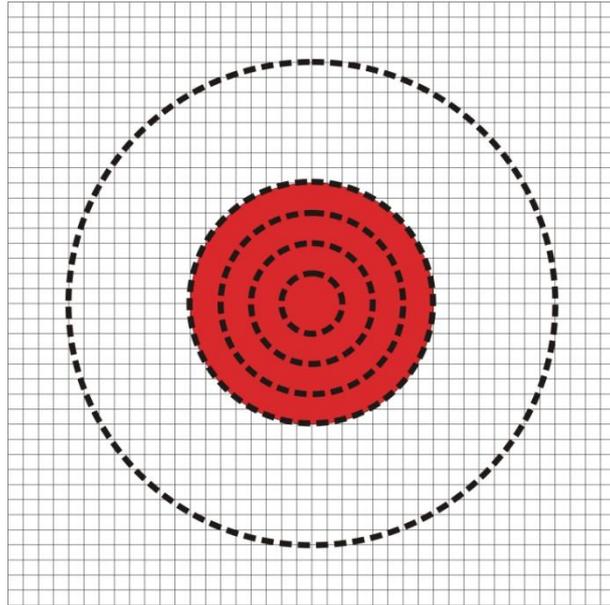
Fig. 4-3 different pinhole sizes

Fig. 4-4 shows simulation results obtained for the confocal system as a function of defocus for different diameters of pinhole. From the curve I note the periodic ripple for negative defocus characteristic of the interference between the direct reradiation reference and the excited SPs. The presence of the pinhole means that only those that appear to come from the focus pass through the pinhole. This leads to a characteristic periodicity of the ripple, $\Delta z$, given by Eq. 4-4. The confocal arrangement thus serves to define the path of the SPs. As the pinhole becomes wider SPs emitted from different positions are detected and I would expect the ripples to become less well defined as can be seen from the simulation results in Fig. 4-4.

Fig. 4-4 Simulated *V(z)* curves for different pinhole diameter. Solid curve 50nm bare gold, dashed curves gold with 10nm overlayer with refractive index 1.5. Each pinhole diameter displaced by 0.1 in y-axis and overlayers displaced by 0.05 in y-axis to distinguish the curves. Pinhole radii defined in terms of radius of Airy disc (0.61λ/NA ) are shown in the legend.

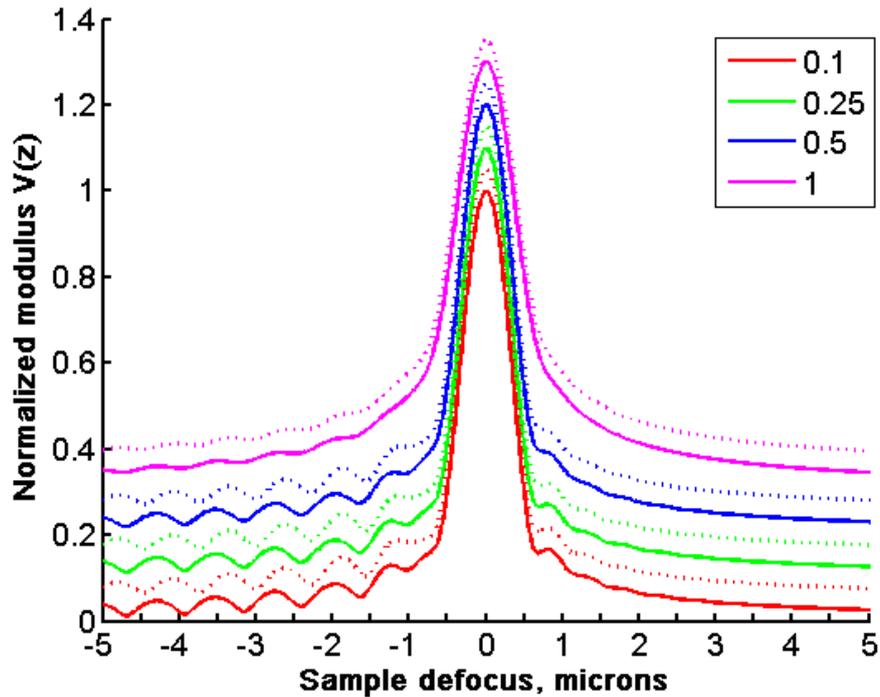It can be seen that for a pinhole radius less than 0.25 of the radius of the main lobe of an Airy disc the response is almost the same as the ideal confocal case with a point pinhole. For values of 0.5 the ripples become less distinct almost disappearing when the pinhole is equal to the radius of the Airy disc. The plots of Fig. 4-4 include both copolar and cross polar components as described by Fig. 4-4, however, the effect of the cross polar term for pinhole diameters less than 0.5 was considerably less than 1% of the total signal. The dashed curves of Fig. 4-4 show the same situation with a 10nm coating of index 1.5, and that the period of the ripples changes allowing the local refractive index of the layers to be determined. It should be noted that in order to see the lower levels in Fig. 4-4 clearly, the plots of Fig. 4-4 show $\left|\vec{V}\left(z\right)\right|$ or $\sqrt{I\left(z\right)}$ which is, of course, what is measured in an interferometer but in the confocal arrangement I detect the square of this quantity which means that the range of

93

signals between the peak value and the ripples will be much greater. Later I will discuss the use of different pupil functions that reduce the range of signals and enhance the ripples relative to the peak signal in section 4.3.4. Throughout this thesis I plot the magnitude of the field rather than the measured intensity for clarity.

# 4.3 Pupil function engineering

In this experiment, I proposed a technique of pupil function engineering to modulate the pupil function of the system. I developed several pupil function patterns and used an amplitude-SLM (ASLM) to realize it experimentally. Here, I will first describe why I require pupil function engineering and analyze it from simulation, secondly, how to realize it in an experiment by selecting pixels and random to be 'on' and 'off' as described in chapter 3, thirdly showing simulation results described.

## 4.3.1 Pupil function engineering

*Sharp edge effect on non-plasmonic case*

I do not want spurious ripples to exist when a non-plasmonic sample is used. However, because of the sharp edge effect on a non-plasmonic sample, ripples do exist on $V(z)$ of non-plasmonic case as shown in Fig. 4-5. These ripples can be calculated by using the Eq. 4-1 in section 4.2.1. For a mirror sample, both of $r_p$ and $r_s$ equal to 1 therefore the $V(z)$ response of the mirror will be :

$$|V(z)| = \left| \int_0^{2\pi} \int_0^{s_{max}} P_{in}(s)P_{out}(s)\left[\alpha(\phi)+\beta(\phi)\right]\exp(2jnkz\cos\theta)dsd\phi \right| \qquad \text{Eq. 4-7}$$

For p polarization,

$$\begin{aligned}\alpha(\phi) &= 1 \\ \beta(\phi) &= 0\end{aligned} \qquad \text{Eq. 4-8}$$

So

$$|V(z)| = \left| \int_0^{s_{max}} P_{in}(s) P_{out}(s) \exp(2jnkz\cos\theta)ds \right| \qquad \text{Eq. 4-9}$$

As the system is a reflection one, the beam passes the objective lens twice so the input pupil function and the output pupil function are the same and both of them refer to the pupil function of the objective lens, expressed as:

$$|V(z)| = \left| \int_0^{s_{max}} P_{obj}^2(s) \exp(2jnkz\cos\theta)ds \right| \qquad \text{Eq. 4-10}$$

Where, s refers to sine of the incident angle.

Eq. 4-10 shows that the *V(z)* response of a mirror is actually the Fourier transform of the pupil function of the objective lens with the change of variable [6, 87]. Because of the limited clear aperture of the objective lens, the edge is relatively sharp which will generate some ripples on the Fourier transform of the objective lens pupil function, the response of *V(z)* of mirror. Details on the mathematical derivation can be found in [6]. The period of the ripples is about 0.48 microns when using a NA1.25 objective lens. Actually, the method of measuring the period of the ripples can be used to evaluate the objective lens and check if the actual NA is that quoted by the manufacturer[81]. For example, if I decrease the NA to be 1.20, the period is about 0.53μm, which matches with the experimental results shown later in the experimental section (Session 4.5).  It is necessary to mention that the amplitude of the first ripple is about 8.6% of the peak value and the second one is about 3.7%. These data will be used below to compare the contribution from the SPR and the sharp edge.
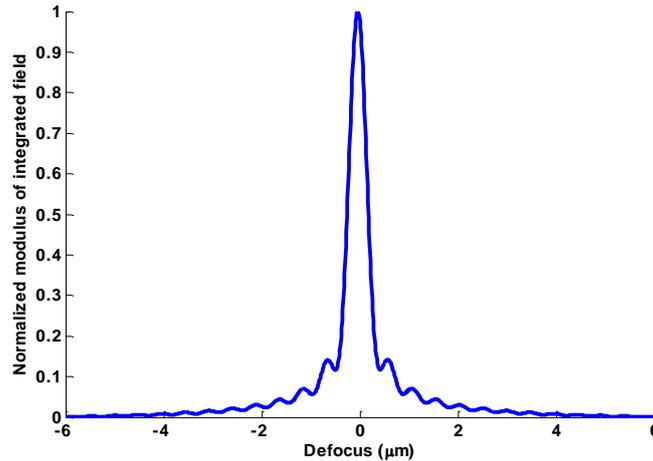
Fig. 4-5 *V(z)* of non-plasmonic sample. The ripples are caused by the sharp edge effect.

## *Influence of sharp edge effect to plasmonic case*

Ideally, there should be no sharp edge effect at all, which means that no ripples exist for a non-plasmonic sample. Or, from the point view of the experiment, if the ripples of the noisy sharp edge effect are much smaller than the SPR signal ripples, I can ignore the noisy ripples. However, if they are comparable, I need to take the noisy ripples into account. Both simulation and experiment have been done to compare them. Here, I will demonstrate the simulation result as shown in Fig. 4-6. Experimental results can be found later this chapter in the experiment results section (section 4.5). The plasmonic sample here in the simulation is a sandwiched three-layer structure, which comprises of coverglass (n=1.518), 50nm Au and air. The *V(z)* of the plasmonic case is a combination of the SPR effect and noisy sharp edge effect. The *V(z)* of the non-plasmonic case is the sharp edge effect.

Ideally, the plasmonic case should have a regular period ripples on its *V(z)* curves. However, because of the sharp edge effect, the combined *V(z)* curve of the plasmonic case shows an irregular periodic structure. Furthermore, the sharp edge ripples have comparable amplitude with the SPR ripples. It is for this reason that I proposed the technique of pupil function

engineering. Another advantage of improved SNR resulting from pupil function engineering will be discussed later in section 4.3.4.
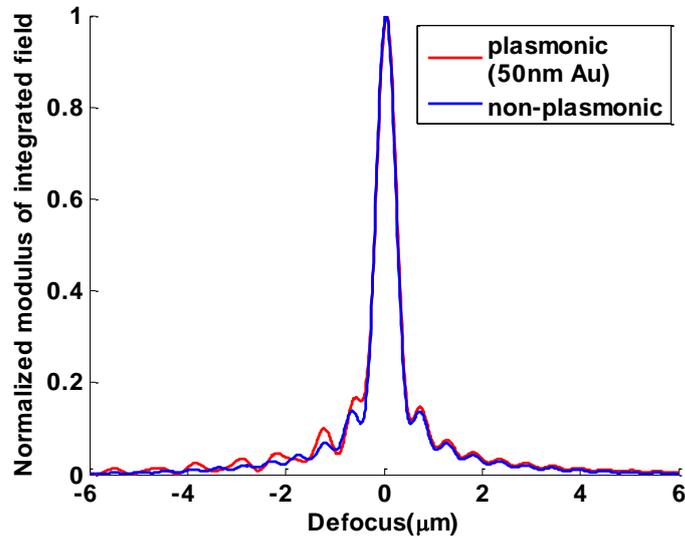


Fig. 4-6 *V(z)* curves comparison between plasmonic and non-plasmonic samples

## 4.3.2 How to remove the sharp edge ripples

As the illumination beam is increased, the beam profile in the aperture of the objective lens is almost flat, as shown in Fig. 4-7 (a). I call this sharp edged illumination. Its 2D profile is shown in Fig. 4-7 (b). As I analyzed above, in order to eliminate the noisy ripples on the *V(z)* curves, I need to smooth the edge of the pupil function. I propose a function which can fulfil my purpose as shown in Fig. 4-7 (c) and (d). Compared to the sharp edged illumination, the pupil function I proposed is quite smooth. The distributions of the un-modulated pupil function and modulated pupil function are shown in Fig. 4-7. The Fig. 4-7 (a) is the 1D un-modulated pupil function distribution and Fig. 4-7 (b) is the 2D distribution. The excitation of SPR by p-wave is also shown in green line. Fig. 4-7 (c) is the 1D modulated pupil function distribution and Fig. 4-7 (d) is the 2D distribution. It illustrates clearly that the pupil function I proposed is smooth enough at the edge of the aperture.
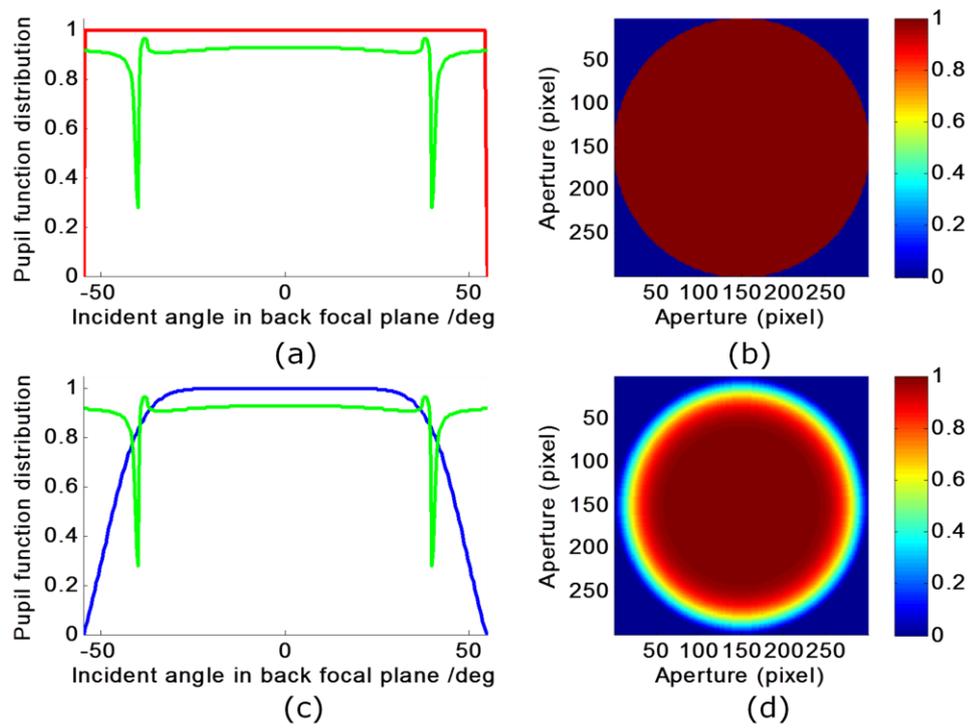
97

Fig. 4-7 Distribution of the un-modulated pupil and modulated pupil function

A comparison between different $V(z)$ curves using the sharp edged pupil and the pupil function modulated illumination is shown in Fig. 4-8.



(a)
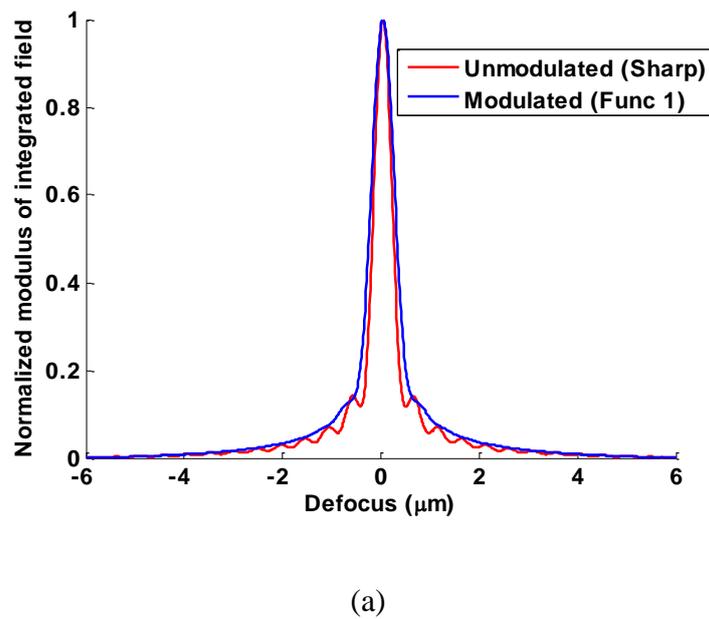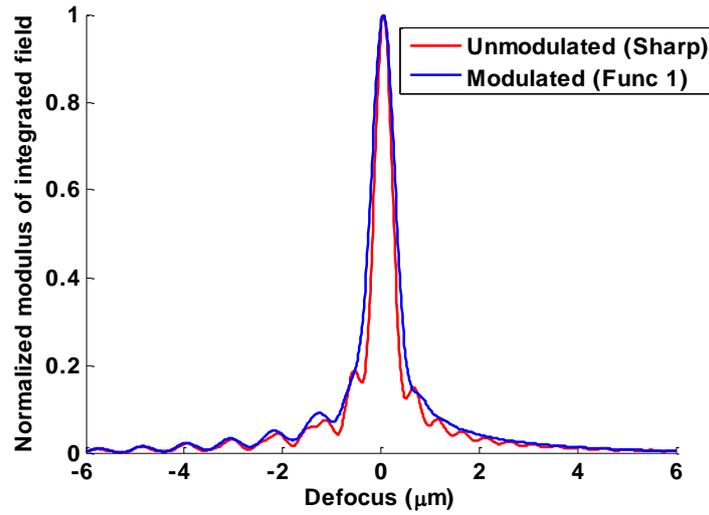
(b)
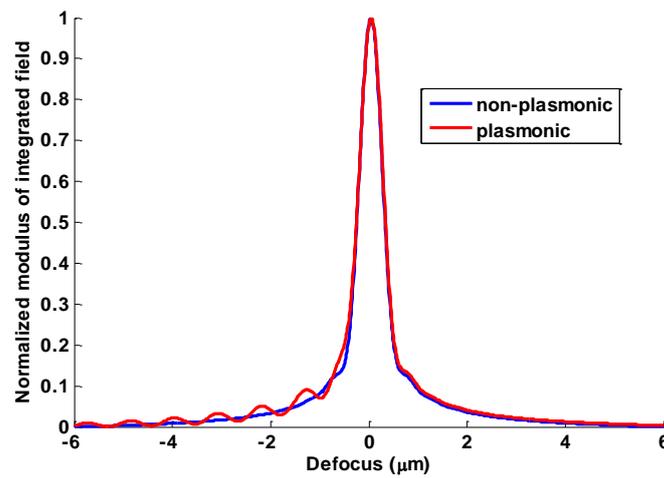


(c)

Fig. 4-8 *V(z)* curves comparison between the sharp edged and the pupil function modulated illumination; (a) with a

non-plasmonic sample; (b) with a plasmonic sample (coverglass/50nmAu/air); (c) *V(z)* curves comparison between

the non-plasmonic and plasmonic sample with the pupil function modulated illumination

Fig. 4-8 (a) shows the *V(z)* curves comparison between the sharp edged and the pupil function

modulated illumination with a non-plasmonic sample. As expected, the *V(z)* curve with the

pupil function modulated illumination has less noisy ripples than those formed when using

the sharp edged pupil. When a plasmonic sample (coverglass/50nm Au/air) is inserted, by

eliminating the noisy pupil function ripples, the *V(z)* curves show regular ripples which are subject to a decaying exponential distribution, as shown in Fig. 4-8(b). In order to demonstrate the results clearly, I plot the *V(z)* curves of plasmonic sample and non-plasmonic sample by using the modulated pupil function in Fig. 4-8(c). It shows clearly that: i) by using the proposed pupil function, the noisy ripples are greatly reduced; ii) for a non-plasmonic case, the sharp edge ripples are very small on the *V(z)* curve; iii) for a plasmonic case, the ripples are regular as I expected. I also need to notice that the ripples have very small amplitude, is it possible to increase their magnitude? In the next section 4.3.4, I optimize the pupil function and make the enlargement of ripples possible.

## 4.3.3 Another application of pupil function engineering

After removing the noisy ripples, I find that the contrast is still very poor compared with the background. Here, I analyze the principle again to find the reason. Fig. 4-9 shows that basic principles of the confocal SPR system. As mentioned, *V(z)* is formed by interference between the directly reflected signal ('Ref') and the SP signal. Therefore, I can suggest that the illumination between the 'Ref' and 'SP' is useless background, as the black part shown in Fig. 4-9. This is the reason that the *V(z)* curves with the modified pupil function provides low contrast.
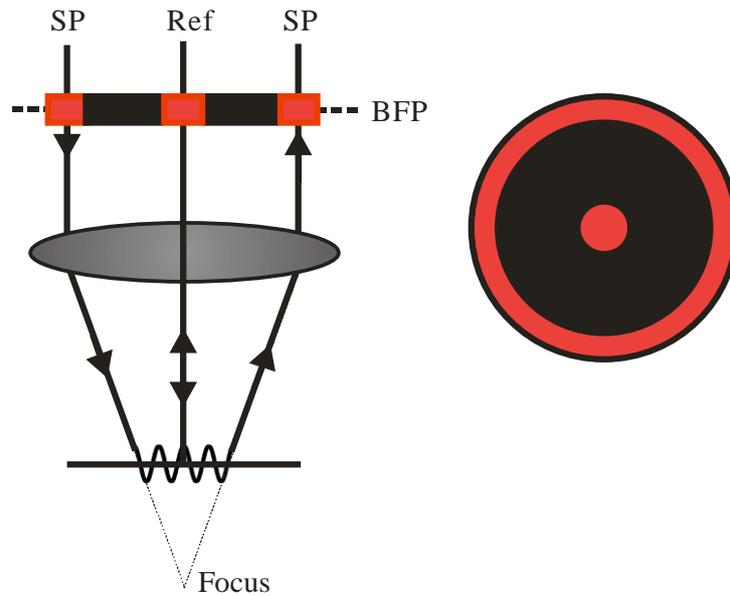
Fig. 4-9 optimizing the *V(z)* curves

It should be noted that no sharp edge should appear in any part of the pupil as other noisy ripples will appear. Based on this, I proposed another pupil function called Pup2, red curve in Fig. 4-10(a). By comparison the Pup1 (blue curves in Fig. 4-10(a)), it is clear that: 1) the new pupil function shares the smooth edge with the original one; 2) it blocks some useless background; 3) For the blocked part, it also shares smooth edge. By fulfilling the three points, the new pupil function provides higher contrast but the same advantage of reduced noisy ripples. In order to show how I blocked the background, 2D and 3D shapes of the new pupil function are shown in Fig. 4-10 (b) and (c). Simulated *V(z)* curves of gold and mirror by using two designed pupil functions are shown in Fig. 4-10 (d) and (e) respectively. It is obvious that the contrast is much higher using the new pupil function (red curves in Fig. 4-10 (d)).
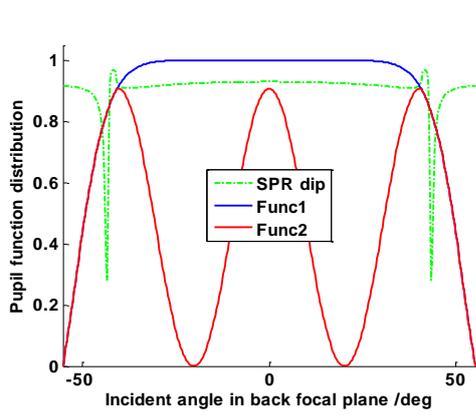
(a)
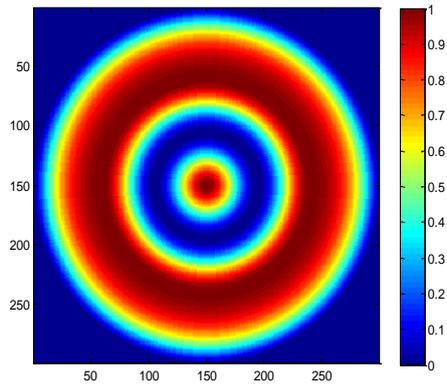


(b)
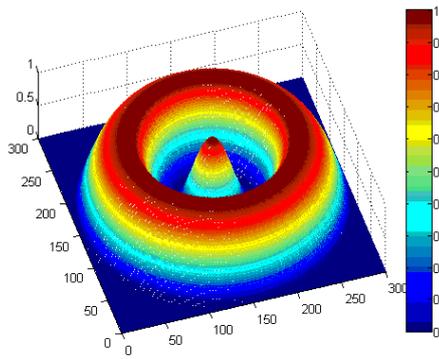


(c)
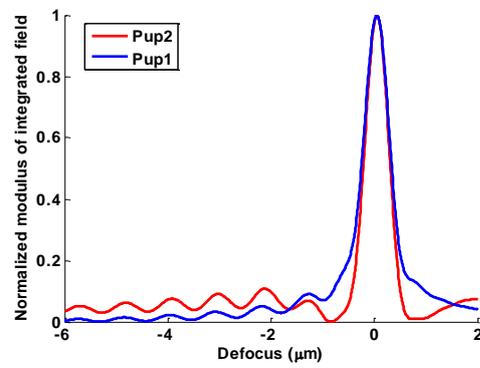


(d)
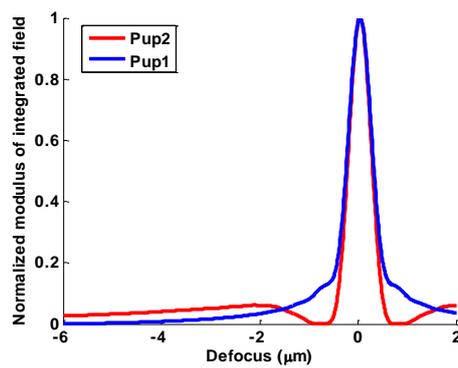


(e)

Fig. 4-10 Distribution of new pupil function and the simulated $V(z)$ curves.(a) 1D pupil function distribution; (b) 2D pupil function distribution; (c) 3D pupil function distribution; (d) $V(z)$ curves comparison between Pup1 and Pup2 when using a gold sample; (e) (d) $V(z)$ curves comparison between Pup1 and Pup2 when using a mirror.

102

### 4.3.4 Realization of pupil function modulation

The pattern from the SLM (Forth DD, SXGA-R5) was imaged onto the BFP of the objective to modulate the pupil function of the scanning system. SXGA-R5 is a fast switching, all digital, high resolution, and 24-bit native color depth reflective micro display. It is designed to control the reflected intensity distribution by varying the illumination time of the reflected light; this approach works well when viewing an intensity image. For this application, however, I need to interfere different portions of the light reflected from the sample so that all parts of the beam need to be on for the same time. I therefore use binary patterns on the SLM so that each region is either 'off' or 'on' and I effected the gray scale modulation of the pupil function by changing the density of 'on' pixels. For instance, for a region where a specific intensity is required I select pixels with a random number generator with a probability proportional to the weighting required for the pupil function in the desired region. In effect, I have used the fact that there are large numbers of pixels in the SLM (1280 by 1024) to replace temporal modulation with spatial modulation. Measurements can be repeated with different pupil functions to average out the randomness in the pupil functions, however, in practice, this was not found to be necessary.

### 4.3.5 Simulation results by using ForthDD ASLM

As I select the pixels of the ASLM randomly to generate the greyscale level, now I need to demonstrate that I can generate $V(z)$ by using this method. A simulation is done here to show it. I compare the responses between the 2D greyscale pattern and the 2D randomly select pixels with SLM. The BFP is shown in Fig. 4-11. Fig. 4-11 (a) is the BFP of the direct greyscale pattern and Fig. 4-11 (b) is that by using the randomly select pixels with the ForthDD SLM.
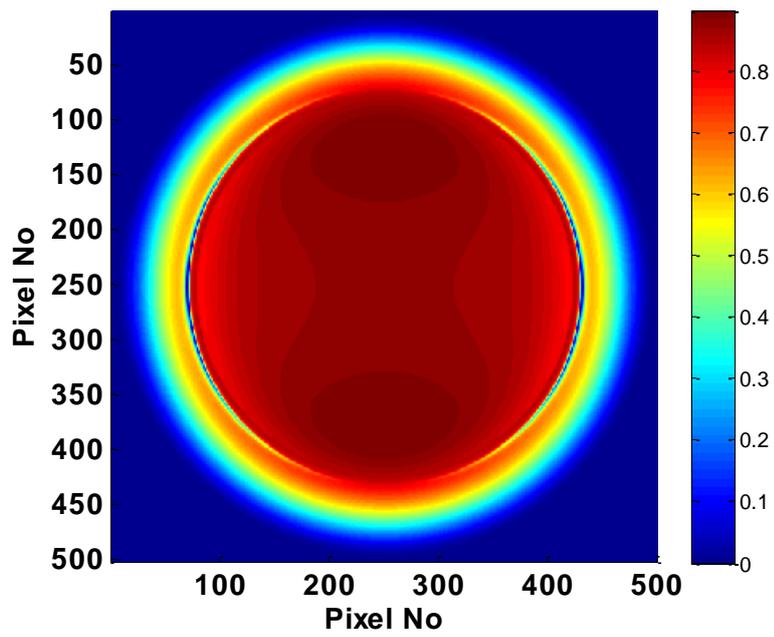
(a)
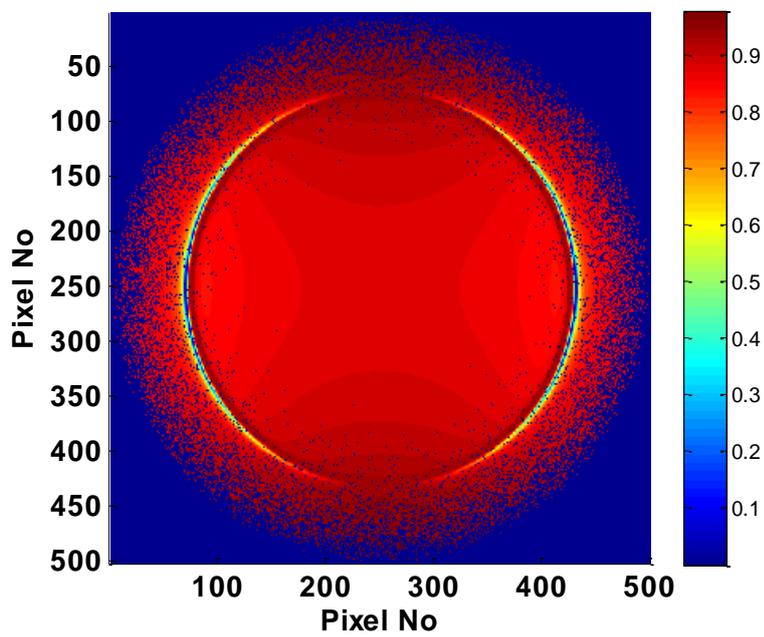


(b)

Fig. 4-11 (a) Ideal pupil function with plasmonic response superimposed; (b) Realization of pupil function with pixellated defects.

*V(z)* curves comparison is shown in Fig. 4-12. In order to clarify them, the field response of *V(z)* with ForthDD SLM is added by 0.1. The results demonstrate that I can use the ForthDD SLM to generate a greyscale pattern and modulate the BFP of the system.
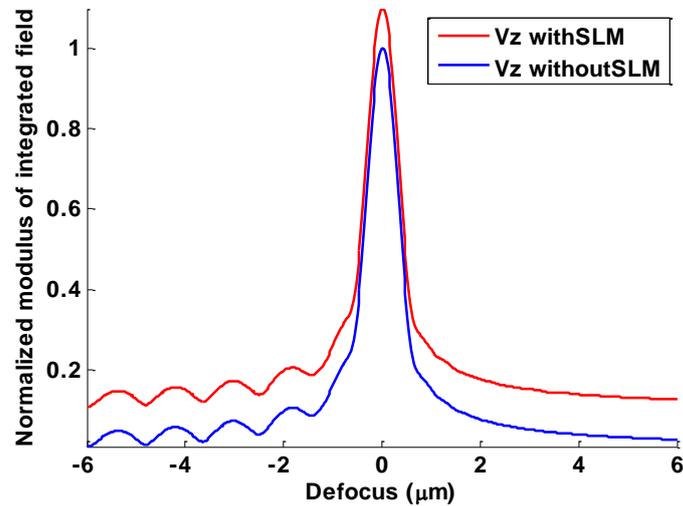


Fig. 4-12 Simulated *V(z)* comparison response with continuous distribution and pixellated distribution from ASLM

## 4.4 Methodology in confocal SPRM

### 4.4.1 Changes of *V(z)* periodicity and contrast mechanism of grating

I can obtain a *V(z)* curve by using the basic sandwiched sample structure (cover glass/Au/air). What will happen if any kind of dielectric is coated on the surface of gold? Fig. 4-13 shows the difference between the *V(z)* curves of uncoated and 20nm BSA (Bovine serum albumin, n=1.43) coated sample. The two *V(z)* curves provide different ripple period and the coated sample has shorter period.
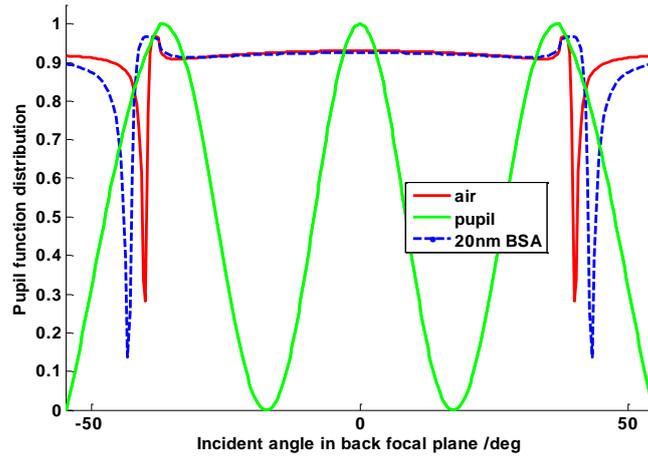
(a)
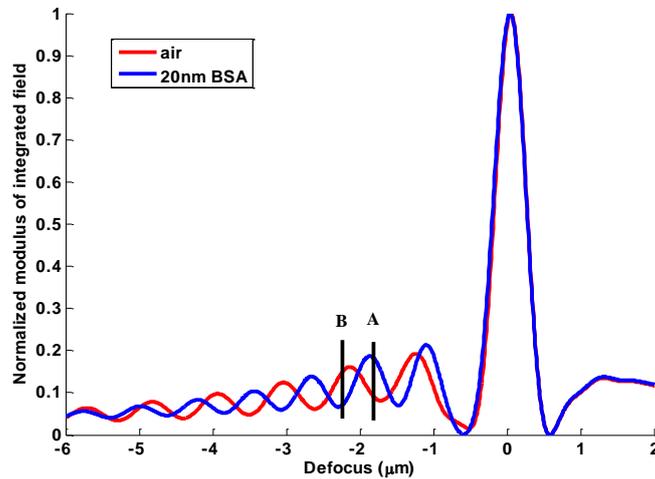


(b)

Fig. 4-13 (a) Pupil function distributions. The blue and red dashed curve shows the p-polarization reflection

coefficient with respect to the aperture of the microscope object using bare gold and 20nm BSA coated gold

respectively. This shows the SP dip relative to the objective aperture. The green curve shows the modified pupils

to optimize contrast and reduce oscillations due to hard cut off in the lens aperture. (b)$V(z)$ movement of coated

and uncoated samples regions explaining contrast mechanism and its reversal.

Fig. 4-14 shows a grating structure (20nm BSA/air). What will happen if I fix the defocus and

scan the x-direction. For example, if I fix the defocus at 'A' in Fig. 4-13, the BSA coated part

provides higher $V(z)$ and the uncoated part has lower response, the grating line scanning

image is like (b) in Fig. 4-14. If I fix the defocus distance at 'B' in Fig. 4-13, the $V(z)$

response of the coated and uncoated part will reverse, and the grating line scanning image will be like (c) in Fig. 4-14. This is the contrast mechanism of the confocal SPR microscopy.
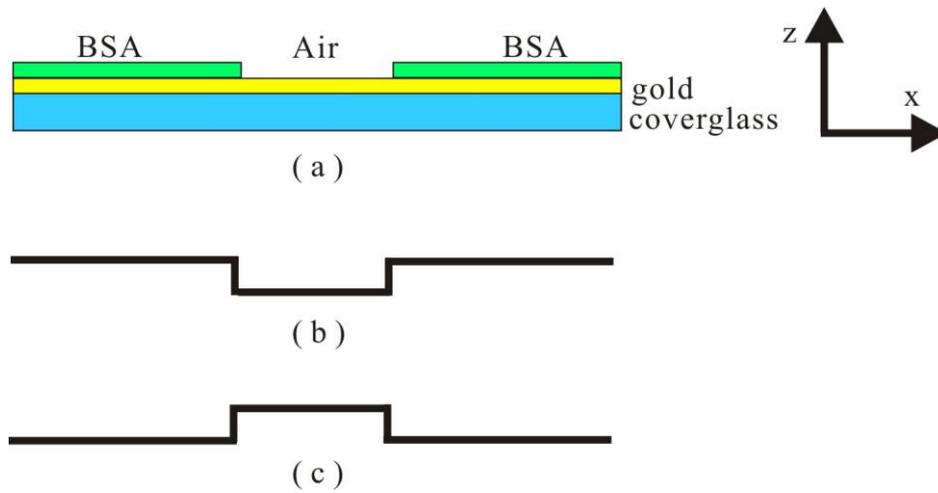


Fig. 4-14 (a) BSA grating structure; (b) theoretically grating image when using near defocus; (c) inverted theoretically grating image when using farther defocus;

## 4.4.2 Centre of gravity calculation in experimental data processing

In order to define the 'virtual' pinhole, I need to find the centre of the focal point. The easiest way is to define the brightest point. However, it is not practical in real experimental data processing. For example, an example image of focal point is shown in Fig. 4-15 (a). It is obvious that the brightest point is not the centre of the focal point. I need to consider another more reliable evaluation algorithm.



(a)
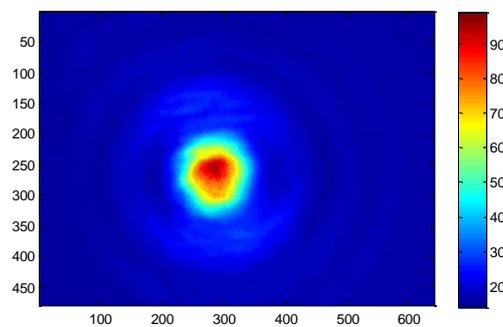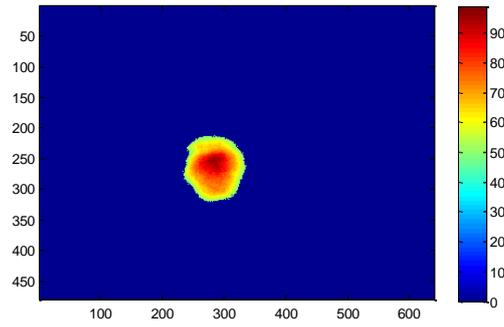
(b)

Fig. 4-15 An example of experimental focal point (worst case). (a) shows the focal point image; (b) shows the
image after cutting the surrounding.

I used the algorithm based on centre of gravity, which is also called centre of mass in physics.
It is necessary to mention that in actual data processing, I remove the blurred surrounding of
the focal point (Fig. 4-15 (b)) and then calculate the centre of gravity, in case that the blurred
surrounding is asymmetric. In the situation, the centre of gravity on the CCD can be
expressed as:

$$\bar{x} = \frac{\sum_{y} PixelVal \times x_i}{\sum x_i} \qquad \text{Eq. 4-11}$$

$$\bar{y} = \frac{\sum_{x} PixelVal \times y_i}{\sum y_i} \qquad \text{Eq. 4-12}$$

Where, PixelVal is the greyscale value of each pixel; $x_i$ is the horizontal position of each

pixel, from 1 to 640; $y_i$ is the vertical position of each pixel, from 1 to 480; $\bar{x}$ is the

horizontal position of the centre; $\bar{y}$ is the vertical position of the centre.

## 4.5 Experimental results

In this section, four aspects will be discussed: 1) BFP images modulated and un-modulated with the SLM; 2) effect of pinhole size; 3) $V(z)$ curves with modulation and without modulation; 4) grating line scan images.

### 4.5.1 BFP images obtained using Amplitude SLM

As mentioned in chapter 3, I used two cameras in the system. One is for the focal point image, another one is for the back focal plane. By detecting the back focal plane image, it shows how the modulation works and can analyze the sample from the position of SPR dip. Here, I will compare the difference from the point of BFP images, as shown in Fig. 4-16. (a) is the BFP image of the mirror without modulation; (b) is the plasmonic BFP image without modulation; (c) is the BFP image of the non-plasmonic with modulation by using the proposed Func 1 pupil function; (d) is that of the plasmonic case with modulation by using Func 1; (e) is that of the non-plasmonic case with modulation by using Func 2. It is worth mentioning that the BFP image in (e) is not as good as the others, because I did not block the cover of the system and background light were present when I grabbed this image.
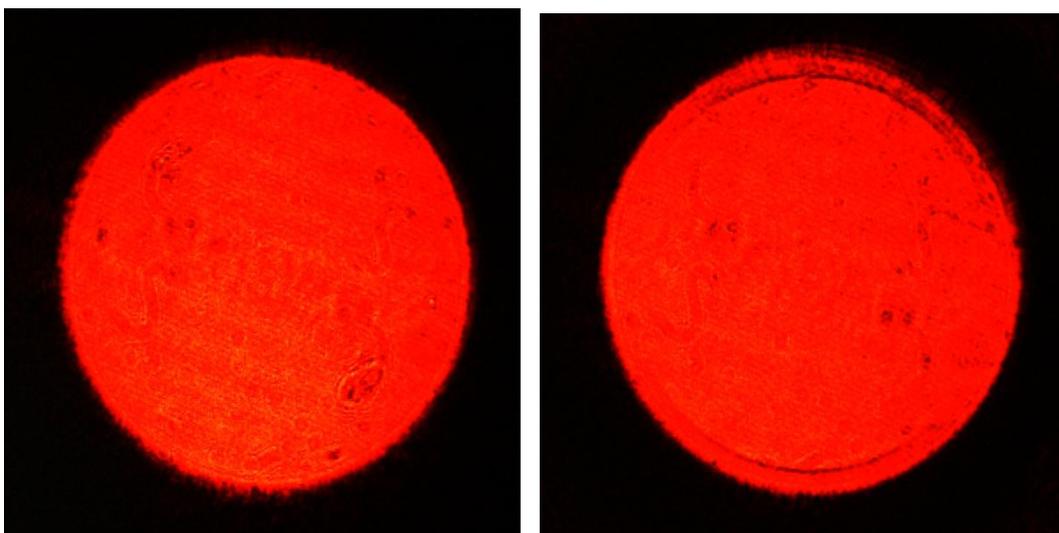


(a)                                                                 (b)
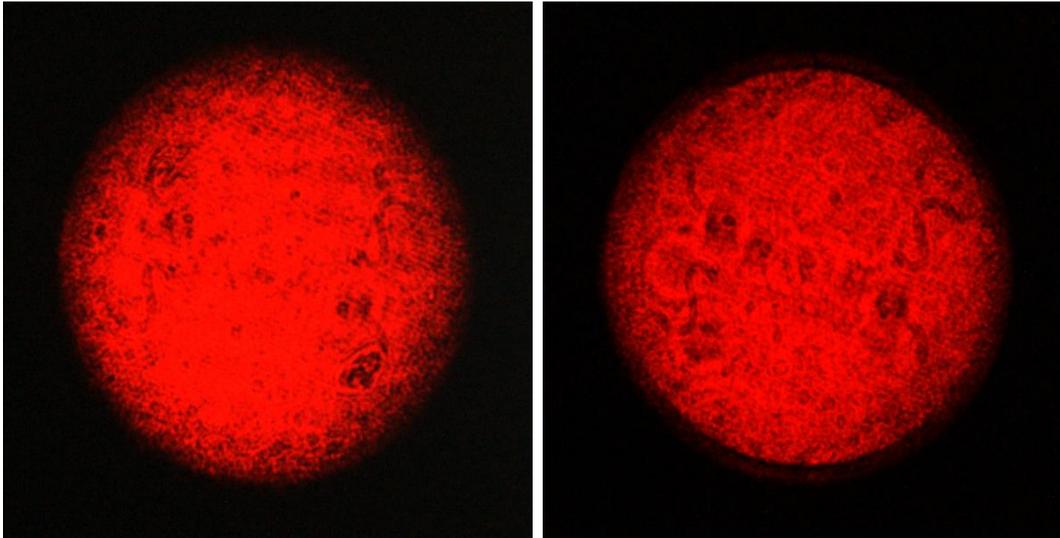
(c)                                                    (d)
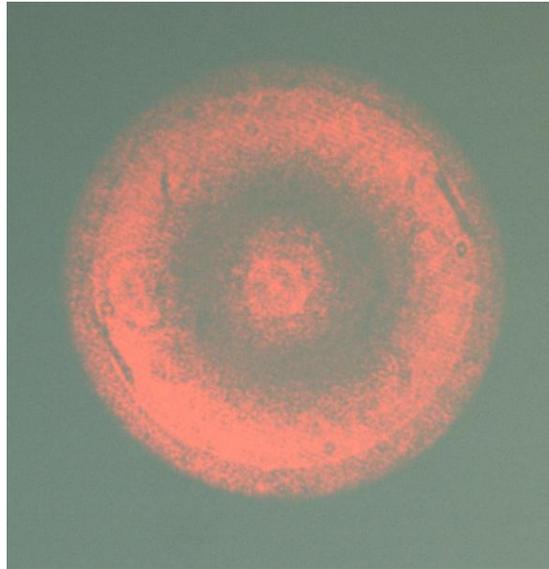


(e)

Fig. 4-16 Back focal plane images; (a) non-plasmonic without pupil function modulation; (b) plamonic without modulation; (c) non-plasmonic with modulation of Func 1; (d) plasnomic with modulation of Func 1; (e) non-plasmonic with modulation of Func 2

By comparing (a) and (b), it is obvious that the SPR dip exists in a plasmonic sample case, while no SPR dip in a non-plasmonic case. The SPR dip shows clearly that the SPR is excited. The BFP image in (c) shows clearly that the sharp edge in the original illumination was smoothed by using the proposed pupil function Func 1. The smooth edge then helps to

110

remove the noisy ripples in the *V(z)* curves. By now, I have demonstrated that: 1) SPR was excited in the experiment when using the three layer sandwiched sample structure; 2) the BFP was modulated as expected. It is also necessary to illustrate that the SPR is very weak by modulating the illumination, as shown in (d), however, I can still see clear ripples in the *V(z)* curve. This is one reason for the low contrast in this experiment. Two measures were proposed to overcome it: to enlarge the SPR signal; to reduce the useless background.

Firstly, in order to enlarge the SPR signal, I can locate the SPR dip position away from the edge of the aperture. If I fix the sample and just adjust the system, the only possible measure is to enlarge the objective NA. In the experiment in this chapter, I did not take this measure. After this experiment, in the following experiment, I used a 1.45NA objective from Zeiss. More details will be in next chapter. The second measure is to reduce the background. This is the reason I proposed the Func 2 pupil function. Experimental results are in the subsequent section.

## 4.5.2 Effect of *V(z)* with different pinhole radii

Fig. 4-17 shows experimental *V(z)* curves obtained from a coverslip that was coated with 50nm gold and 1nm chromium. The numbers in the legend (0.01, 0.1, 0.5 etc.) means the pinhole radii ratio to the Airy disc radius. For the large pinhole diameters the system has the same transfer function as a wide-field imaging system and the ripples are not observed, as can be seen in the simulations of Fig. 4-4, as shown by the violet curve (ratio = 1) and black curve (ratio =2) in Fig. 4-17. For very small pinhole diameters the SNR is very poor since little light is detected (blue curve of ratio 0.01), so a suitable compromise between satisfactory confocal response and good SNR is, for pinhole size between 0.1 and 0.5 of the Airy disc (red and green curves); These are similar to the values used in most conventional confocal imaging experiments. Fig. 4-17 demonstrates that the *V(z)* effect is periodic with a

period of 741nm by the FFT method close to the expected value of 752nm, however errors in film thickness and properties and also changes in the pupil function [3] account for this difference. A systematic error in absolute period does not prevent the measurement of very small changes, which is the primary purpose of most SP sensors. Fig. 4-17 also shows that the contrast is low as I expected in simulation. In the section above, I mentioned that this problem was mitigated by optimizing the pupil function and blocked some useless background. Experimental data will be shown in the section below.
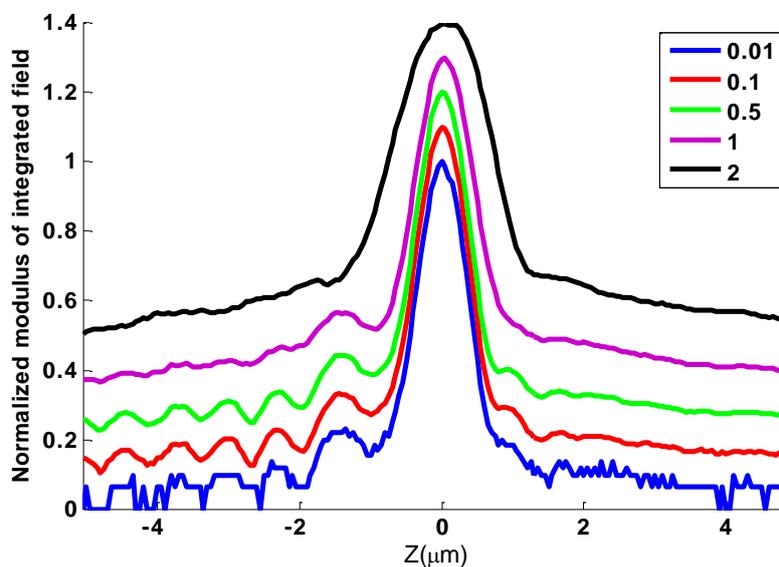


Fig. 4-17 Experimental *V(z)* curves on 50nm gold sample for different pinhole radii

## 4.5.3 Experimental *V(z)* curves

*V(z) curves without pupil function modulation*

In this section, I discuss the *V(z)* curves without pupil function modulation. For a confocal system, I have discussed that even if the sample is just a pure mirror (non-plasmonic sample), *V(z)* curve still presents some oscillatory behaviour which arises from the edges of the pupil function [7]. The experimental results (Fig. 4-18) show that the period is approximately 559 nm, and the strength of the signal is also about 15% of the amplitude response at the focal

plane, which means that when using uniform illumination, it is difficult to obtain a good quantification.
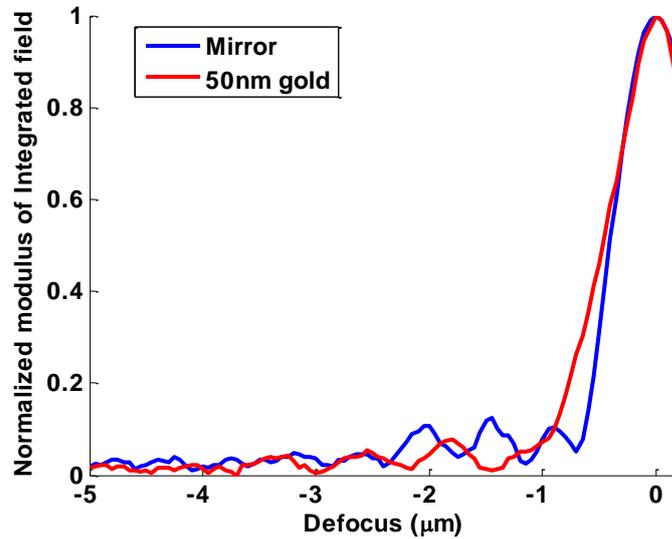


Fig. 4-18 *V(z)* curve of mirror and 50nm gold without pupil function modulation;

### *V(z) curves with pupil function modulation*

In the pupil function engineering section, I analyzed why I adopted pupil function and how to optimize the *V(z)* curve by blocking part of the useless background illumination.
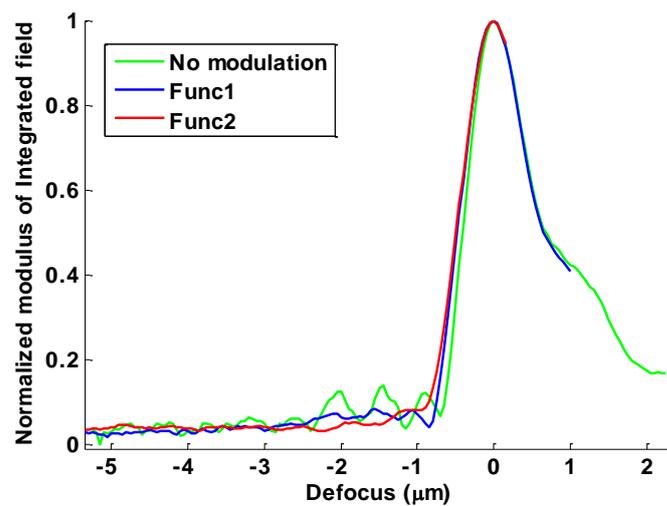


Fig. 4-19 *V(z)* curves comparison with no pupil function modulation, modulated pupil function 1, and optimized

modulated pupil function 2

According to the theory, both of the Function 1 and Function 2 should generate no ripples or quite low ripples when using a non-plasmonic sample, like a pure mirror. The experimental results are shown in Fig. 4-19. The green curve is *V(z)* without pupil function modulation, the blue curve is that of the firstly proposed pupil function, called Func 1. It can be seen that the useless ripples frequencies are removed. Then the experiment using the optimized pupil function, called Func 2, modulation was also operated, shown as 'red'. It can also be used to remove useless ripple frequency. By now, I have demonstrated that the two functions work well in the system and can be used to reduce the ripples due to the pupil function, see Fig. 4-19.

Then the plasmonic sample was applied, which consisted of coverglass (n=1.518, diameter 22mm, thickness 0.17-0.19mm), 50nm gold and air. 2 nm of chromium was also coated between the coverglass and the gold layer to help increase the adherence of the gold layer. The experimental results are shown below. It is obvious that, by using the Func1, I removed the noisy ripple frequencies and the *V(z)* curves just show the SPR (blue curve in Fig. 4-20), rather than a messy combination of noisy ripples and the signals (red curve in Fig. 4-20).
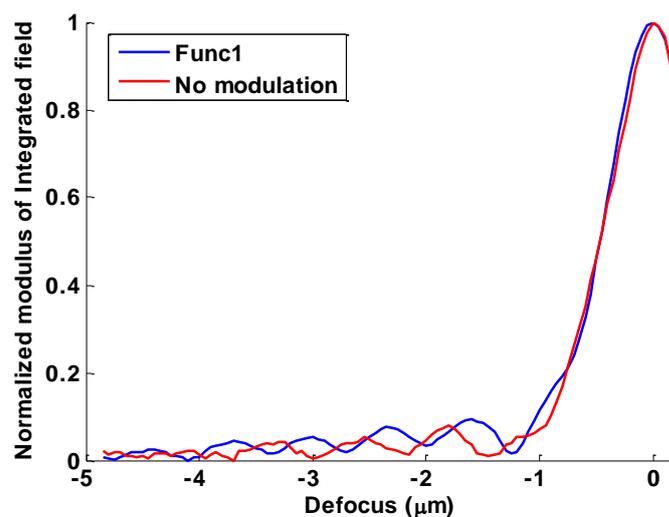


Fig. 4-20 *V(z)* curves of 50nm gold without modulation and by using Func1 pupil function

However, as expected, the signal contrast is quite poor. That is why I designed another pupil function, called Func 2. I have showed that Func 2 did not introduce new frequencies to the *V(z)* and did be able to remove the noisy ripples as shown in Fig. 4-19. Here, the experimental results of 50nm gold were shown in Fig. 4-21. The blue curve refers to the firstly proposed pupil function, Func1, while the red curve refers to the optimized pupil function, Func2. It is obvious that the contrast is enhanced by using Func 2 instead of Func1, as Func2 blocks the background signal in the angular range between normal incidence and the region where SPs are excited greatly improves the SP contrast.
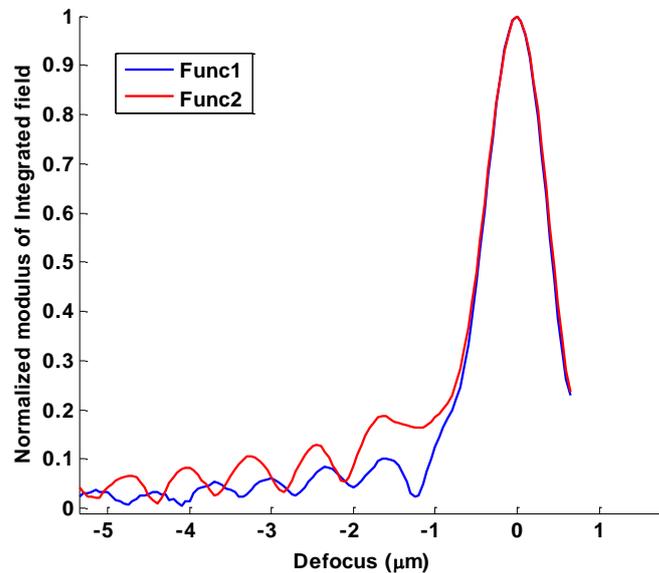


Fig. 4-21 *V(z)* curves of 50nm gold by Func1 and Func2 pupil functions

## 4.5.4 Grating image

In order to demonstrate that the technique can be used for spatially resolved measurements, a Bovine serum albumin (BSA) grating was imaged. Fig. 4-22 shows the 1D line traces of the BSA grating when the defocus distances are -1.25 μm (top left), -1.8 μm (top right) and at the focal plane (bottom left) respectively. It can be seen that the images at defocus -1.25 μm and at -1.8 μm are inverted, which can be easily explained by the bottom right figure, with

different defocus (say position A and B), *V(z)* values of coated and uncoated gratings are inverted. At the focal plane the grating contrast is extremely poor. It should be mentioned that at the focal plane, the intensity is much larger than the values when the sample is defocused. In order to get better contrast for the defocused values the light level was increased which saturated the signal at focus, which accounts for the saturation seen in Fig. 4-22 (d), of course, Fig. 4-22 (c) was taken at the lower power level where the focal distribution was unsaturated. Here I use the lateral resolution definition of the 10%-90% grating edge response proposed in [3, 14]. According to this definition, the lateral resolution shown in Fig. 4-22 is about 1.5 to 2 μm. Considering the sample I used in this experiment is relatively old and therefore the edge of the sample might not be sharp, the actual lateral resolution is expected to be better than the measured 1.5 μm.
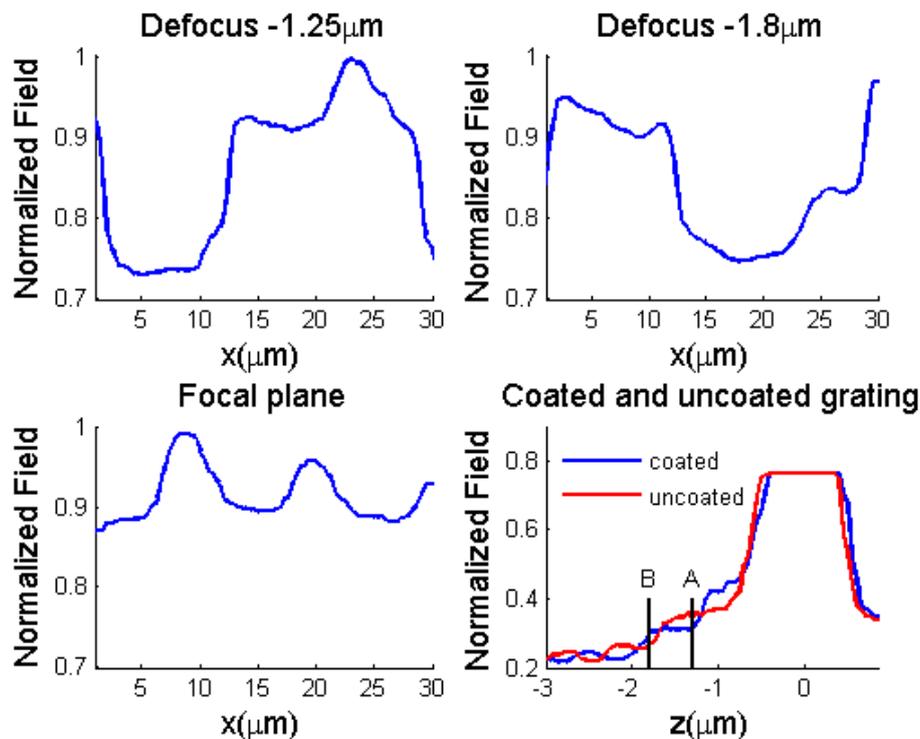


Fig. 4-22  One dimensional grating images with different defocuses. Bottom right shows *V(z)* curves on coated and

uncoated regions explaining contrast reversal

Fig. 4-23 shows the 1D images of the BSA grating when using different pinhole radii. It can be seen that contrast varies with the pinhole radius. When the pinhole radius ratio is 2, that is essentially, the conventional scanning microscope, the shape of the grating almost vanishes. With smaller pinhole radius, like 0.8, the grating shape can be recognized but with lower contrast; while the ratio shrinks to 0.1 or 0.01, the image can be obtained with better contrast. For the very small pinhole radius of 0.01 the SNR is poorer than 0.1 as expected although the values are still acceptable. We can see that confocal imaging gives greatly improved contrast and quantification.
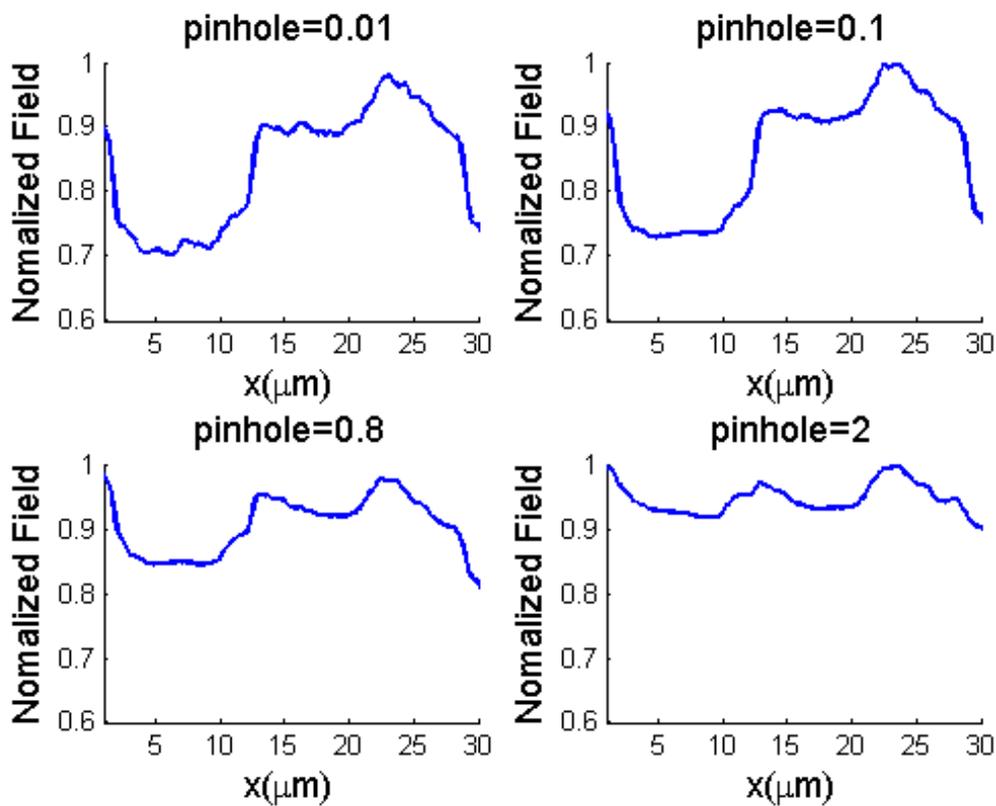


Fig. 4-23 One dimensional grating images at -1.25μm defocus using different pinhole radii

## 4.6 Conclusion and discussion

This experiment has demonstrated the feasibility of using a confocal arrangement to perform localized measurement of SP propagation. I have examined the effect of pinhole diameter and

also shown the effects of different illumination pupil functions. The method offers an alternative to interferometric SP imaging which is simpler and more stable, and perhaps the most significant advantage is that is can be incorporated into a conventional confocal microscope with minimal adaptation.

During this phase of the work, I found limitations of the technology and also some promising techniques by using the confocal SPR system.

1) Although I could use 1.25 NA objective lens to image the grating and I did get some results in the experiment; I also found that higher NA objective could be adopted to optimize the contrast;

2) I have shown that the amplitude modulation did work well in this project. However, there was a substantial background reflection from the amplitude SLM which reduced the contrast of the pattern. In the next two chapters, I will use a phase SLM to modulate the beam profile on the back focal plane.

# 5 Surface plasmon microscopic sensing with beam profile modulation

The purpose of the chapter is to implement an equivalent to the $V(z)$ method without mechanical scanning. In order to simulate the effect of defocusing, the amplitude SLM used in chapter 4 is replaced by a phase SLM. In this chapter, I will show how a phase spatial light modulator (i) performs the necessary pupil function apodization (ii) imposes an angular varying phase shift that effectively changes sample defocus without any mechanical movement and (iii) changes the relative phase of the surface plasmon and reference beam to provide signal enhancement not possible with previous configurations introduced in chapter 4.

## 5.1 Fundamentals of $V(\alpha)$

### 5.1.1 General introduction

In chapter 4, I used an amplitude only spatial light modulator (SLM) to apodize the illumination in the back focal plane, to ensure good quality oscillations. In this chapter I perform the same role with a phase only SLM, which also provides the phase variations necessary to obtain a plot equivalent to the $V(z)$ curve without mechanical movement, I call this $V(\alpha)$, for reasons that will become apparent later. A conceptual diagram of SP imaging in a confocal system is shown in Fig. 5-1(a).

The experimental system is similar to that used in chapter 4, except here a phase SLM (BNS $512 \times 512$ phase SLM) is used to replace the amplitude SLM; its function will be described at length in the chapter. The diagram is shown in Fig. 5-1(b). The phase SLM is applied to generate both the phase pattern and effective amplitude pattern and then is projected onto the back focal plane of the objective lens.
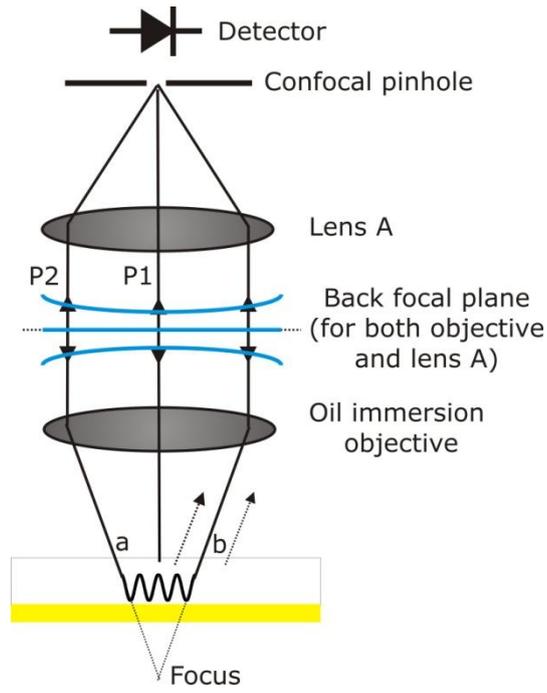
(a)
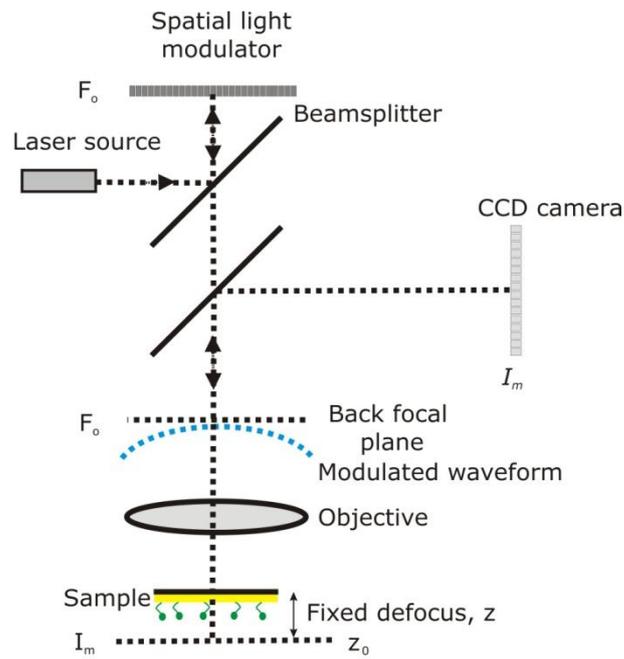


(b)

Fig. 5-1 (a) Simplified schematic showing operation of confocal microscope with SP excitation; (b) Schematic of optical system showing relationship between different planes in the system

## 5.1.2 From *V(z)* to *V(α)*

As mentioned in chapter 4, the output signal from a confocal microscope is a function of defocus, *z,* with a small pinhole (in practice a radius of ¼ the Airy disc diameter meets this condition) and linear input polarization into the back focal plane. Now consider the sample at a fixed axial position, $z_0$, which may include $z_0=0$, can I still get the periodic effect of effective *V(z)*? Let us think the basic concept of this chapter:
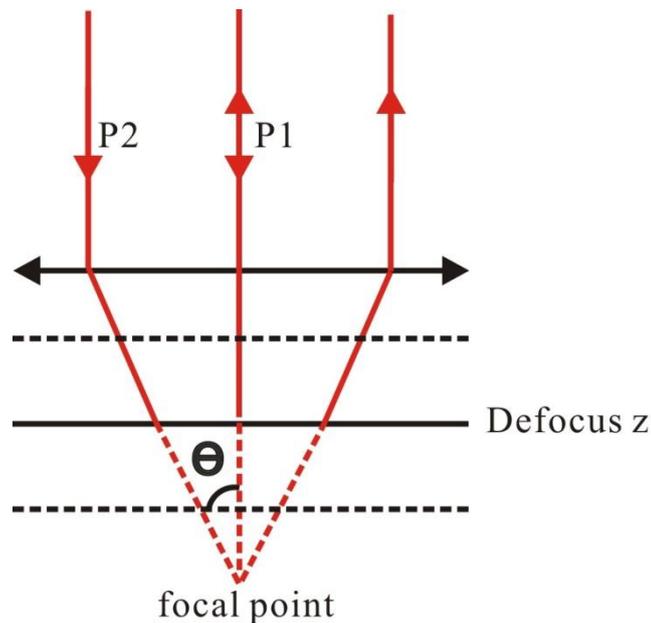


Fig. 5-2 basic idea of defocus z scanning

The phase difference between the reference 'P1' and signal 'P2' can be calculated by:

$$ph = \exp(j2nkz(1-\cos\theta)) \qquad \text{Eq. 5-1}$$

I note that the effect of defocus is to effectively change the phase profile of the incoming beam; this means that the SLM can be used to impose the same phase distribution that would usually be imposed by a mechanical defocus. In order to replicate the effect of defocus, I project a radially varying phase distribution onto the back focal plane of the objective. The

phase variation on the SLM, $\psi(s)$, is given by Eq.3 where $s$ again represents the sine of the incident angle which is proportional to the radial position in the back focal plane.

$$\psi(s) = \alpha\left(1 - \sqrt{1-s^2}\right) = \alpha\left(1-\cos\theta\right)$$    Eq. 5-2

gives an effective defocus

$$z_{eff} = z_0 + \frac{\alpha}{2nk}$$    Eq. 5-3

This means that varying the curvature on the SLM by varying $\alpha$ moves the defocus without mechanical scanning. In effect this is equivalent to incorporating the phase shifts associated with defocus into the input pupil function. Since the light only interacts with the SLM on the incident beam path so $P_{out}$ is unchanged.



(a)    (b)
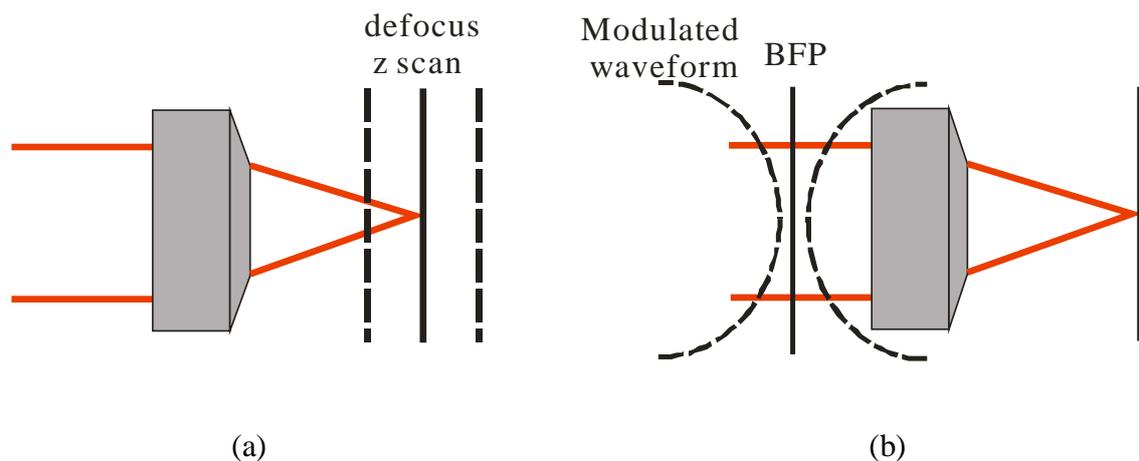
Fig. 5-3 from $V(z)$ to $V(\alpha)$; (a) the principle of $V(z)$ by mechanically scanning the defocus along axial direction; (b) the principle of $V(\alpha)$ by generating the phase pattern on the back focal plane

## 5.2 Simulation results

### 5.2.1 Is amplitude modulation necessary?

In the confocal surface plasmon experiment described in chapter 4, I introduced pupil function engineering which was necessary for the success of the experiment. In this

experiment, before I explain how to generate phase patterns for $V(\alpha)$, one question needs to be asked: do I need to modulate the amplitude? Simulations on both non-plasmonic case and plasmonic case are done as shown in (a) and (b) of Fig. 5-4 respectively. Simulated curve in (a) show that the sharp edge effect exists without the amplitude modulation (blue curve). The red curve in Fig. 5-4 (a) illustrates that the sharp edge effect can be removed with the amplitude pupil function modulation. The results matches with the $V(z)$ in chapter 4. For the plamonic sample simulation (blue curve) in Fig. 5-4 (b), it can be seen that although the SPR periodic effect is there, the curve shows an irregular feature as the existence of the sharp edge effect, while a regular periodic SPR $V(z)$ curve can be obtained with the amplitude pupil function modulation as the red curve shown in Fig. 5-4 (b). I can draw the conclusion that similar to the $V(z)$ technique in chapter 4, I still need the amplitude modulation in this $V(\alpha)$ experiment. In order to compare $V(\alpha)$ of plasmonic sample and non-plasmonic sample, the two curves are re-plotted in Fig. 5-4 (c), which show clearly that the periodic SPR $V(\alpha)$ effect only exists in the plasmonic sample .
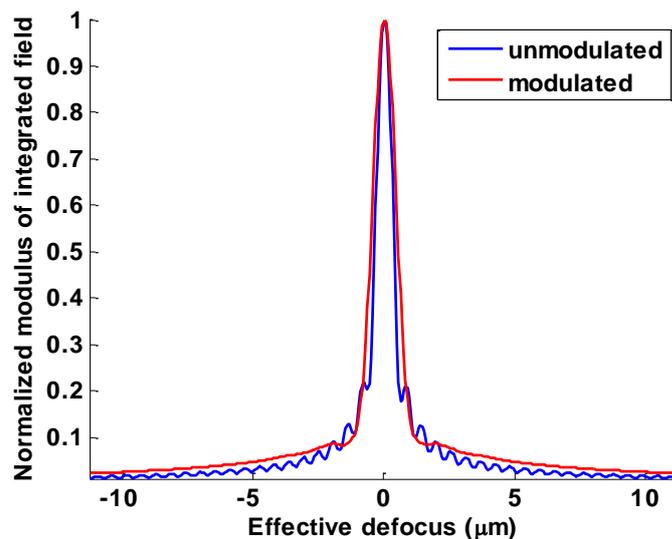


(a)
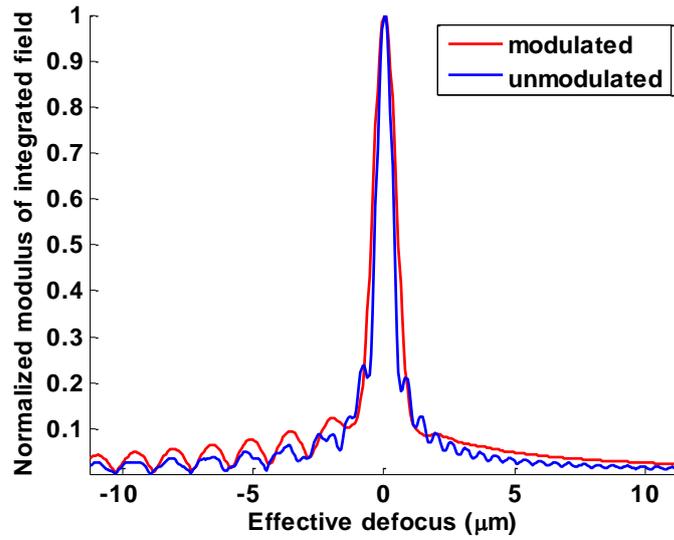
(b)
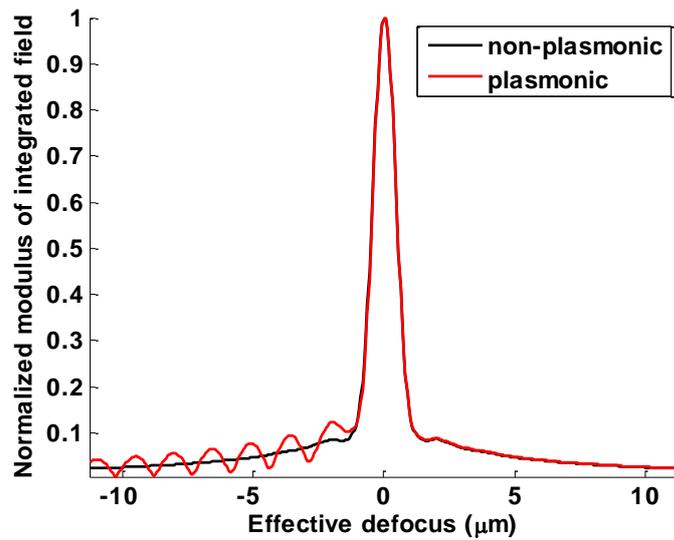


(c)

Fig. 5-4 Simulated $V(\alpha)$ results to show if the amplitude modulation still necessary. (a) Simulated $V(\alpha)$ comparison of a non-plasmonic sample with the amplitude modulation (red curve) and without the amplitude modulation (blue curve); (b) Simulated $V(\alpha)$ comparison of a plasmonic sample with the amplitude modulation (red curve) and without the amplitude modulation (blue curve); (c) re-plot curves of the plasmonic (red curve) and non-plasmonic sample (black curve) with the amplitude modulation

## 5.2.2 *V(α)* **movement**

Earlier in this chapter, I mentioned that the period of the *V(α)* curves varies with the coated

sample. Fig. 5-7 shows the movement of *V(α)* when using an uncoated sample and the 10nm

ITO coated sample. It shows clearly that the periods of the *V(α)* curves are different. This is

the image contrast mechanism distinguishing different materials in SP microscopy.
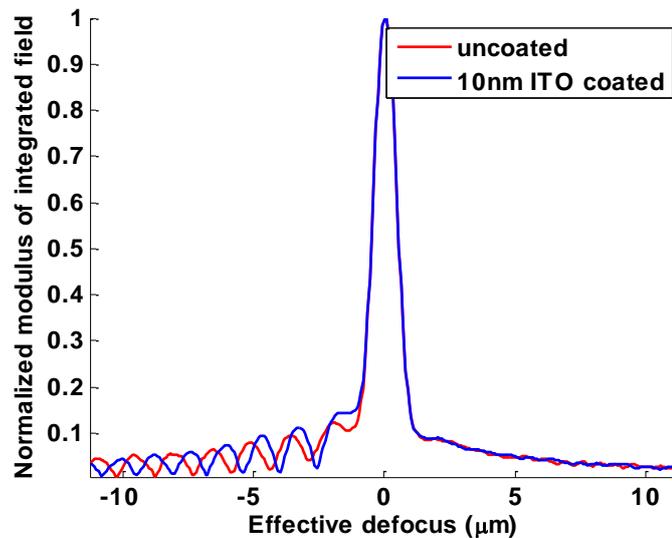


Fig. 5-5 Simulated *V(α)* curve movement when using the bare gold (red curve) and 10nm ITO coated sample (blue

curve)

## 5.2.3 Different defocus

In the introduction part, I mentioned that for this technique of *V(α)*, I can fix the defocus.

Then I need to ask which initial defocus I should fix. A simulation is done here to show the

influence of initial defocuses as Fig. 5-6. The simulated results show that the effective *V(α)*

curves move with the initial defocus, however, the shape and period of the curves do not

move, which means I can use any initial defocus in simulation. Later, I will show that

experimental results are similar to the simulated results in section 5.3.4.
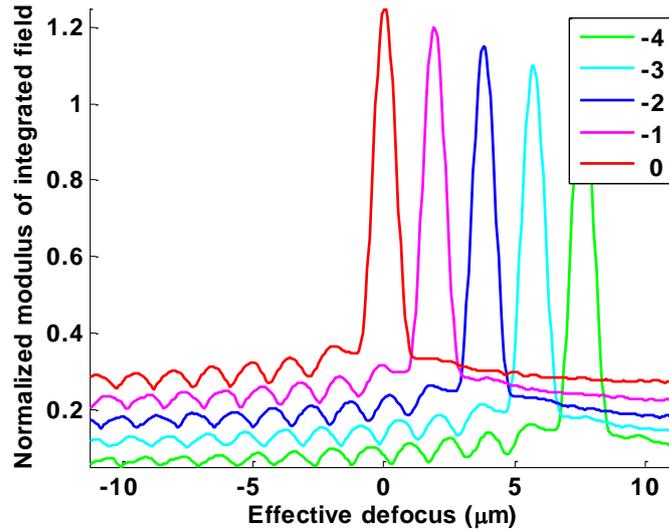
Fig. 5-6 Simulation $V(\alpha)$ results comparison on the effect of defocus. From the top red curve to the bottom green curve represent fixed physical defocuses of -4, -3, -2,-1 and 0 respectively. The curves are displaced along the y-axis by 0.1 units for clarity.

## 5.2.4 Amplitude modulation using a phase SLM

From the section 5.2.1, it can be see that I still need to modulate the amplitude in the technique of $V(\alpha)$ as well as the phase. That means I need to think about how to modulate an amplitude pattern by using a phase SLM. Details on how to modulate the amplitude using a phase SLM with the technique of phase cancellation can be found in chapter 3. However, I still need to ask a question: is the modulation of amplitude and that of the phase independent? That determines whether just one device can be used to modulate both the amplitude and the phase. Here, a simulation is presented to demonstrate that it is sensible. The red curve is the result of modulating the amplitude and phase separately and the blue curve shows the result of modulating both the amplitude and phase with one pure phase SLM. The simulated results demonstrate clearly that there is no difference between the two curves. That means I can use one pure phase SLM to modulate both the phase and amplitude simultaneously and independently.

126
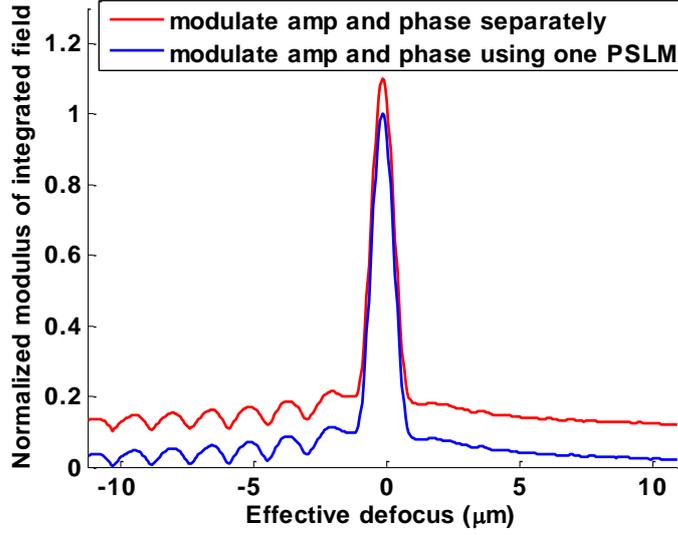
Fig. 5-7 Simulated results to show if amplitude modulation and the phase modulation independent; red curve is the result modulating the amplitude and phase separately and blue curve shows the result modulating both the amplitude and phase with one pure phase SLM. The red curve is displaced along the y-axis by 0.1 units for clarity.

## 5.2.5 Phase wrapping

For the BNS 512×512 phases SLM, the phase modulation range is (0 to 2.5π). However, in the experiment, I need a much larger phase modulation range, like -40π to 40π corresponding to [-11.24μm, 11.24μm], not to mention another [0 to π] for the effective amplitude pattern modulation. In order to solve this problem, I need wrap the actual phase into the range of [0, 2π]. I will not distinguish how much the phase of $V(\alpha)$ pattern is and how much the equivalent phase of the amplitude pattern is, because as long as the phase difference of two adjacent pixels is π, the intensity can be cancelled out to generate the designed amplitude pattern. The beam profile on the back focal plane can be expressed as:

$$A = A_{amp} \exp(j\psi_{phase}) \qquad \text{Eq. 5-4}$$

Secondly, I used the phase cancellation method to realize the amplitude modulation:

$$A = \exp(j\psi_{amp}) \bullet \exp(j\psi_{phase}) = \exp(j(\psi_{amp} + \psi_{phase})) = \exp(j(\psi_{tot})) \qquad \text{Eq. 5-5}$$

127

Where $\psi_{amp}$ is the phase necessary to obtain the amplitude pupil function modulation.

Then wrap the total phase by using the phase wrapping algorithm introduced above:

$$\psi_{tot} \Rightarrow \text{modulo}(2\pi) \qquad \text{Eq. 5-6}$$

It means that there is no difference on the $V(\alpha)$ curves with phase wrapping and without phase wrapping, therefore, I can use the BNS $512 \times 512$ phases SLM to generate the equivalent amplitude pattern and the required $V(\alpha)$ patterns in the experiment. Experimental results will be shown later in section 5.3 of this chapter.

## 5.2.6 Phase shifting

For the PSLM based system, I could change the relative phase of the surface plasmon and reference beam to provide signal enhancement not possible with previous configurations in chapter 4. Fig. 5-8 demonstrates the principles and the simulation results. I can change both the phase of the plasmon or the reference to change their relative phase. In this chapter, I select to rotate the reference beam ('R' in Fig. 5-8(a)) by 90º, 180º and 270º to see if the ripples on the $V(\alpha)$ curve move as expected.
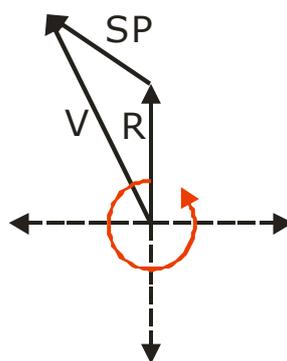


(a)
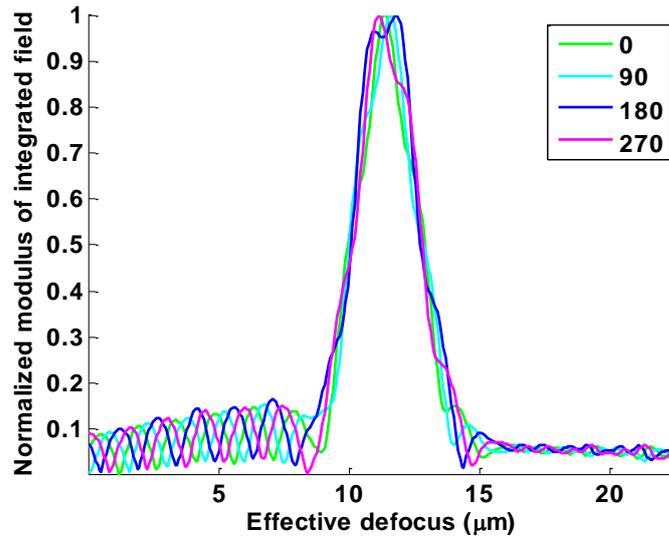
(b)

Fig. 5-8 (a) Diagram of phase shifting; (b) Changes in *V(α)* periodicity when shifting the phase 90 degrees each

time; the four colours represent the curves of 0°, 90°, 180°, 270° respectively.

A simulation (Fig. 5-8 (b)) is operated here to show the changes in $V(\alpha)$ periodicity when

shifting the phase of reference beam 90 degrees each time. The curves demonstrate clearly

that the ripples move when rotating the reference.

## 5.2.7 Generating patterns

This section shows how to generate the patterns required. It includes five steps: 1) generate

pure phase patterns for *V(α)*; 2) generate phase cancellation patterns for amplitude

modulation; 3) add the two patterns generated in the first two steps; 4) wrap the patterns of

the third step; 5) change the generated wrapped phase patterns to be the greyscale levels bmp

files by using the function of the phase SLM I fitted.

The whole steps were showed in Fig. 5-9. (a) is a 1D plot of generated V($\alpha$) patterns; (b) is

the wrapped 1D image of (a);  (c) is the 2D of generated V($\alpha$) patterns; (d) is the wrapped 2D

of (c); (e) shows the generated 2D total (amplitude +phase) patterns; (f) shows the wrapped

patterns of (e); (g) shows the whole patterns; (h) shows the generated grey scale level bmp files.
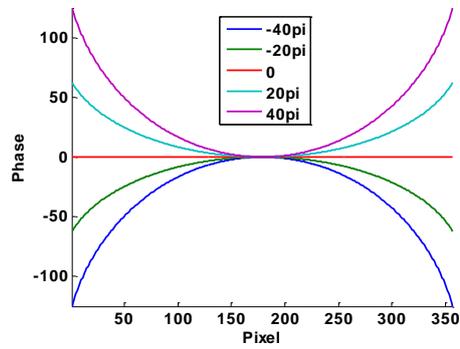


(a)
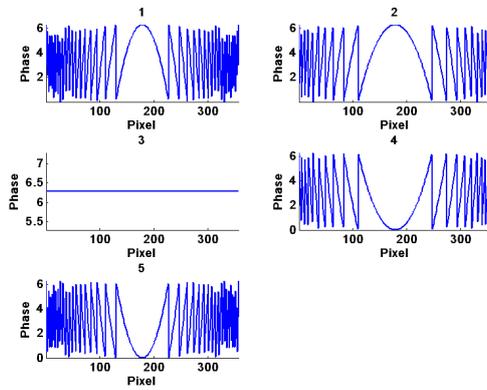


(b)
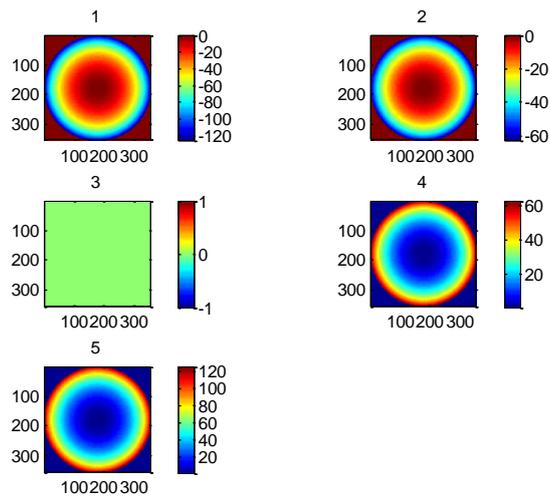


(c)
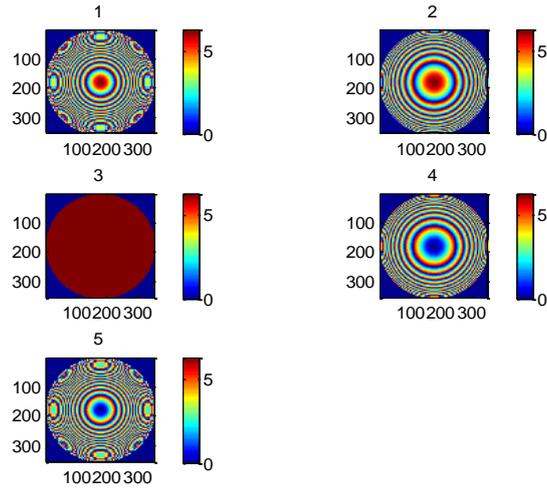
(d)
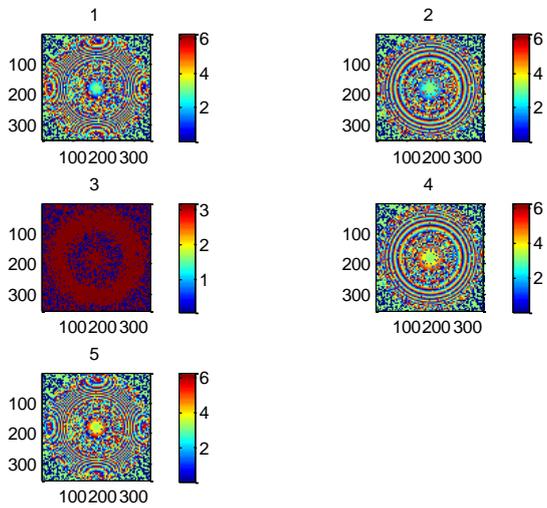


(e)
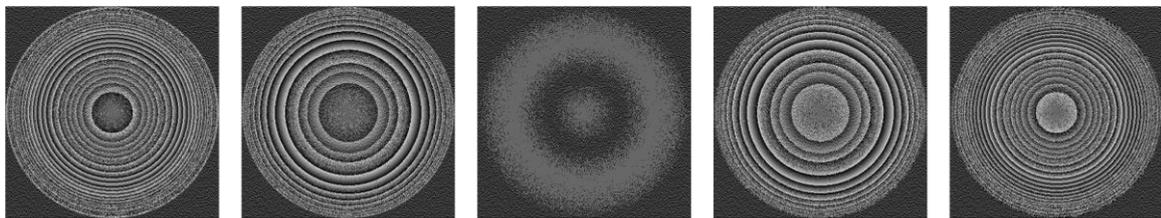


(f1)  (f2)  (f3)  (f4)  (f5)

(f)

Fig. 5-9 A selection of 2D pattern I use to generate V($\alpha$); (a) 1D of generated V($\alpha$) patterns; (b) Wrapped 1d of

generated V($\alpha$) patterns; (c) 2D of generated V($\alpha$) patterns; (d) Wrapped 2D of generated V($\alpha$) patterns; (e)

Wrapped 2D of generated total (Amplitude +phase) patterns; (f) Generated grey bmp files sent to SLM

## 5.3 Experimental results

### 5.3.1 Can I use a pure phase SLM to generate amplitude pattern?

Fig. 5-10 shows the back focal plane images. (a) is the un-modulated BFP image when using uncoated gold; (b) is the modulated BFP image when using uncoated gold; (c) is the un-modulated BFP image when using 10nm ITO coated gold; (d) is the modulated BFP image when using 10nm ITO coated gold. Comparing (a) and (b), I can demonstrate the phase cancellation method by using a phase SLM to modulate amplitude works. (c) and (d) also demonstrate it. Comparing (a) and (c), or (b) and (d), I should be able to see the difference between coated sample and uncoated sample, however, the difference is not so clear because of the thickness of the ITO layer is too low.

(a)

(b)

(c)

(d)
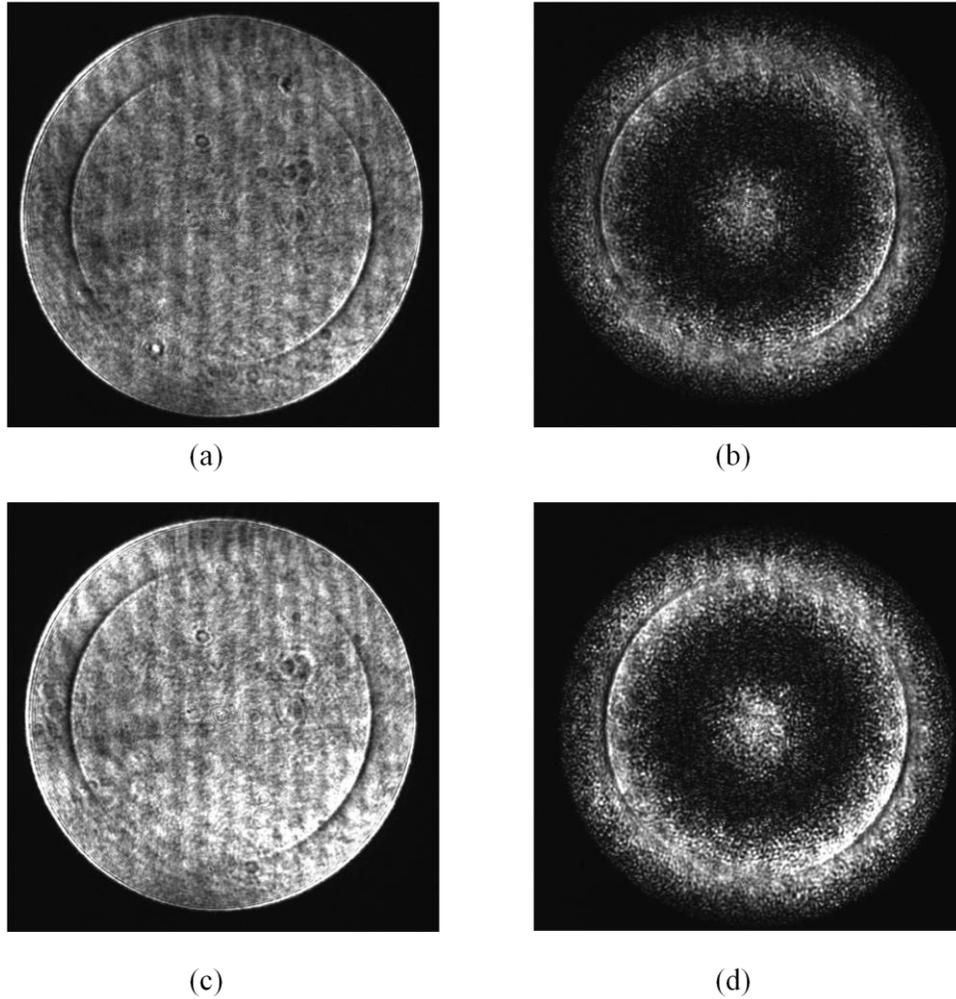
Fig. 5-10 Back focal plane (BFP) images using a phase SLM to effectively modulate the amplitude; (a) is the un-modulated BFP image when using uncoated gold; (b) is the modulated BFP image when using uncoated gold; (c) is the un-modulated BFP image when using 10nm ITO coated gold; (d) is the modulated BFP image when using 10nm ITO coated gold.

## 5.3.2 Generating an apodized pupil function

In this subsection I consider the $V(z)$ curve generated by scanning the axial defocus. In reference [5] I showed that amplitude apodization was necessary since a sharp edge to the pupil function introduces phase and amplitude fluctuations in the response which are unrelated to SP propagation. Moreover, it is also useful to attenuate light incident at angles intermediate between normal incidence and angles close $\theta_p$ as these angles do not contribute to the desired signal, so the relative amplitude of the plasmonic contribution is increased

when these angles are eliminated. The angles close to normal incidence correspond to path P1 and those at higher angles correspond to path P2 of Fig. 1-2.
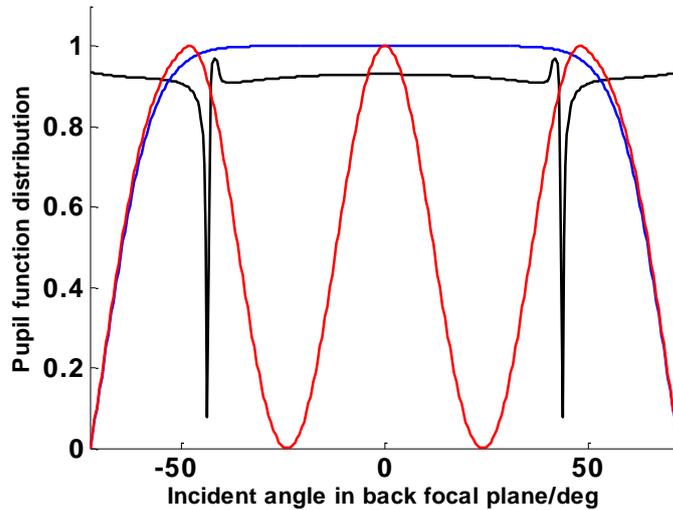


(a)
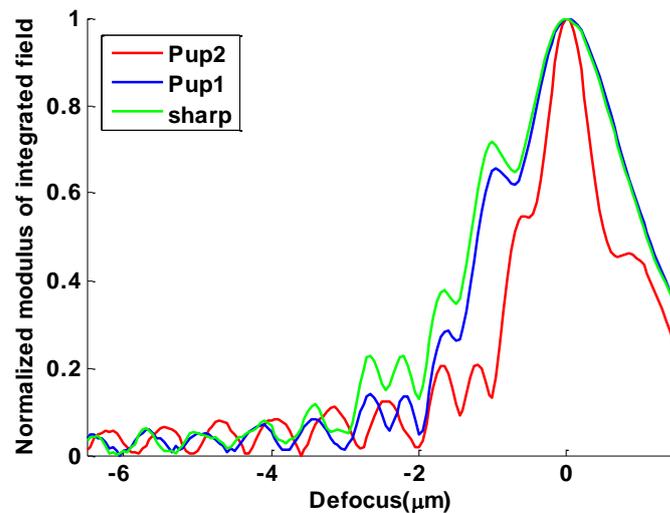


(b)

Fig. 5-11 (a) Pupil function distribution, red curve and blue curve are the pupil functions used in the experiment, the black curve show the calculated reflection coefficient for *p*-incident polarization on an uncoated sample. Note the blue curve overlaps the red for large incident angles; (c) *V(z)* curves obtained using different pupil functions (green curve was produced by a pupil function which was constant over the whole aperture, the red and blue curves correspond to the pupils of the same color in (a).

In chapter 4, I used binary modulation to generate desired amplitude of the pupil function by changing the density of 'on' and 'off' pixels in direct proportion to the required strength of the pupil function in the measurement region. This was performed using a random number generator and selecting an on pixel with probability proportional to the local amplitude. Since I am restricted here to using a phase only modulator I simply used a 2 by 2 block of pixels as a 'super pixel' and selected these units in the same way as done previously where an 'on' group of pixels would be in phase, whereas and 'off' pair would have two pixels in phase and two in antiphase (many other possibilities are also possible). I chose to use a 2 by 2 block rather than a pair of pixels simply to maintain the symmetrical shape along two axes. In addition to modulating the amplitude this procedure also allows to have a local phase since the pixels constituting an 'on' pixel only need to be in phase and their actual phase can be controlled independently. This point is crucial in the sections that follow. Fig. 5-11(c) shows $V(z)$ curves obtained with different pupil functions, where I see that the hard edged pupil (green) has a less well defined period and the defocus is greater than 3 microns before the ripples due to the SPs dominate; this compares to about 2 microns for the other cases.

### 5.3.3 $V(\alpha)$ curves: defocusing without scanning

Fig. 5-12 shows a comparison between a $V(z)$ curve and a $V(\alpha)$ curve taken on the same sample. The values of $\alpha$ have been obtained from the phase profile on the SLM using Eq. (3). No mechanical scanning was used to obtain the $V(\alpha)$ curves. I note in both curves that there is region of rapid oscillation equivalent to a defocus between approximately -1 and -2 microns this is due to aberration in the objective possibly due to some surface damage, however, beyond -2 microns there is a clear oscillation due to the presence of the SPs which show equivalent behaviour and predict a value of $\theta_p$ =43.5 degrees.
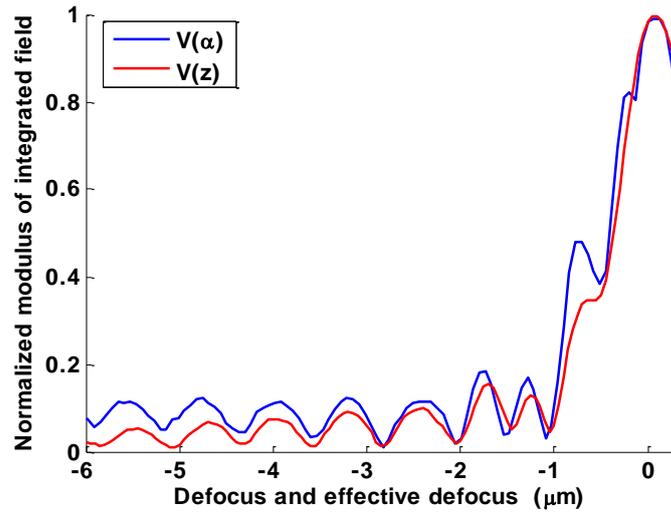
Fig. 5-12 Comparison between $V(z)$ and $V(z_{eff})$, the red line refers to the real $V(z)$ curve and blue line refers to the effective $V(z)$ calculated from $V(\alpha)$

Fig. 5-13 shows a comparison between $V(z_{eff})$ curves obtained on a gold sample and gold layer coated with a thin layer of ITO, We can see that ripples associated with the coated region have a shorter period compared to the uncoated region (0.714 $\mu m$ compared to 0.739 $\mu m$), corresponding to plasmonic angles of 44.93º and 43.48º respectively. The difference in $\theta_p$ obtained between the coated and uncoated region is attributed to layer of ITO of thickness 7.8 nm, which is close to the value set in the deposition process.
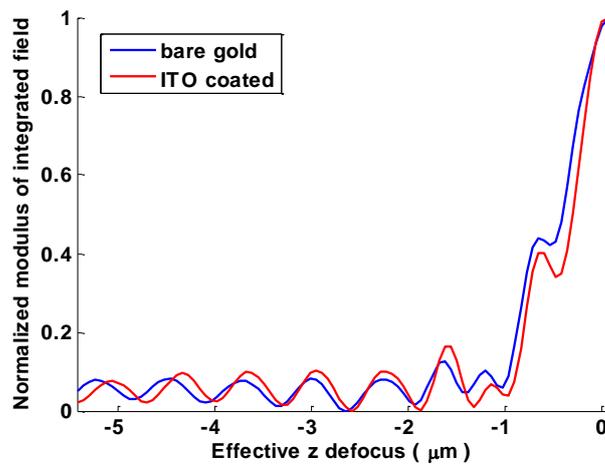


Fig. 5-13 $V(\alpha)$ comparison between uncoated and ITO coated sample, the red line is the ITO coated case and blue line is the uncoated case;

136

## 5.3.4 Changing the offset defocus

Equation 5-2 shows that the effects of the physical defocus and defocus imposed by the SLM are additive. This effect is borne out in Fig. 5-14 which shows how the curves are displaced as the physical defocus is changed. For instance, in the case of the green curve there is a physical defocus of -2 microns so an equal and opposite effective defocus from the SLM is required. The interesting feature is that although the periodicity of the ripples is essentially unchanged the quality of curves is actually better when the physical defocus is small. This is somewhat counterintuitive since large defocuses mean the additional curvature imposed by the SLM is small. Moreover, with two defocus mechanisms the system appears very sensitive to sample tilt. Since the quality of the oscillations is not noticeably degraded when there are large numbers of phase wraps on the SLM pattern the experiments were performed with little or no physical defocus.
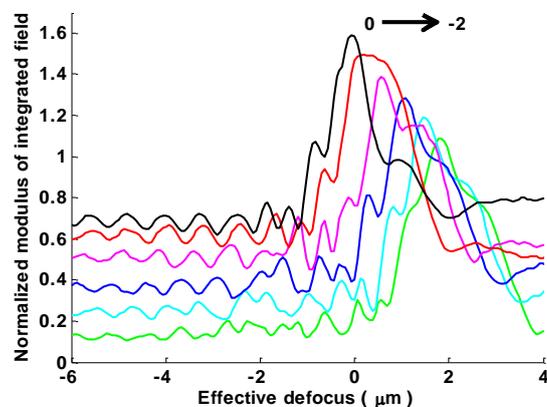


Fig. 5-14 *V(α)* curves obtained with different amounts of physical defocus . The black line to the bottom green line, represent fixed physical defocuses of 0, -0.4, -0.8, -1.2, -1.6, -2 respectively. The curves are displaced along the *y*-axis by 0.2 units for clarity. Line order black (solid), red(dashed), magenta (dotted), blue (solid), cyan (dash), green (dotted).

## 5.3.5 Additional phase shifting of the reference beam

Since the phase SLM performs all the functions necessary in the signal processing I can simply modify the expression for $\psi(s)$ so that I add an additional phase shift, $\beta$, below incident angles corresponding to $\sin^{-1}(s_1)$.

$$\psi(s) = \begin{cases} \alpha\left(1-\sqrt{1-s^2}\right) + \beta, & \text{for } s < s_1 \\ \alpha\left(1-\sqrt{1-s^2}\right), & \text{for } s \geq s_1 \end{cases}$$

Eq. 5-7

where s again represents the sine of the incident angle which is proportional to the radial position in the back focal plane.
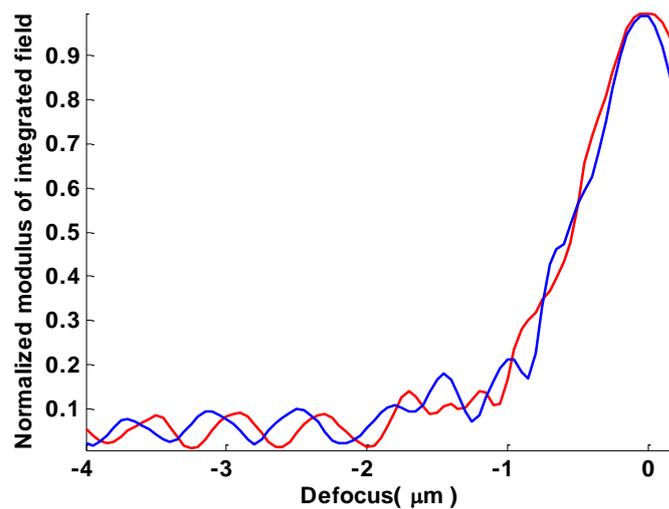


Fig. 5-15 $V(\alpha)$ curves obtained with two different phase shifts of the reference, red curve refers to the non-phase shifting case and the blue line refers to the case with shifting $90^\circ$ on the reference beam;

## 5.3.6 Misalignment of the phase SLM

Fig. 5-16 shows the effect of moving the phase SLM from the optimal position. We can see that the period of the ripples does not change significantly but even a very small displacement of 1% of the radius of the aperture in the back focal plane degrades the number of observable ripples dramatically, clearly this phase error is exacerbated for large curvatures. When the

SLM is displaced by 2% of the aperture radius the interference between reference and SPs is barely visible at any defocus.
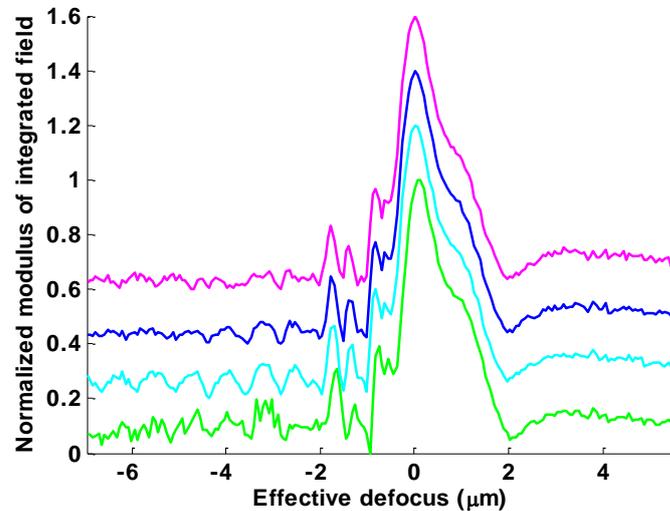


Fig. 5-16 The effect of SLM misalignment on the quality of the $V(\alpha)$ curves. The SLM was misaligned by -0.01, 0, 0.01, 0.02 units of the back focal plane aperture from the lower green line to the upper magenta line. The curves are displaced along the $y$-axis by 0.2 units for clarity.

## 5.4 Conclusion

This chapter has shown how a phase SLM can greatly extend the utility of confocal based SP sensing and imaging. A crucial feature in SP imaging is that contrast changes and quantification of the SP $k$-vector can be obtained by axially scanning of the sample. This chapter shows that this may be achieved functionally by simply altering the phase profile of the SLM. This removes the need for precision mechanical components and is inherently more stable and also potentially quicker.

I also show preliminary results that demonstrate that further processing of the response may be obtained by changing the phase between the reference beam (P1 in Fig. 1) and the SP beam (P2 in Fig. 1), this provides an additional contrast mechanism.

# 6 Quantitative plasmonic measurements using embedded phase stepping confocal interferometry

In this chapter, I will introduce quantitative plasmonic measurements of the phase velocity and the propagation length by extending the interferometer concept to produce an 'embedded' phase shifting interferometer, where I can control the phase between the reference and surface plasmon beams with a spatial light modulator. I demonstrate that this approach facilitates extraction of the amplitude and phase of the surface plasmon to measure of the phase velocity and the attenuation of the surface plasmon with greatly improved signal to noise compared to previous measurement approaches[1]. I also show that reliable results are obtained over smaller axial scan ranges giving potentially superior lateral resolution.

## 6.1 Introduction

In chapter 4, I demonstrated how a modified confocal microscope which used only the amplitude of the confocal signal gave considerable advantage compared to the output from a non-confocal system. Then in chapter 5, I introduced a phase SLM into the system and showed that I could move the ripples on the curves when imposing phase shifting between the reference beam and the surface plasmon. In this chapter, I will use the same hardware configuration as that used in chapter 5. I will demonstrate that compared to the amplitude only measurement in chapter 4, phase measurement gives much better performance in terms of immunity to noise and lateral resolution. This measurement can be achieved using the spatial light modulator which allows us to configure the confocal instrument as an 'embedded' phase stepping interferometer. I show that the system forms a phase stepping interferometer

between the paths P1 and P2 of Fig. 6-1(a). Data extraction from the system allows the amplitude and phase corresponding to the SP excitation to be extracted directly. This allows both the real and imaginary parts of the SP k-vector to be extracted which can, of course, be equated to the phase velocity and attenuation of the SP.
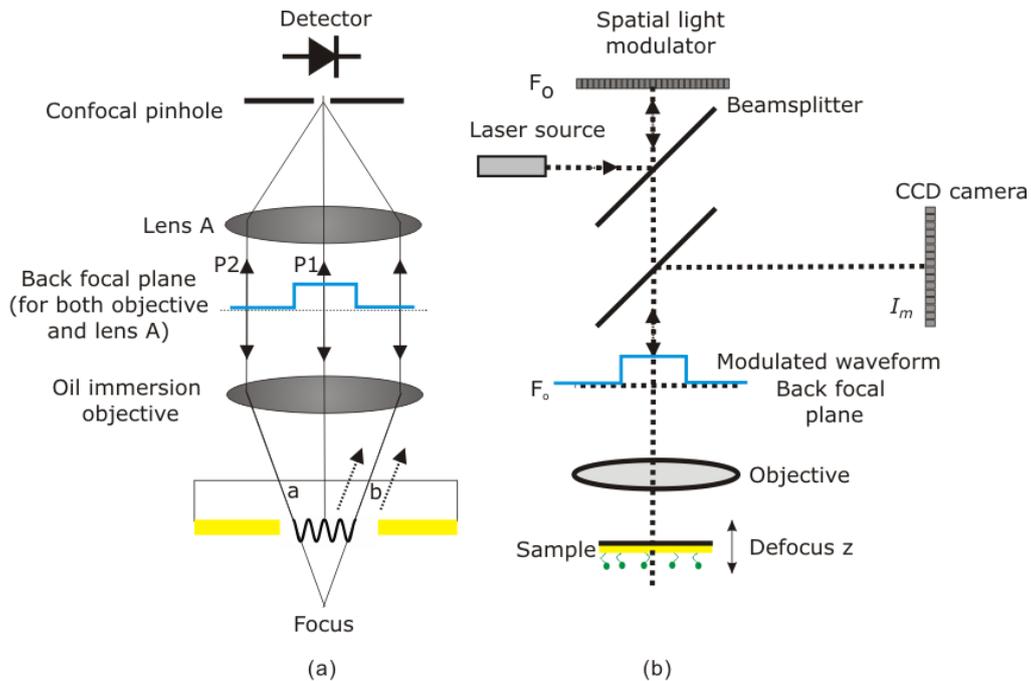


Fig. 6-1 (a) Simplified schematic showing operation of confocal microscope with SP excitation; (b) Schematic of optical system showing relationship between different planes in the system. The blue waveform indicates phase modulation in the back focal plane.

## 6.2 Phase-stepping technique

### 6.2.1 General phase stepping interferometry

Interferometry is an excellent method for high precision quantitative measurement and phase can be used for surface profiling, however, the phase information is encoded within fringe patterns, thus, algorithms that can extract the phase information from the fringe pattern are necessary. Phase stepping is one of the techniques which can be used for fringe analysis. It can provide higher precision compared to other techniques, such as Fourier transform[88],

and usually needs at least three interferograms to extract the phase information from the fringes. Here, I adopt the phase stepping technique to extract the amplitude and phase information of SPs. The experiment results have demonstrated that this technique is effective.

The basic equation for two beam interference is

$$I = DC + AC\cos(\phi)$$ 

Eq. 6-1

The four-step algorithm is one of the most common methods used for the optical wave front reconstruction. According to the four-step phase stepping algorithm, I require four interferograms with a phase difference of $\frac{\pi}{2}$ to reconstruct the sample image. Four equations are as follows:

$$
\begin{aligned}
I_0 &= DC + AC\cos(\phi) \\
I_1 &= DC + AC\cos(\phi + \frac{\pi}{2}) \\
I_2 &= DC + AC\cos(\phi + \pi) \\
I_3 &= DC + AC\cos(\phi + \frac{3\pi}{2})
\end{aligned}
$$

Eq. 6-2

Where $I_1$, $I_2$, $I_3$, $I_4$ represent the images of four steps respectively, Ø denotes the desired phase information and AC denotes the contrast. The phase can be calculated by the following equation:

$$\tan(\phi) = \frac{I_4 - I_2}{I_1 - I_3}$$

Eq. 6-3

The AC amplitude can be calculated with the equation

$$AC = \frac{\sqrt{\left(I_1 - I_3\right)^2 + \left(I_2 - I_4\right)^2}}{I_1 + I_2 + I_3 + I_4}$$

Eq. 6-4

## 6.2.2 Phase stepping in *V(z)* of confocal SPRM

In this experiment, I fixed the amplitude pattern and just changed the phase patterns by adding $\frac{\pi}{2}$ to the reference beam each time. More details on how to control the phase can be found in next section. As the system involves scanning along the axial direction, the output signal is a function of the defocus z. In the project, I assume *V(z)* is the interference between two vectors, S and R. *V(z)* can be expressed as:

$$I = \vec{V} * \vec{V^*} = \left|\vec{V}\right|^2 = (\vec{R} + \vec{S})(\vec{R} + \vec{S})^* = \left|\vec{R}\right|^2 + \left|\vec{S}\right|^2 + 2\left|\vec{R}\right|\left|\vec{S}\right|\cos(\theta)$$

By using different phase patterns of four steps, equations of four steps can be expressed as:

$$I_0 = \vec{V_0} * \vec{V_0^*} = \left|\vec{V_0}\right|^2 = (\vec{R} + \vec{S})(\vec{R} + \vec{S})^* = \left|\vec{R}\right|^2 + \left|\vec{S}\right|^2 + 2\left|\vec{R}\right|\left|\vec{S}\right|\cos(\theta)$$

$$I_1 = \vec{V_1} * \vec{V_1^*} = \left|\vec{V_1}\right|^2 = (\vec{R} + \vec{S})(\vec{R} + \vec{S})^* = \left|\vec{R}\right|^2 + \left|\vec{S}\right|^2 + 2\left|\vec{R}\right|\left|\vec{S}\right|\cos(\theta + \tfrac{\pi}{2})$$

$$I_2 = \vec{V_2} * \vec{V_2^*} = \left|\vec{V_2}\right|^2 = (\vec{R} + \vec{S})(\vec{R} + \vec{S})^* = \left|\vec{R}\right|^2 + \left|\vec{S}\right|^2 + 2\left|\vec{R}\right|\left|\vec{S}\right|\cos(\theta + \pi)$$

$$I_3 = \vec{V_3} * \vec{V_3^*} = \left|\vec{V_3}\right|^2 = (\vec{R} + \vec{S})(\vec{R} + \vec{S})^* = \left|\vec{R}\right|^2 + \left|\vec{S}\right|^2 + 2\left|\vec{R}\right|\left|\vec{S}\right|\cos(\theta + \tfrac{3\pi}{2})$$

Eq. 6-5

Then:

$$\tan\left(\theta(z)\right) = \frac{I_4(z) - I_2(z)}{I_1(z) - I_3(z)}$$

Eq. 6-6

$$AC(z) = \left|\vec{R}\right|\left|\vec{S}\right| = \frac{2\sqrt{(I_1(z) - I_3(z))^2 + (I_2(z) - I_4(z))^2}}{I_1(z) + I_2(z) + I_3(z) + I_4(z)}$$

Eq. 6-7

Because I can measure the response of the reference beam directly, the amplitude of the surface plasmon can be expressed as:

143

$$\left|\vec{S}\right| = \frac{\sqrt{(I_1(z) - I_3(z))^2 + (I_2(z) - I_4(z))^2}}{I_1(z) + I_2(z) + I_3(z) + I_4(z)} / \left|\vec{R}\right| \qquad \text{Eq. 6-8}$$

Eq. 6-6 will be used in the measurement of phase velocity and Eq. 6-8 will be used in the measurement of attenuation decaying length.

### 6.2.3 Beam profile modulation in the back focal plane

In section 6.2.2, I introduced the technique of phase stepping into the experiment and explained that I could extract the amplitude and phase information of the surface plasmon when shifting the phase difference between the reference 'R' and the surface plasmon 'S'. Here, I will show how to shift the phase difference between the two terms in the experimental simulation.
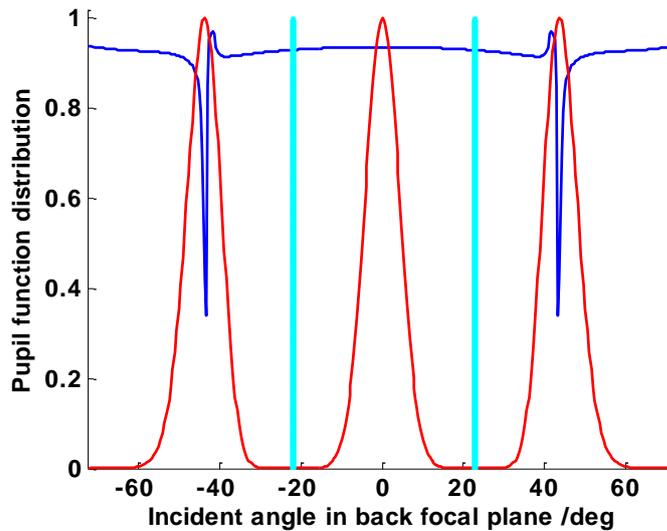


Fig. 6-2 Pupil function distribution (red curve) and calculated reflection coefficient for p-incident polarization on an uncoated sample (blue curve); the vertical cyan lines represent the range of angles over which the phase stepping of the reference beam was imposed.

The phase sensitive SLM shown in Fig. 6-1(b) is used to control the profile of the beam in the back focal plane. It is worth mentioning that the amplitude pupil function engineering is still required. Fig. 6-2 shows the pupil function distribution (red curve) and calculated reflection

coefficient for p-incident polarization on an uncoated sample (blue curve); the vertical cyan lines represent the range of angles over which the phase stepping of the reference beam was imposed. If I now assume that confocal system forms a two beam interferometer between the reference beam and the beam involving excitation and reradiation of SPs, I can use the phase shifting ability of the SLM to form a phase stepping interferometer between sample and reference. The experimental measurements and simulations will allow us to evaluate the effectiveness of this assumption and also to see the values of defocus where the assumption is valid.
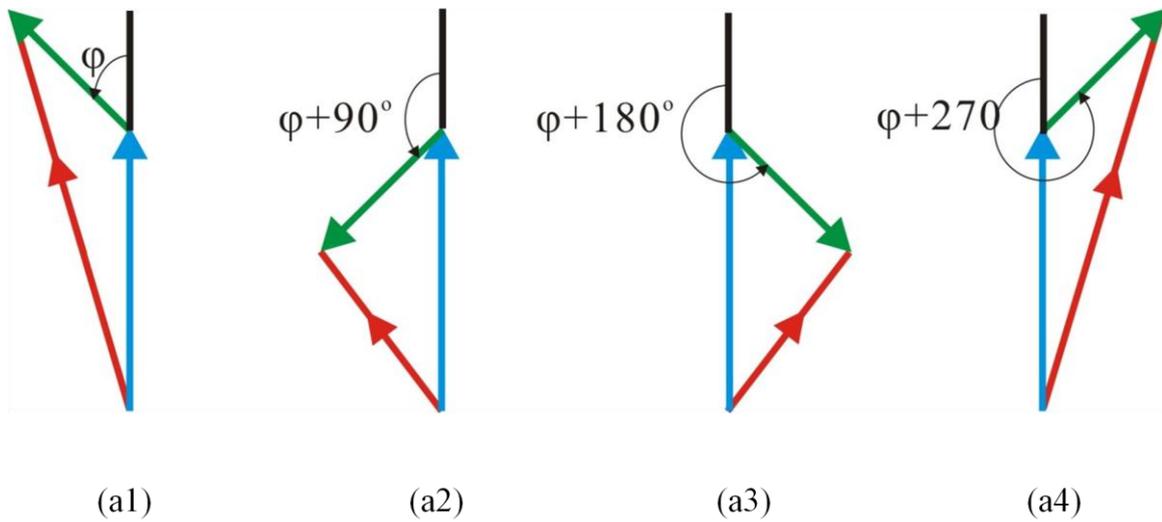


Fig. 6-3 Effect of phase stepping on relative phase of reference and plasmon beams, green line is the reference

signal R, blue line is the SP, red line is the resultant signal *V*. a1, a2, a3, a4 shows the four steps vectors;

Taking four phase shifts as the vector diagrams shown in Fig. 6-3, I form the standard interferometric expressions thus:

$$I_n = \left|\vec{R}\right|^2 + \left|\vec{S}\right|^2 + 2\left|\vec{R}\right|\left|\vec{S}\right|\cos(\varphi(z) + \alpha_n) \qquad \text{Eq. 6-9}$$

Where $\alpha_n = (n-1)\dfrac{\pi}{2}$ and n=1, 2, 3, 4; *R* and *S* represent the reference and signal beams respectively, and $\varphi$ represents the relative phase between the reference and signal beams.

These signals can then be readily processed to extract $\varphi$; the phase stepping also allows one to extract $|R|^2 + |S|^2$ as well as $|R||S|$, since the reference beam can be independently measured by blocking excitation of SPs the value of S can therefore be obtained independently. The formulae used to extract those terms were introduced in section 6.2.2. The vector diagrams are shown in Fig. 6-3. The methods and steps on how to impose an amplitude patterns using a phase SLM in antiphase is similar as that used in chapter 5 and the details can be referred to in chapter 3.

## 6.3 Phase stepping to obtain the plasmon angle

I now combine the phase stepping approach with $V(z)$ and obtain the relative phase between reference and signal beams as a function of defocus, $z$. The sample was scanned axially through each defocus position, $z$, and at each defocus position 4 phase steps were performed. The four $V(z)$ curves on bare gold obtained by shifting the phase of the reference in increments of 90 degrees are shown in Fig. 6-4. From lower to upper figures I have: zero phase shift (red), 90 degree phase shift (blue), 180 degree phase shift (black) and 270 degree phase shift (cyan). Then the four $V(z)$ curves are used to obtain the relative phase between reference and signal at each defocus, $\varphi(z)$. The relation between the $\varphi(z)$ and the plasmonic angle is expressed as:

$$\varphi(z) = 2kz(1 - \cos(\theta_p)) + \beta \qquad \text{Eq. 6-10}$$

$\theta_p$ is a phase constant accounting for the offset phase between sample and reference. The slope of the unwrapped phase is thus:

$$s_{slope} = 2k(1 - \cos(\theta_p)) \qquad \text{Eq. 6-11}$$

By measuring the slope of the fitted line, I can therefore calculate the plasmonic angle $\theta_p$.
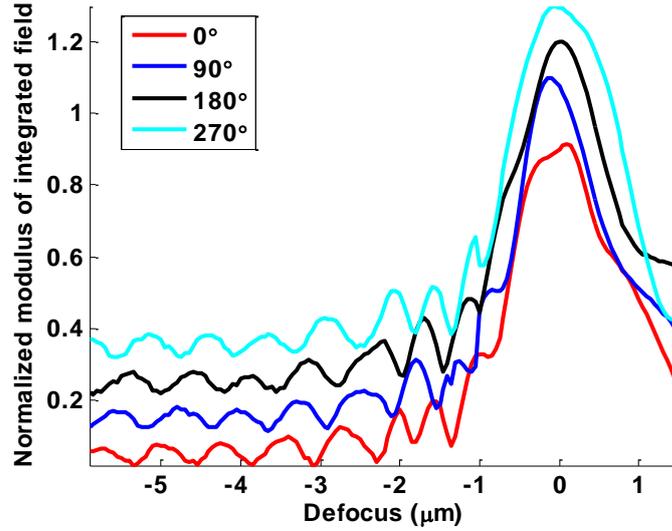
Fig. 6-4 *V(z)* curves variations of bare gold obtained by shifting the phase of the reference in increments of 90 degrees. From lower to upper figures I have: zero phase shift (red), 90 degree phase shift (blue), 180 degree phase shift (black) and 270 degree phase shift (cyan). Successive curves are shifted by 0.1 units for clarity.

Fig. 6-5 shows $\varphi(z)$ for a bare gold layer and a layer with an additional deposited layer of indium tin oxide (ITO). We can see that for positive defocus, that means the distance between the sample and the objective lens are longer than the focal length (see Fig. 6-1), there is little systematic difference between the responses for the two layers. For negative defocus close to the focal position the $\varphi(z)$ curve shows an irregular form, which is clearly not linear. This arises principally because the reference beam cannot be regarded as being a simple linear function as assumed. Aberration in the lens and possibly the finite number of pixels in the SLM means that the defocus value before the slope is linear is somewhat greater than predicted by theory. At larger defocus the unwrapped phase shows a linear form which relates to the value of $\theta_p$. The values of $\theta_p$ obtained for the bare layer and coated layers are 43.48 deg. and 46.39 deg. respectively, which correspond to a thickness of 13.4 nm of ITO assuming a refractive index of 1.858. The thickness of the ITO was measured independently with a commercial ellipsometer (alpha-SE J. A. Woollam (Inc)) was determined to be 11nm±2.5nm. The strength of the method for measuring the value of $\theta_p$ arises from several

147

factors (i) the region of defocus where accurate measurements can be obtained is readily observed from the linearity of $\varphi(z)$ where the periods of $V(z)$ are stable, (ii) the method uses all the data points in the measurement range thus optimizing the signal to noise ratio and (iii) while clearly the signal to noise ratio improves as the defocus range increases a reliable measurement can be obtained over a very small region of defocus corresponding to less than the theoretical $\Delta z_p$. Such a measurement range is not practical if one measures the amplitude only of the $V(z)$ curve without phase stepping. In the next section I compare by simulation the immunity to measurement noise of different processing methods. It demonstrates clearly that the present method is very stable and robust compared to methods used without phase stepping. I reiterate that $\varphi(z)$ refers to the phase of the SP rather than the $V(z)$.
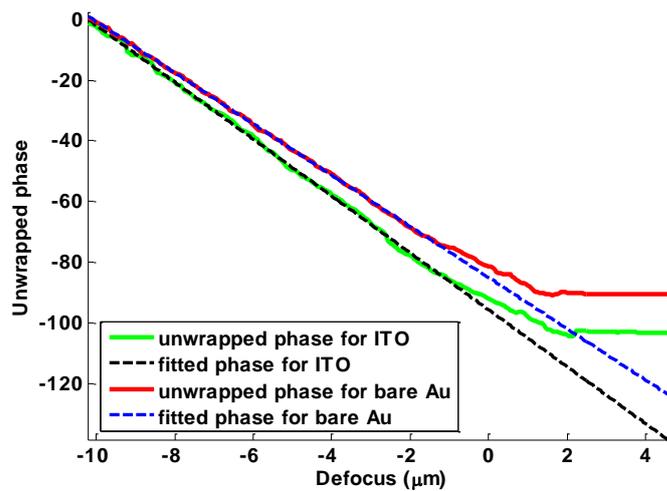


Fig. 6-5 Calculated $\varphi(z)$ from four $V(z)$ curves by using phase-stepping technique. The red curve refers to the unwrapped $\varphi(z)$ of bare gold and the blue line is the fitted data, while the green curve refers to the ITO coated sample case and the black line is the linear fitted data.

I introduced the phase stepping measurement above and assert that this method is more accurate and robust in calculating the plasmonic angle $\theta_p$ compared to direct measurement of the ripple period or Fourier transform measurement. In order to validate this, my colleague Pechprasarn carried out a set of Monte Carlo simulations to assess the performance of these

three measurement methods and the results are shown here for the completeness. The definitions of the three methods are as follows: 1) Direct measurement of the ripple period; the ripple period $\Delta z$ was calculated by averaging the first few ripples as shown in Fig. 6-6 (a) and then the plasmonic angle $\theta_p$ can be calculated. The minimum positions of the ripples are determined by 3rd order polynomial curve fitted to 25 data points (over a range of 200 nm) around the minimum as shown in Fig. 6-6 (b). 2) For the Fourier Transform measurement, the average ripple period $\Delta z$ was determined from Fourier transform of the windowed pattern of ripples. Details of the phase stepping measurement have been described above. In order to compare the three methods fairly I used four times as many measurements for the direct measurement and the Fourier method as the phase stepping measurement requires four different measurements.
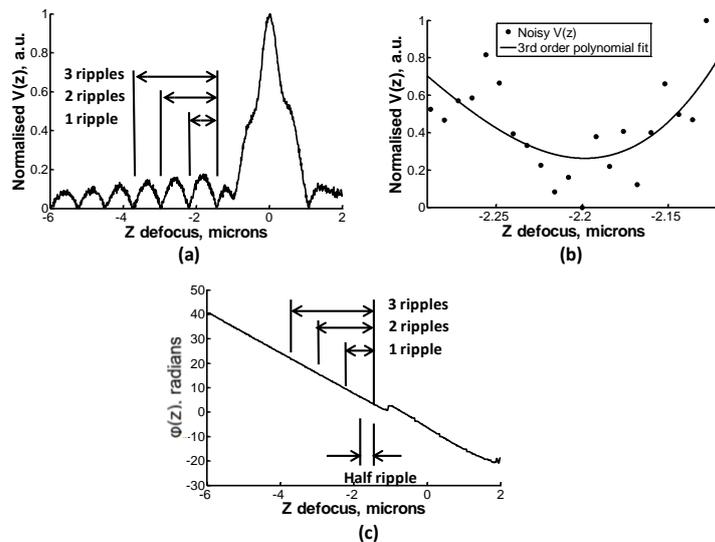


Fig. 6-6 (a) shows the method of measuring the ripple period measurement (b) shows 3rd order polynomial fit (black) to locate a minimum position for ripple period measurement; (c) shows regions on $\varphi(z)$ and corresponding ripple positions.

Now let us consider the case where there is noise. I will consider a shot noise source. The noise levels were calculated on the basis that the maximum signal in the $V(z)$ curve contained obtained without phase shifting. The SNR is presented in dB and each value corresponds to a

fixed number of photons. For $N$ incident photons the optical SNR is $\sqrt{N}$, so the electrical signal to noise is $N$, so that 60dB corresponds to $10^6$ measured photons. Values below the peak value are scaled appropriately, so have proportionately worse SNR values. The $V(z)$ curves were sampled at a spatial resolution of 8 nm, The optical signal to noise ratio is defined as:

$$SNR_{optical\ signal} = (SNR_{electrical\ signal})^2 = \frac{\mu^2}{\sigma^2} \qquad \text{Eq. 6-12}$$

where $\mu$ is the mean value and $\sigma^2$ is the variance, the ratio thus gives the signal to noise ratio. Monte Carlo simulations were carried out over $10^6$ cases. Monte Carlo simulations were carried out over $10^6$ cases. Standard derivation (S.D. in degrees) between the mean plasmonic angle (noiseless case) and the plasmonic angle recovered from the three methods (noisy cases) were determined in order to compare performance of each method as shown in Fig. 6-7(a) and (b). It may, of course, be argued that in many situations the noise is not shot noise limited, nevertheless, the relative performance between the different methods is retained provided each method is subject to similar noise models. The general conclusions are therefore valid for other independent noise processes.

Fig. 6-7 (a) and (b) shows that the performance of phase stepping measurement (solid black) performs best as it has the lowest S.D. compared to the others; the FFT method is the next best presumably because all the data is used and the poorest method involves direct measurement of the ripple. Interestingly, the phase stepping method can be used to make measurements over very small defocus ranges, even though its performance improves more rapidly than the other methods as the measurement range is increased. This is expected since the uncertainty of the gradient of a line rapidly decreases as the extent of the measurement increases.
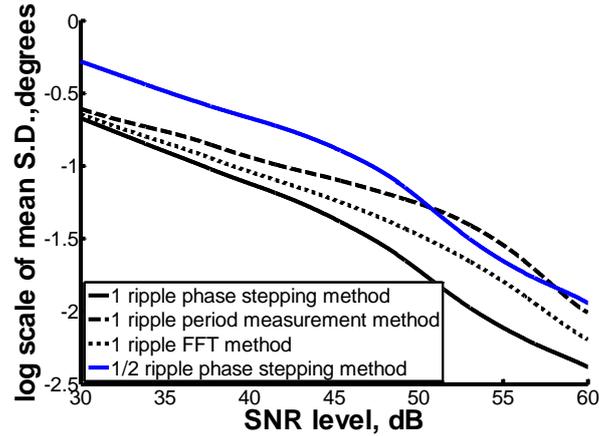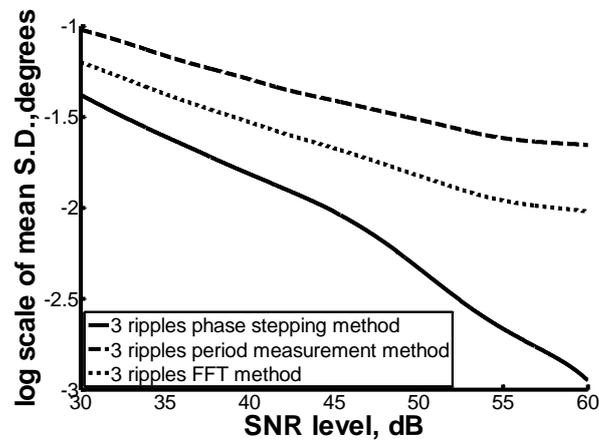
Fig. 6-7 (a) Mean standard deviation in degrees versus SNR level in dB for single ripple measurements and half ripple measurement for phase stepping. Solid black is for 1 ripple phase stepping measurement, dashed black for 1 ripple period measurement, dotted black for 1 ripple FFT measurement and solid blue for half ripple phase stepping measurement. (b) Mean standard deviation in degrees versus SNR level in dB for first three ripple measurements. Solid black curve is for 3 ripples phase stepping measurement, dashed black curve is for 3 ripples period measurement, dotted black for 3 ripples FFT measurement.

## 6.4 Measurement of SP propagation length

The propagation properties of the SP are related to its complex wave number where the real part is related to the attenuation of the wave. There are two components of the attenuation $\alpha_{leaky}$ and $\alpha_{loss}$, the first term represents the strength of the coupling between the SP and the

excitation medium. The second term $\alpha_{loss}$ is related to the ohmic losses in the metal and the total attenuation is the sum of these two terms.

The SLM allows us to make at least two distinct measurements of the SP propagation length which I can call indirect and direct. The indirect method is simply an extension of the phase stepping approach, where the value of $|S|$ can be obtained from the phase stepping approach (red curve in Fig. 6-10(a)). There are small ripples present on the curves obtained by the indirect method, due, in part, to small amounts of amplitude phase crosstalk on the SLM. The direct method involves performing a $V(z)$ measurement where only those angles close to $\theta_p$ are allowed to pass through the system; in other words the reference beam is blocked as the pattern distribution demonstrates in Fig. 6-8.
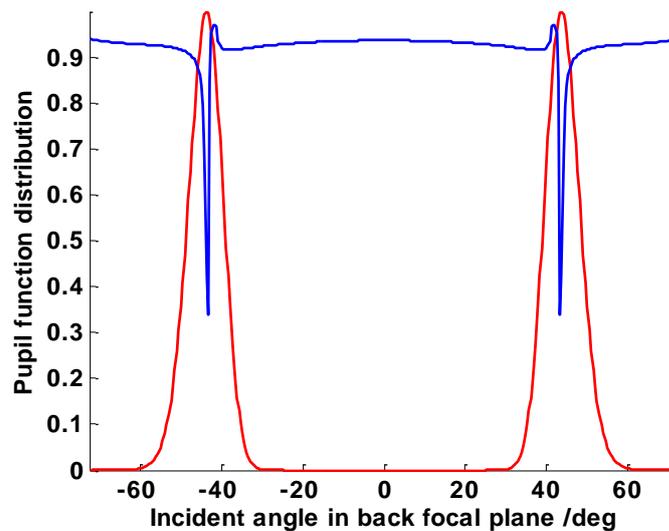


Fig. 6-8 Pupil function distribution (red curve) for the direct measurement of the propagation length and calculated reflection coefficient for p-incident polarization on an uncoated sample (blue curve);

If the phase is not required, there is no need for a reference beam. The detected $|S|$ is shown in the red curve in Fig. 6-10 (a). Both methods allow a value of $|S|$ to be obtained as a function of defocus, $z$. Fig. 6-9 shows the schematic diagram of the propagation length

calculation. There are two methods to calculate the phase delay for an incident at angle $\theta_p$ when the sample defocus is z. One method uses Fourier optics and the other uses a ray path that includes the assumed propagation path of the SP. If the results of the two methods match, one can say that the propagation length can be reliably represented by the ray picture of Fig. 6-9. Red curves show the actual rays of SPR signal and the reference beam (normal one). For the reference beam, the phase can be expressed as $2kn\Delta z$ while the phase of the SPR signal is

$$2kn\Delta z(\frac{1}{\cos\theta_p} - \sin\theta_p \tan\theta_p) = 2kn\Delta z \cos\theta_p \qquad \text{Eq. 6-13}$$

So the phase difference between the SPR and the reference is

$$2kn\Delta z(1 - \cos\theta_p) \qquad \text{Eq. 6-14}$$

When considering the problem from the point of view of plane waves, both the reference and the SPR signal can be assumed to have been emitted from the focal point. Based on this assumption, the phase of the reference (green line) is $2kn\Delta z$ and the phase of the SPR (blue curve) is $2kn\Delta z \cos\theta_p$, therefore, the phase difference between the SPR and the reference is also $2kn\Delta z(1 - \cos\theta_p)$ as the Eq. 6-14 shows. This gives confidence that one can use the ray path to approximate the path length of the SP. As a result, the attenuation constant measured in the propagation, x, direction can be related to the measured decay as a function of defocus, z using:

$$B_z z = B_x x \qquad \text{Eq. 6-15}$$

The $V(z)$ curves in Fig. 6-10 can be fitted to an exponential function $A\exp(-B_z z)$ which allows the strength of excitation and the attenuation to be obtained. Considering the relation $x = 2z \tan\theta_p$, I can get the below equation:

$$B_x = \frac{B_z}{2\tan\theta_p} \qquad\qquad \text{Eq. 6-16}$$

the propagation length can therefore be calculated as:

Then the propagation length can therefore be calculated as:

$$L_x = 2\tan\theta_p / B_z \qquad\qquad \text{Eq. 6-17}$$

This idea was originally proposed in the surface acoustic wave microscopy [81, 89, 90].
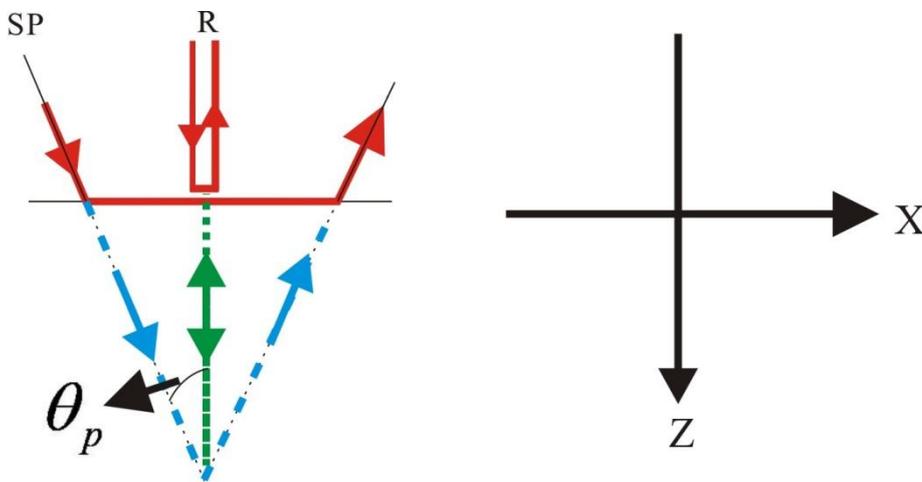


Fig. 6-9 Schematic diagram of the propagation length calculation
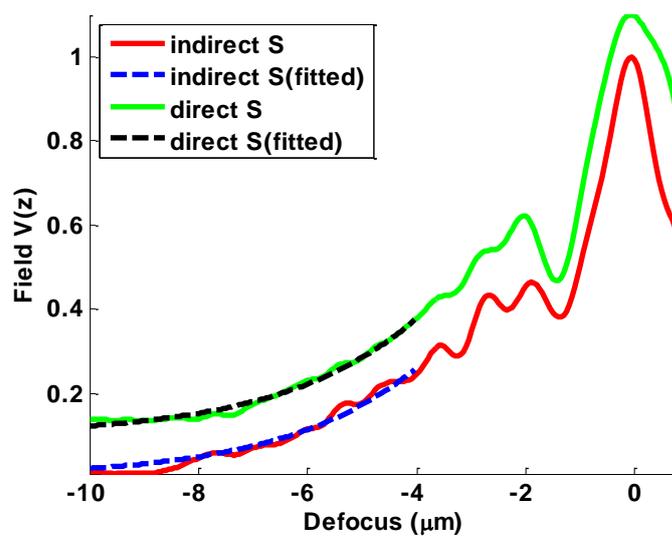


(a)
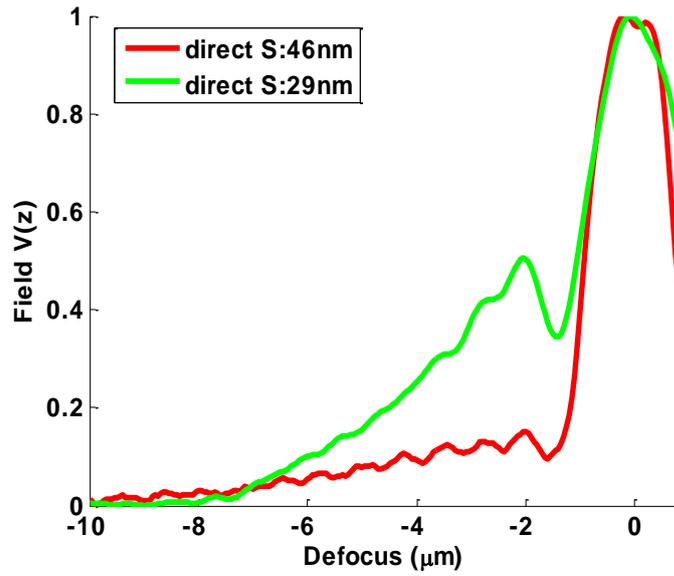
(b)
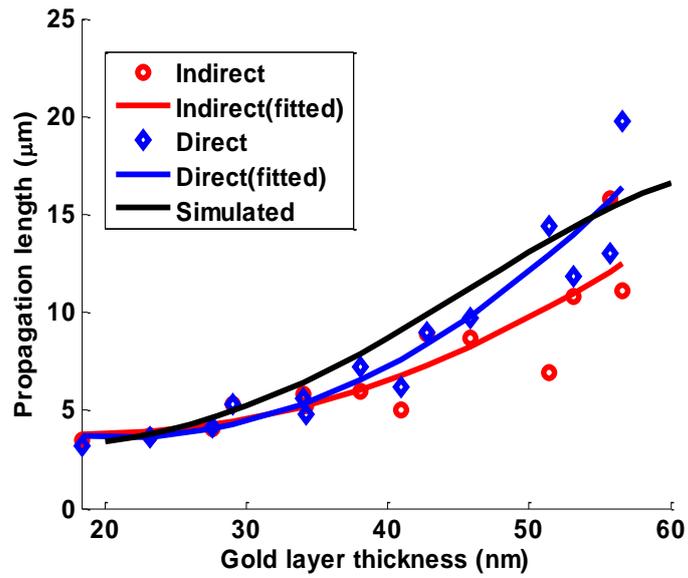


(c)

Fig. 6-10 (a) The |S| curves by using the direct method (add 0.1 in plot) and indirect methods; (b) Propagation

attenuation comparison between the 29nm and 46nm thickness of gold layer; (c) Propagation attenuation

comparison of /S/ for different thickness of gold layer, the blue curve shows the direct method results and the red

curve for the indirect results. The black curve represents the calculated value of attenuation for each layer

thickness. The data from each measurement was fitted to a third order polynomial curve.

In Fig. 6-10 (a), the green curve shows the measurements obtained by the direct method and the red curve shows the measurements obtained by the indirect method. The calculated attenuation is shown by the fitted curve. Fig. 6-10 (b) shows the comparison of the attenuation values between the 29nm and 46nm gold layer. The results demonstrate clearly that the 29nm gold layer provides higher attenuation than the 46nm case. Fig. 6-10 (c) shows values of attenuation obtained for different thicknesses of gold (which affects the attenuation strongly) by using the direct and indirect methods. The simulation results are shown on the black curve. It can be seen, as may be expected, that the direct method shows a smaller variance around the fitted values, nevertheless, both measurements show a similar trend. The standard deviations from the third order fits are smaller for the direct method (1.09 microns) compared to the indirect method (1.63 microns) as shown in Fig. 6-10 (c). This suggests that better measurement precision is obtained with the direct method, provided the fitted curve can be taken as a reasonable reference point. The measurement of attenuation of SPs can therefore be obtained using pupil function engineering. It is clear that the error in the attenuation measurement is far greater compared to the measurement of the real part of the wave number. Indeed similar observations were made in the measurement of velocity and attenuation of surface acoustic waves using the *V(z)* method in the scanning acoustic microscope, where relative accuracy of around 1 part in $10^3$ was obtained for the measurement of velocity but 'a few' per cent for attenuation[1].

## 6.5 Conclusions

This chapter has presented a technique to extract the SP properties applying a phase SLM to shift the phase difference between the reference beams and SP signal in the confocal surface plasmon microscope (Fig. 6-1). I show how the method can be used to measure the phase velocity which corresponds to the SP k-vector and propagation attenuation caused by

radiation leakage and ohmic heating. Compared to the previous measurement of the SP k-vector in chapter 4 and chapter 5, the new technique provides more robust, more accurate and potentially faster results. The fact that measurements can be made over a very small scan range means that the optimum spatial resolution is superior to processing methods requiring large defocus range. The method also provides a means to evaluate the attenuation, although the relative uncertainty in this measurement is presently far greater than the uncertainty in the measurement of the real part of the SP wave number.

# 7   Conclusion and future work

## 7.1 Conclusion

In this thesis, I have described the confocal surface plasmon microscopic sensing. This chapter will summarize the main aspects in previous chapters (chapter 4, 5 and 6) and draw the conclusions of the three experiments described in chapter 4, 5 and 6. Future work will be discussed later in section 7.2 of this chapter.

### 7.1.1 Confocal surface plasmon microscopy with pupil function engineering

Surface plasmon microscopy enables measurement of local refractive index on a far finer scale than prism based systems. Interferometric plasmon imaging delivers quantitative high spatial resolution images sensitive to refractive index. In addition the so called $V(z)$ method allows image contrast to be controlled by varying the sample defocus without substantially degrading spatial resolution. In chapter 4, I demonstrated the feasibility of using a confocal arrangement to perform localized measurement of SP propagation. Firstly, a big advantage of the system is that it can be incorporated into a conventional confocal microscope with minimal adaptation. Secondly, as this system placed greater demands on the dynamic range of the system, I therefore use a spatial light modulator (SLM) to engineer the microscope pupil function to suppress light that does not contribute to the signal. Furthermore, I used the SLM to modulate the sharp edge of the beam profile and removed the sharp effect on the $V(z)$ curves. I proposed several different illumination pupil functions and showed the difference of them in the chapter. Thirdly, I examined the effect of pinhole diameter and demonstrated that the pinhole size should not be too small or too big. If the pinhole size was too small, the signal to noise ratio (SNR) would be poor; while if the pinhole size was too big, the $V(z)$ effect would disappear. I found that operating with a pinhole size between 10%-50% of the

Airy disc provided satisfactory result. Finally, I showed the 1D line scanning image of the BSA grating in section 4.5.

## 7.1.2 Surface plasmon microscopic sensing with beam profile modulation

In chapter 4, I have showed that the confocal system gives the so-called $V(z)$ curve when the sample is scanned axially, which gives a measure of the surface plasmon propagation velocity. However, the mechanical scanning in the axial z direction was required which made the experiment time-consuming owing to the mechanical scanning and limited the applications of the system, due to the system vibration. Furthermore, in the experiment, I found that because of the precision of the piezoelectric stage, when I scanned the $V(z)$ curves on the grating like sample, I could not make the piezo stage return to the exact initial position, which would introduce some error in the imaging of the sample. In order to solve these problems, in the surface plasmon microscopic sensing with beam profile modulation experiment described in chapter 5, I replaced the amplitude sensitive spatial light modulator (SLM) with a phase sensitive SLM which made the phase of the beam profile on the back focal plane possible. I showed how a phase SLM could greatly extend the utility of confocal based SP sensing and imaging. The crucial feature in SP imaging was that contrast changes and quantification of the SP $k$-vector can be obtained by axially scanning of the sample. I showed that this might be achieved functionally by simply altering the phase profile of the SLM. This removed the need for precision mechanical components and was inherently more stable and also potentially quicker. In total , I showed how a phase spatial light modulator (i) performs the necessary pupil function apodization (ii) imposes an angular varying phase shift that effectively changes sample defocus without any mechanical movement and (iii) changes the relative phase of the surface plasmon and reference beam to provide signal enhancement not possible with previous configurations used in chapter 4.

### 7.1.3 Quantitative plasmonic measurements

In chapter 4 and 5, I showed how a confocal configuration could form a surface plasmon microscope involving interference between a path involving the generation of surface plasmon and one involving a directly reflected beam. The relative phase of these contributions changes with axial scan position allowing the phase velocity of the surface plasmon to be measured. In the quantitative plasmonic measurements using embedded phase stepping confocal interferometry described in chapter 6, I extended the interferometer concept to produce an 'embedded' phase shifting interferometer, where I could control the phase between the reference and surface plasmon beams with a spatial light modulator. I demonstrated that this approach facilitates extraction of the amplitude and phase of the surface plasmon to measure of the phase velocity which corresponds to the SP k-vector and the attenuation of the surface plasmons caused by radiation leakage and ohmic heating. Compared to the previous measurement of the SP k-vector[1], the new technique provides more robust, more accurate and potentially faster results. The fact that measurements can be made over a very small scan range means that the optimum spatial resolution is superior to processing methods requiring large defocus range. The method also provides a means to evaluate the attenuation, although the relative uncertainty in this measurement is presently far greater than the uncertainty in the measurement of the real part of the SP wave number.

## 7.2 Future work

### 7.2.1 Imaging and sensing in an aqueous environment

All the experiments in this thesis were carried out in air. As one major application of surface plasmon is to sense and image biological samples which live in an aqueous environment. The future job is therefore to extend the system to operate in water media. The whole system would be the same except for the laser and the sample scanning. In water, a larger incident

angle is required to excite SPR as shown in Fig. 7-1(a). For the coverglass/50nm gold/ sample structure, if the sample is pure air, the plasmonic angle is about 43.7° however if the sample is pure water, the plasmonic angle is increased to be 71°. Therefore an objective with higher NA is needed. Colleagues usually use NA1.49 objective lens by Olympus to do experiments in water combined with 690nm laser as the illumination as the wavelength of 690nm can will required lower NA as shown in Fig. 7-1(b).
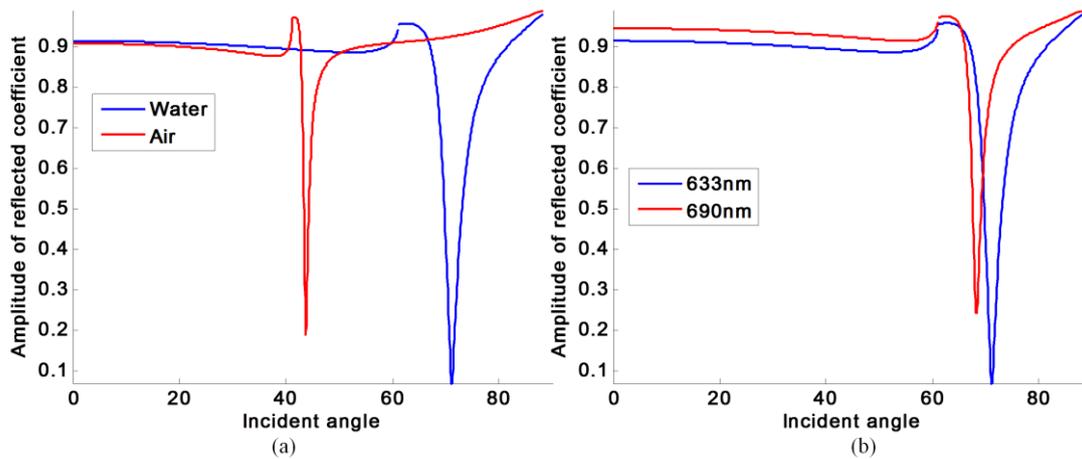


Fig. 7-1 (a) Simulated SPR excitation comparison in water and in air; (b) Simulated SPR excitation in water using 633nm and 690nm illumination respectively.

For the experiments in air, I just needed to hold the sample and no special device was required in the sample scanning part. However, if I need to do the experiments in aqueous environment, a flow cell which is required to inject and extract the liquid. The diagram is shown in Fig. 7-2.
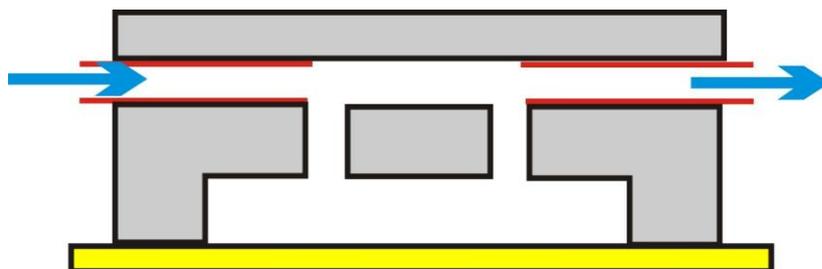


Fig. 7-2 Schematic diagram of the designed flow cell

161

## 7.2.2 Artificial plasmon

In the main part of the thesis, I used the interference between the beam at the centre of the BFP ('P1' in Fig. 1-2) and that on the SPR ring ('P2' in Fig. 1-2). When I scan the defocus, the phase difference between the two beam parts will give us the $V(z)$ effect. However, as the two beam parts (P1 and P2) are located at different radius of the BFP, they behave differently for the microphotonics. Then I ask: can I put the signal beam and the reference beam at similar radius on the BFP?



(a)　　(b)

(c)
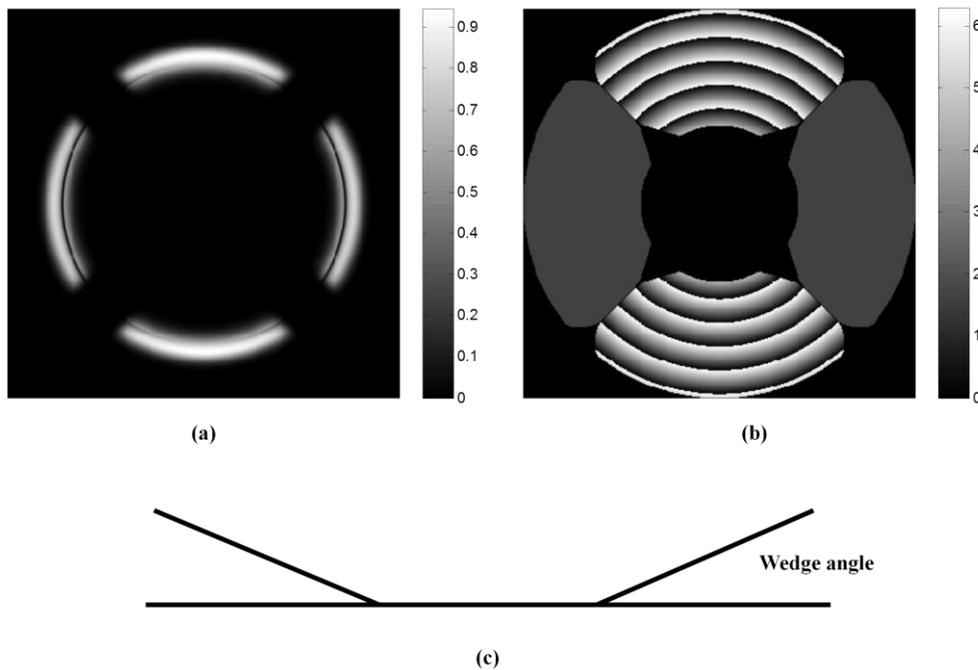
Fig. 7-3 (a) Amplitude pupil function used for the artificial plasmon; (b) Phase pup S wedge angle =-0.1111

degrees; (c) unwrapped phase pattern; Pixel size=15 microns and one-sided wedge=100 pixels and back focal

plane size=357 pixels

At the very beginning of the review of SPs in chapter 2, I mentioned that only p-wave could be used to excite SPR while s-wave does not excite SP, however, both p and s are located on the same radius of the BFP. That means I can use the s-wave as the reference rather than the centre part. I call this technique artificial plasmon. The diagram of the intensity pattern is shown in Fig. 7-3 (a). I divide the BFP into four parts and the two quarters with SPR dips is

the signal beam while the other two quarters is the reference. One problem here is that in the confocal system, a pinhole is added in the detection. That means only the excited SPs will be detected while the non-propagating s-wave will be blocked. In order to solve this problem, I use a 'virtual' wedge to bend the s-wave so that it can also be detected. The 'virtual' wedge (Fig. 7-3 (c)) is realized by imposing a wedge phase pattern on the radius where the s-wave located on the phase sensitive SLM. As the phase SLM can only provide phase between 0 and $2\pi$, if the imposed phase for the s-wave, I will wrap it. The diagram of the phase pattern is shown in Fig. 7-3 (b). I will show that this artificial plasmon technique is more robust to microphotonics.

## 7.3 Summary

In this chapter, I have summarized the main aspects of the three experiments described in chapter 4, 5 and 6 respectively and drew the conclusion that I have achieved the objective aims. Later in section 7.2, I discussed the future works which included two parts: 1) confocal surface plasmon microscopic imaging and sensing in aqueous environment; 2) artificial plasmon.

# References

1.  Kushibiki, J. and N. Chubachi, *Material characterization by line-focus-beam acoustic microscope.* Ieee Transactions on Sonics and Ultrasonics, 1985. **32**(2): p. 189-212.

2.  Zernike, F., *Phase contrast, a new method for the microscopic observation of transparent objects part II.* Physica, 1942. **9**(10): p. 974-986.

3.  pechprasarn, S., *Analysis of sensitivity and resolution in plasmonic microscopes.* Thesis, 2012.

4.  Somekh, M.G., S.G. Liu, T.S. Velinov, and C.W. See, *High-resolution scanning surface-plasmon microscopy.* Applied Optics, 2000. **39**(34): p. 6279-6287.

5.  Somekh, M.G., S.G. Liu, T.S. Velinov, and C.W. See, *Optical V(z) for high-resolution 2 pi surface plasmon microscopy.* Optics Letters, 2000. **25**(11): p. 823-825.

6.  Argoul, F., T. Roland, A. Fahys, L. Berguiga, and J. Elezgaray, *Uncovering phase maps from surface plasmon resonance images: Towards a sub-wavelength resolution.* Comptes Rendus Physique, 2012. **13**(8): p. 800-814.

7.  Berguiga, L., T. Roland, K. Monier, J. Elezgaray, and F. Argoul, *Amplitude and phase images of cellular structures with a scanning surface plasmon microscope.* Opt. Express, 2011. **19**(7): p. 6571-6586.

8.  Berguiga, L., S. Zhang, F. Argoul, and J. Elezgaray, *High-resolution surface-plasmon imaging in air and in water: V(z) curve and operating conditions.* Optics Letters, 2007. **32**(5): p. 509-511.

9.  Somekh, M.G., G. Stabler, S. Liu, J. Zhang, and C.W. See, *Wide-field high-resolution surface-plasmon interference microscopy.* Optics Letters, 2009. **34**(20): p. 3110-3112.

10. Stabler, G., M.G. Somekh, and C.W. See, *High-resolution wide-field surface plasmon microscopy.* Journal of Microscopy-Oxford, 2004. **214**: p. 328-333.

11. Somekh, M.G., *Depth discrimination in scanned heterodyne microscope systems.* Journal of Microscopy-Oxford, 1992. **168**: p. 131-151.

12. Rothenhausler, B. and W. Knoll, *Surface-plasmon microscopy.* Nature, 1988. **332**(6165): p. 615-617.

13. Yeatman, E. and E.A. Ash, *Surface-plasmon microscopy.* Electronics Letters, 1987. **23**(20): p. 1091-1092.

14. Pechprasarn, S. and M.G. Somekh, *Surface plasmon microscopy: resolution, sensitivity and crosstalk.* J Microsc, 2012. **246**(3): p. 287-97.

15. Somekh, M. and S. Pechprasarn, *Surface plasmon microscopy resolution vs sensitivity.* IEEEXplore Photonics Global Conference (PGC), 2010, 2010.

16. Anker, J.N., W.P. Hall, O. Lyandres, N.C. Shah, J. Zhao, and R.P. Van Duyne, *Biosensing with plasmonic nanosensors.* Nature Materials, 2008. **7**(6): p. 442-453.

17. Liu, S., *Optical microscopy for high resolution and high sensitivity imaging of biological samples* Thesis, 2002.

18. Wood, R.W., *On a remarkable case of uneven distribution of light in a diffraction grating spectrum.* Philosophical Magazine, 1902. **4**(19-24): p. 396-402.

19. Wood, R.W., *Diffraction gratings with controlled groove form and abnormal distribution of intensity.* Philosophical Magazine, 1912. **23**(133-8): p. 310-317.

20. Rayleigh, *On the dynamical theory of gratings.* Proceedings of the Royal Society of London Series a-Containing Papers of a Mathematical and Physical Character, 1907. **79**(532): p. 399-416.

21. Rayleigh, L., *Note on the remarkable case of diffraction spectra described by Prof. Wood.* Philosophical Magazine, 1907. **14**(79-84): p. 60-65.

22. Fano, U., *The theory of anomalous diffraction gratings and of quasi-stationary waves on metallic surfaces (Sommerfeld's waves).* Journal of the Optical Society of America, 1941. **31**(3): p. 213-222.

23. Hessel, A. and A.A. Oliner, *A New Theory of Wood?s Anomalies on Optical Gratings.* Appl. Opt., 1965. **4**(10): p. 1275-1297.

24. Powell, C.J. and J.B. Swan, *Effect of oxidation on the characteristic loss spectra of Aluminum and Magnesium.* Physical Review, 1960. **118**(3): p. 640-643.

25. Ritchie, R.H., *Plasma losses by fast electrons in thin films.* Physical Review, 1957. **106**(5): p. 874-881.

26. Bohm, D. and D. Pines, *A collective description of electron interactions .1. magnetic interactions.* Physical Review, 1951. **82**(5): p. 625-634.

27. Bohm, D. and D. Pines, *A collective description of electron interactions .3. coulomb interactions in a degenerate electron gas.* Physical Review, 1953. **92**(3): p. 609-625.

28. Pines, D., *A collective description of electron interactions.4. electron interaction in metals.* Physical Review, 1953. **92**(3): p. 626-636.

29. Pines, D. and D. Bohm, *A collective description of electron interactions .2. collective VS individual particle aspects of the interactions.* Physical Review, 1952. **85**(2): p. 338-353.

30. Barnes, W.L., A. Dereux, and T.W. Ebbesen, *Surface plasmon subwavelength optics.* Nature, 2003. **424**(6950): p. 824-830.

31. Hecht, E., *Optics.* Addison-Wesley; 4 th edition 2001.

32. Raether, H., *Surface plasmons on smooth and rough surfaces and on gratings.* Springer Tracts in Modern Physics. 1988: Springer-Verlag.

33. Won, H., *Surface-plasmon-polariton waveguides.* Phd thesis,Hanyang University, 2005.

34. Zhang, J., *High resolution solid immersion lens microscopy and its application to surface plasmon resonance imaging.* Ph.D thesis, University of Nottingham, 2006.

35. Kano, H. and S. Kawata, *Grating-coupled surface-plasmon for measuring the refractive-index of a liquid sample.* Japanese Journal of Applied Physics Part 1-Regular Papers Short Notes & Review Papers, 1995. **34**(1): p. 331-335.

36. Kano, H., S. Mizuguchi, and S. Kawata, *Excitation of surface-plasmon polaritons by a focused laser beam.* J. Opt. Soc. Am. B, 1998. **15**(4): p. 1381-1386.

37. Otto, A., *Excitation of nonradiative surface plasma waves in silver by method of frustrated total reflection.* Zeitschrift Fur Physik, 1968. **216**(4): p. 398-&.

38. Kretschm.E, *Determination of optical constants of metals by excitation of surface plasmons.* Zeitschrift Fur Physik, 1971. **241**(4): p. 313-&.

39. Kretschm.E and H. Raether, *Radiative decay of non radiative surface plasmons excited by light.* Zeitschrift Fur Naturforschung Part a-Astrophysik Physik Und Physikalische Chemie, 1968. **A 23**(12): p. 2135-&.

40. Berger, C.E.H., R.P.H. Kooyman, and J. Greve, *Resolution in surface-plasmon microscopy.* Review of Scientific Instruments, 1994. **65**(9): p. 2829-2836.

41. Abeles, F., *Use of optical cavities for investigation of surface films.* Journal of Vacuum Science & Technology, 1972. **9**(1): p. 169-&.

42. Azzam, R.M.A., *Ellipsometry and polarized light*, ed. N.M.j.a. Bashara. 1977, Amsterdam ; New York : New York :: North-Holland Pub. Co. ; sole distributors for the U.S.A. and Canada, Elsevier North-Holland.

43.     Cardona, M., *Fresnel reflection and surface plasmons.* American Journal of Physics, 1971. **39**(10): p. 1277-&.

44.     Johs, B.D., R.H. French, F.D. Kalk, W.A. McGahan, and J.A. Woollam, *Optical analysis of complex multilayer structures using multiple data types.* 1994: p. 1098-1106.

45.     Tan, *High resolution angle scanning surface plasmon resonance microscopy and its application to bio-molecular interactions.* Ph.D thesis, University of Nottingham, 2011.

46.     Strong, J., *Effect of evaporated films on energy distribution in grating spectra.* Physical Review, 1936. **49**(4): p. 0291-0296.

47.     Giebel, K.F., C. Bechinger, S. Herminghaus, M. Riedel, P. Leiderer, U. Weiland, and M. Bastmeyer, *Imaging of cell/substrate contacts of living cells with surface plasmon resonance microscopy.* Biophysical Journal, 1999. **76**(1): p. 509-516.

48.     de Bruijn, H.E., R.P. Kooyman, and J. Greve, *Choice of metal and wavelength for surface-plasmon resonance sensors: some considerations.* Applied Optics, 1992. **31**(4).

49.     Eustis, S. and M.A. El-Sayed, *Why gold nanoparticles are more precious than pretty gold: Noble metal surface plasmon resonance and its enhancement of the radiative and nonradiative properties of nanocrystals of different shapes.* Chemical Society Reviews, 2006. **35**(3): p. 209-217.

50.     Homola, J., *Surface plasmon resonance sensors for detection of chemical and biological species.* Chemical Reviews, 2008. **108**(2): p. 462-493.

51.     Y. H. Huang, H.P.H., 1 S. Y. Wu,1 and S. K. Kong2, *Detecting Phase Shifts in Surface Plasmon Resonance: A Review.* Advances in Optical Technologies, 2012. **2012**.

52.     Lyon, L.A., M.D. Musick, and M.J. Natan, *Colloidal Au-enhanced surface plasmon resonance immunosensing.* Analytical Chemistry, 1998. **70**(24): p. 5177-5183.

53.     Homola, J., S.S. Yee, and G. Gauglitz, *Surface plasmon resonance sensors: review.* Sensors and Actuators B: Chemical, 1999. **54**(1-2): p. 3-15.

54.     Homola, J., I. Koudela, and S.S. Yee, *Surface plasmon resonance sensors based on diffraction gratings and prism couplers: sensitivity comparison.* Sensors and Actuators B: Chemical, 1999. **54**(1–2): p. 16-24.

55. Abdiche, Y.N., D.S. Malashock, A. Pinkerton, and J. Pons, *Exploring blocking assays using Octet, ProteOn, and Biacore biosensors.* Analytical Biochemistry, 2009. **386**(2): p. 172-180.

56. Kabashin, A.V., S. Patskovsky, and A.N. Grigorenko, *Phase and amplitude sensitivities in surface plasmon resonance bio and chemical sensing.* Optics Express, 2009. **17**(23): p. 21191-21204.

57. Hooper, I.R., J.R. Sambles, M.C. Pitter, and M.G. Somekh, *Phase sensitive array detection with polarisation modulated differential sensing.* Sensors and Actuators B-Chemical, 2006. **119**(2): p. 651-655.

58. Nylander, C., B. Liedberg, and T. Lind, *Gas-detection by means of surface-plasmon resonance.* Sensors and Actuators, 1982. **3**(1): p. 79-88.

59. Miwa, S. and T. Arakawa, *Selective gas detection by means of surface plasmon resonance sensors.* Thin Solid Films, 1996. **282**(1-2): p. 466-468.

60. Sigal, G.B., C. Bamdad, A. Barberis, J. Strominger, and G.M. Whitesides, *A self-assembled monolayer for the binding and study of histidine tagged proteins by surface plasmon resonance.* Analytical Chemistry, 1996. **68**(3): p. 490-497.

61. Ostuni, E., L. Yan, and G.M. Whitesides, *The interaction of proteins and cells with self-assembled monolayers of alkanethiolates on gold and silver.* Colloids and Surfaces B-Biointerfaces, 1999. **15**(1): p. 3-30.

62. Su, K.H., Q.H. Wei, X. Zhang, J.J. Mock, D.R. Smith, and S. Schultz, *Interparticle coupling effects on plasmon resonances of nanogold particles.* Nano Letters, 2003. **3**(8): p. 1087-1090.

63. Ditlbacher, H., J.R. Krenn, G. Schider, A. Leitner, and F.R. Aussenegg, *Two-dimensional optics with surface plasmon polaritons.* Applied Physics Letters, 2002. **81**(10): p. 1762-1764.

64. Matsui, J., K. Akamatsu, N. Hara, D. Miyoshi, H. Nawafune, K. Tamaki, and N. Sugimoto, *SPR sensor chip for detection of small molecules using molecularly imprinted polymer with embedded gold nanoparticles.* Analytical Chemistry, 2005. **77**(13): p. 4282-4285.

65. Pernites, R.B., R. Ponnapati, M.J. Felipe, and R. Advincula, *SPR sensing of drug molecules using a smart polymer film.* Abstracts of Papers of the American Chemical Society, 2010. **240**.

66. Okamoto, T. and I. Yamaguchi, *Surface-plasmon microscope with an electronic angular scanning.* Optics Communications, 1992. **93**(5-6): p. 265-270.

67. Knobloch, H., G. vonSzadaBorryszkowski, S. Woigk, A. Helms, and L. Brehmer, *Dispersive surface plasmon microscopy for the characterization of ultrathin organic films.* Applied Physics Letters, 1996. **69**(16): p. 2336-2337.

68. Hickel, W. and W. Knoll, *Surface-plasmon optical characterization of lipid monolayers at 5 mu-m lateral resolution.* Journal of Applied Physics, 1990. **67**(8): p. 3572-3575.

69. Kooyman, R.P.H. and U.J. Krull, *Surface-plasmon microscopy of 2 crystalline domains in a lipid monolayer.* Langmuir, 1991. **7**(7): p. 1506-1509.

70. Kawata, S., *Near-field optics and surface plasmon polaritons.* Springer, 2001.

71. Zayats, A.V., J. Elliott, Smolyaninov, II, and C.C. Davis, *Imaging with short-wavelength surface plasmon polaritons.* Applied Physics Letters, 2005. **86**(15).

72. Fanton, J.T., J. Opsal, D.L. Willenborg, S.M. Kelso, and A. Rosencwaig, *Multiparameter measurements of thin-films using beam-profile reflectometry.* Journal of Applied Physics, 1993. **73**(11): p. 7035-7040.

73. See, C.W., M.G. Somekh, and R.D. Holmes, *Scanning optical microellipsometer for pure surface profiling.* Applied Optics, 1996. **35**(34): p. 6663-6668.

74. Shatalin, S.V., R. JuŠKaitis, J.B. Tan, and T. Wilson, *Reflection conoscopy and micro-ellipsometry of isotropic thin film structures.* Journal of Microscopy, 1995. **179**(3): p. 241-252.

75. Kano, H. and W. Knoll, *A scanning microscope employing localized surface-plasmon-polaritons as a sensing probe*. Vol. 182. 2000, Amsterdam, PAYS-BAS: Elsevier. 11-15.

76. Zhang, J., C.W. See, M.G. Somekh, M.C. Pitter, and S.G. Liu, *Wide-field surface plasmon microscopy with solid immersion excitation.* Applied Physics Letters, 2004. **85**(22): p. 5451-5453.

77. Zhang, J., C.W. See, and M.G. Somekh, *Imaging performance of widefield solid immersion lens microscopy.* Applied Optics, 2007. **46**(20): p. 4202-4208.

78. Zhang, J., M.C. Pitter, S. Liu, C. See, and M.G. Somekh, *Surface-plasmon microscopy with a two-piece solid immersion lens: bright and dark fields.* Applied Optics, 2006. **45**(31): p. 7977-7986.

79. Atalar, A. and H. Koymen, *V(z) of the surface acoustic-wave focusing system.* Ieee Transactions on Ultrasonics Ferroelectrics and Frequency Control, 1987. **34**(3): p. 387-388.

80. R.A.Lemons and C.F.Quate, *Acoustic microscopy-scanning version.* Applied Physics Letters, 1974. **24**(4): p. 163-165.

81. Zhou, H. and C.J.R. Sheppard, *Aberration measurement in confocal microscopy: Phase retrieval from a single intensity measurement.* Journal of Modern Optics, 1997. **44**(8): p. 1553-1561.

82. Minsky, M., *Confocal Microscopy.* Microscopy apparatus, 1961. **US19570695107 19571107 (US 3013467 (A))**.

83. JB, P., *Handbook of Biological Confocal Microscopy (3rd ed. ed.).* 2006.

84. Semwogerere, D. and E.R. Weeks, *Confocal Microscopy.* Encyclopedia of Biomaterials and Biomedical Engineering, Taylor & Francis, 2005.

85. Gordon, J.G. and J.D. Swalen, *Effect of thin orgainic films on surface plasma resonance on gold.* Optics Communications, 1977. **22**(3): p. 374-376.

86. Torok, P., P.D. Higdon, and T. Wilson, *On the general properties of polarised light conventional and confocal microscopes.* Optics Communications, 1998. **148**(4-6): p. 300-315.

87. Ilett, C., M.G. Somekh, and G.A.D. Briggs, *Acoustic microscopy of elastic discontinuities.* Proceedings of the Royal Society of London Series a-Mathematical Physical and Engineering Sciences, 1984. **393**(1804): p. 171-&.

88. Singh, H. and J.S. Sirkis, *Direct extraction of phase gradients from Fourier-transform and phase-step fringe patterns.* Appl. Opt., 1994. **33**(22): p. 5016-5020.

89. Parmon, W. and H.L. Bertoni, *Ray interpretation of the material signature in the acoustic microscope.* Electronics Letters, 1979. **15**(21): p. 684-686.

90. Atalar, A., C.F. Quate, and H.K. Wickramasinghe, *Phase imaging in reflection with acoustic microscope.* Applied Physics Letters, 1977. **31**(12): p. 791-793.